

**Fractional vortices
in Josephson tunnel junctions
with a ferromagnetic
interlayer**

DISSERTATION

Zur Erlangung des Grades eines Doktors
der Naturwissenschaften
der Fakultät für Mathematik und Physik
der Eberhard-Karls-Universität zu Tübingen

vorgelegt von

JUDITH PFEIFFER

aus Schweinfurt

2010

Tag der mündlichen Prüfung: 11.01.2010
Dekan: Prof. Dr. W. Knapp
1. Berichterstatter: Prof. Dr. R. Kleiner
2. Berichterstatter: Prof. Dr. D. Kölle

*Hey you,
out there in the cold*

Pink Floyd

Abstract

In this thesis, we study Josephson tunnel junctions with a ferromagnetic interlayer, so-called SIFS (superconductor-insulator-ferromagnet-superconductor) Josephson junctions. Conventional 0 Josephson junctions have a current phase relation $I = I_c \sin \mu$ with $I_c > 0$. In contrast, SIFS Josephson junctions provide the possibility to realize π junctions. In such structures the superconducting wave function changes its sign across the barrier, *i.e.*, shifts its phase by π . The current phase relation of π junctions reads $I = I_c \sin \mu$, formally with $I_c < 0$. Using a step-like thickness of the ferromagnetic barrier, allows to fabricate so-called $0-\pi$ Josephson junctions. The ground state phase in such junctions has a value of 0 deep inside the 0-region, and a value of π deep inside the π region. Supposed that the critical current densities in both halves of the $0-\pi$ junction are equal, the ground state of the system consists of a spontaneously formed vortex of supercurrent circulating around the $0-\pi$ boundary. This supercurrent corresponds to a local magnetic flux $|\Phi| \leq \Phi_0/2$, where $\Phi_0 = h/2e$ is the magnetic flux quantum [BKS78; XMT95; GKK02]. Thus, the localized magnetic field is called *semifluxon*. In the framework of this thesis, we examine *triplets*, $0-\pi$ junctions with their respective 0 and π reference junctions. Samples of different geometries (linear and annular) and of different lengths (ranging from the short to the long junction limit) are available. The junctions are realized in overlap geometry, using Nb/Al-Al₂O₃/Ni₆₀Cu₄₀/Nb technology [WTK06; WSK07].

The aim of this thesis was twofold: First, we wanted to figure out whether the additional ferromagnetic interlayer of SIFS junctions modifies the Josephson physics or leads to additional noise contributions in contrast to conventional SIS Josephson junctions, both in the thermal and in the quantum regime. As a second aim, we studied the properties of $0-\pi$ junctions and characterized the associated fractional flux in detail.

We determined the static and dynamic properties of our samples by measuring current-voltage characteristics, IVCs, and by measuring the critical current I_c vs. applied magnetic field B , $I_c(B)$. The experiments were performed using a standard ⁴He- and ³He-cryostat. As a result, $I_c(B)$ of the reference junctions and of the $0-\pi$ junctions showed a small offset from zero magnetic field. Additionally, $I_c(B)$ of the $0-\pi$ Josephson junctions revealed an asymmetric height of the maxima and bumped side minima. This behavior is most likely due to a finite magnetization of the ferromagnetic layer. Regarding the dynamic properties of the reference junctions, we observed no discrepancy from standard Josephson physics. Depending on the respective experimental conditions, Fiske steps, zero

field steps and Shapiro steps were verified, exactly as expected from theory. In case of short $0-\pi$ junctions, half-integer zero field steps were experimentally verified on the IVCs for the first time. Additionally, we presented the first experimental observation of various metastable fluxon/semifluxon configurations in long $0-\pi$ junctions. Switching current measurements were performed in a dilution refrigerator to study escape mechanisms of the Josephson phase in SIFS junctions. The effective potential height as a function of magnetic field and as a function of temperature was examined using samples in the short limit. Numerical simulations showed, that the activation energy of SIFS Josephson junctions vs. magnetic field can be described in the framework of standard short Josephson junction theory. Performing switching current measurements at different temperatures revealed, that the escape temperatures coincided perfectly with the bath temperatures, for 0 , π as well as $0-\pi$ coupling. Using microwave spectroscopy, we observed harmonic, subharmonic and superharmonic pumping. The experimental data of the eigenfrequencies of short and intermediate length samples showed a perfect agreement with the pointlike junction theory.

Overall we conclude, that we do observe peculiarities of the ferromagnetic interlayer in SIFS Josephson junction. Nevertheless, we did not find any indication for additional noise contributions due to the presence of the ferromagnetic layer. Thus, regarding quantum applications, the usability of SIFS Josephson junctions is not restricted due to poor noise properties. In many aspects, short SIFS samples are well described by the short Josephson junction theory. In the case of $0-\pi$ junctions, we developed a deep understanding of the associated fractional flux. Its occurrence was experimentally observed in several experiments, as it had been predicted in theory.

Contents

Introduction	1
I Basics	5
1 Josephson physics	6
1.1 Superconductivity	6
1.2 The Josephson relations	7
1.3 Short Josephson junctions	10
1.3.1 RCSJ model	10
1.3.2 Magnetic field dependence	13
1.3.3 Resonances in short junctions: Fiske steps and Shapiro steps	15
1.4 Long Josephson junctions	17
1.4.1 The sine-Gordon equation	17
1.4.2 Resonances in long junctions: zero field steps . . .	21
1.5 The pendulum analog	21
2 Fractional vortices in Josephson junctions	24
2.1 $0-\pi$ Josephson junctions	24
2.2 Semifluxons	26
2.3 Static properties of $0-\pi$ junctions: a fingerprint of the semifluxon	30
3 Josephson junctions in the quantum regime	33
3.1 The washboard potential	33
3.2 Escape mechanisms of the Josephson phase in point junctions	35
3.2.1 Thermal activation	35

3.2.2	Macroscopic quantum tunneling	39
3.2.3	Resonant activation	41
3.3	Consequences of finite length and phase discontinuity points on the escape mechanisms	43
4	Josephson junctions with a ferromagnetic barrier	47
4.1	Introduction: history and state of the art	47
4.2	Theory of π junctions	50
4.2.1	Microscopic origin	50
4.2.2	Diffusive vs. clean limit	53
4.3	Fabrication of $0-\pi$ SIFS Josephson junctions with reference junctions	56
II	Results	59
5	Conventional characterization of SIFS Josephson Junctions	60
5.1	Samples and measurement techniques	61
5.2	Static properties of $0-\pi$ SIFS junctions	64
5.2.1	Magnetic field dependence of short $0-\pi$ junctions	64
5.2.2	Magnetic field dependence of long $0-\pi$ junctions	67
5.3	Dynamic properties of short and intermediate SIFS Josephson junctions	75
5.3.1	Half-integer zero field steps	75
5.3.2	Fiske steps	79
5.3.3	Shapiro steps	82
5.4	Dynamic properties of long $0-\pi$ SIFS junctions	85
5.4.1	Experimental data	85
5.4.2	Numerical analysis	86
5.5	Conclusions	89
6	Escape of the Josephson phase in SIFS junctions: From thermal to quantum regime	91
6.1	Samples and measurement techniques	92
6.2	Escape rate measurements of short SIFS Josephson junctions	94
6.2.1	Phase escape in magnetic field	96
6.2.2	Phase escape at different temperatures	103
6.3	Microwave spectroscopy of short and intermediate length SIFS Josephson junctions	108

6.4 Conclusions	115
Summary	117
Zusammenfassung	122
A Samples	128
Bibliography	131

Introduction

In the framework of this thesis, we will present detailed studies on Josephson junctions with a ferromagnetic barrier, so-called SIFS (superconductor-insulator-ferromagnet-superconductor) junctions. Conventional 0 SIS junctions have a current-phase relation $I = I_c \sin \mu$ with $I_c > 0$ and the ground state phase $\mu = 0$. In contrast, SIFS Josephson junctions additionally provide the possibility to realize so-called π junctions. In π Josephson junctions the superconducting wave function changes its sign across the barrier, *i.e.*, shifts its phase by π . Their current phase relation reads $I = I_c \sin \mu$ with $I_c < 0$. $\mu = \pi$ is their ground state. Whether a ferromagnetic SIFS Josephson junction exhibits 0 or π coupling, depends on the thickness of the F-layer d_F . The idea of ferromagnetic π Josephson junctions is rather old: The first one to predict Josephson junctions with a negative critical current was L. Bulaevskii in 1977 [BKS77; BKS78]. He considered Josephson junctions having a barrier with magnetic impurities. Nevertheless, it took more than 20 years until the experimental progress in thin film preparation allowed the fabrication of high-quality S/F heterostructures. The first unambiguous experimental realization of Josephson junctions in the π state was provided by V. V. Ryazanov *et al.* [ROR⁺01]. Henceforward, the interplay between (singlet) superconductivity and ferromagnetism in S/F heterostructures was a topic of growing scientific interest; to date, several groups successfully fabricated SFS or SIFS Josephson junctions [KAL⁺02; BTKP02; SBLC03; WKG⁺06; BSH⁺06; RPB⁺06]. π Josephson junctions are intensively investigated, as they promise important advantages for Josephson junction based electronics [TGB97; TB98], *e.g.* for RSFQ logics, or for Josephson junction based qubits [IGF⁺99; BGI01; YTTM05; YTM06]. Furthermore, SIFS technology provides the possibility to realize so-called 0- π Josephson junctions. The ground state phase in such junctions has a value of 0 deep inside the 0-region, and a value of π deep inside the π re-

gion. The different phase coupling in $0-\pi$ SIFS junctions is realized by the use of a step-like thickness of the ferromagnetic barrier. Supposed that the critical current densities in both halves of the $0-\pi$ junction are equal, the ground state of the system consists of a spontaneously formed vortex of supercurrent circulating around the $0-\pi$ boundary. This supercurrent corresponds to a local magnetic flux $|\Phi| \leq \Phi_0/2$, where $\Phi_0 = h/2e$ is the magnetic flux quantum [BKS78; XMT95; GKK02]. In the case of a very long $0-\pi$ Josephson junction the flux $\Phi = \pm\Phi_0/2$, and thus the localized magnetic field is called *semifluxon*. $0-\pi$ junctions are of fundamental interest as these systems provide semifluxons with a degenerate ground state for applications in quantum systems. Throughout this thesis, we used $0-\pi$ junctions and their respective 0 and π reference junctions, which were fabricated by Martin Weides at the Forschungszentrum Jülich, using Nb/Al-Al₂O₃/Ni₆₀Cu₄₀/Nb technology [WTK06; WSK07].

The motivation of the presented studies is twofold: First, we want to clarify whether the additional ferromagnetic layer in SIFS junctions has any influence on the junction properties, *i.e.*, whether the F-layer modifies the Josephson physics or leads to additional noise contributions in contrast to conventional SIS Josephson junctions. For this purpose, we focus on the investigation of the 0 and π coupled reference junctions. As a second aim, we want to study in detail $0-\pi$ junctions and the associated fractional flux. In contrast to studies on SFS and SIFS junctions published so far, we use so-called triplets for our studies — $0-\pi$ junctions with their respective 0 and π reference junctions. This provides us with a good knowledge about the respective junction parameters. Furthermore, we examine junctions of different geometries (linear and annular) and of different length (ranging from the short to the long junction limit).

This thesis is organized in the following way: The **first part** presents basic physical concepts. The **first chapter** reviews on superconductivity and Josephson physics. Josephson junctions in two limiting cases, the short junction limit and the long junction limit, are described by introducing the RCSJ-model for lumped elements and the sine-Gordon model. Static properties of short junctions are examined by deriving the dependence of the critical current on magnetic field. Regarding the dynamic properties of short and long Josephson junctions, Fiske steps, Shapiro steps and zero field steps are described as resonant steps on current-voltage characteristics. The pendulum analog and a chain of coupled pendula is discussed.

In the **second chapter** basic properties of fractional vortices in Josephson junctions are presented. Here, we concentrate on semifluxons as a

special type of fractional vortices. A theoretical description of $0-\pi$ junctions, as well as of semifluxons is given. Special attention is paid to the distinction between fluxons and semifluxons.

The **third chapter** deals with different escape mechanisms of the Josephson phase and their experimental confirmation. The washboard potential is introduced. Then, a brief description of thermal activation, macroscopic quantum tunneling and resonant activation of the Josephson phase is presented. We discuss how finite length effects and phase discontinuity points influence the effective barrier height of the potential.

The **fourth chapter** introduces the physics of Josephson junctions with a ferromagnetic barrier. We briefly overview the important theoretical and experimental results and comment on the current state of the art. A microscopic description of π junctions is presented, distinguishing between diffusive and clean limit. We conclude this chapter by describing the fabrication process of our SIFS Josephson junctions.

In the **second part** of this thesis the scientific results are reported. **Chapter five** presents a characterization of SIFS Josephson junctions by studying their static and dynamic properties. To examine the static properties, the dependencies of the critical current on magnetic field are measured, concentrating on the differences between short and long $0-\pi$ junctions. To study the dynamic properties, current-voltage characteristics are analyzed in detail. Varying the experimental conditions, Fiske steps, zero field steps and Shapiro steps are observed. Numerical simulations support data analysis. The experiments throughout this chapter are performed using a standard ^4He - and ^3He -cryostat.

Chapter six presents the results of switching current measurements of short SIFS junctions performed in a dilution refrigerator. The respective barrier height was examined as a function of magnetic field and as a function of temperature. Numerical simulations based on the point-like and short junction model support the data analysis. Microwave spectroscopy is used, to determine the eigenfrequencies of short and intermediate length samples.

Finally, the **Summary** concludes this thesis.

Part I

Basics

Chapter 1

Josephson physics

This introductory chapter presents the basic properties of Josephson junctions. First a brief review of superconducting materials and their extraordinary features is given. Then Josephson junctions are introduced and the Josephson relations are presented. We distinguish between two limits: short Josephson junctions and long Josephson junctions. The RCSJ model for Josephson junctions is derived. Static and dynamic properties of short junctions are described, namely their magnetic field dependence and different excitation modes. If the junction area is large in normalized units, this gives rise to rich and diverse junction dynamics. The sine-Gordon equation is presented as a model for long Josephson junctions. Its solutions are given with focus on solitary waves. At the end of this chapter the mechanical model of Josephson junctions is explained - the pendulum analog and its extension, a chain of pendula.¹

1.1 Superconductivity

In 1911 H. Kamerlingh-Onnes discovered that the resistivity of mercury drops to an unmeasurable small value, when cooled down below a critical temperature T_c around 4K [KO11]. This behavior was soon reproduced for many different materials like lead or niobium, and called *superconductivity*. In the observed state current can flow without dissipation, until it reaches a critical value (*critical current* I_c). 22 years later W. Meissner

¹A good introduction into superconductivity and Josephson physics can be found in [Sch97; BK04; Ust09].

and R. Ochsenfeld proved that this state is a new thermodynamically stable state. They showed that in the *superconducting state* materials expel magnetic field from their interior [MO33]. In contrast to ideal conductors this behavior is observed, independently of whether the magnetic field had been switched on before or after cooling below T_c .

A phenomenological theory of superconductivity was published in 1950 by V. L. Ginzburg and L. D. Landau [GL50]. Describing superconductivity as a second order phase transition, V. L. Ginzburg introduced the *superconducting order parameter* Ψ . He derived an expression for two characteristic length scales in superconductors, the *magnetic field penetration depth* λ_L and the *coherence length* ξ . λ_L describes the spatial extension on which magnetic fields are shielded from the interior of a superconductor by screening currents. ξ is the spatial variation where the superconducting order parameter vanishes from its bulk value to zero. The first microscopic theory of superconductivity was introduced in 1957 by J. Bardeen, N. L. Cooper and J. R. Schrieffer (*BCS theory*) [BCS57]. According to their ideas, electrons of opposite momenta and spin interact via phonons of the crystal lattice. This interaction is attractive and couples two electrons into a *Cooper pair*. As the total spin and momentum of Cooper pairs is zero², the Cooper pairs form a common ground state. This common ground state is described by a macroscopic wave function

$$\Psi = \sqrt{n_s} e^{i\theta}, \quad (1.1)$$

which is equivalent to the superconducting order parameter in the Ginzburg-Landau theory. n_s is the density of the Cooper pairs and θ the phase of the superconducting wave function. In the frame of the BCS theory single electrons are excitations of the system and are called *quasiparticles*. An *energy gap* Δ is postulated between the ground state and the quasiparticle excitations. An energy of 2Δ is necessary to break a Cooper pair into two single electrons³.

1.2 The Josephson relations

After the publication of the BCS theory great effort has been undertaken to observe the energy gap experimentally. A very elegant way to study

²This is not true for (all) high T_c d-wave superconductors. In this work only low T_c s-wave superconductors are considered.

³L. P. Gor'kov [Gor59] showed that the superconducting Ginzburg-Landau order parameter is proportional to the energy gap and that near T_c the Ginzburg-Landau theory can be derived from the BCS theory.

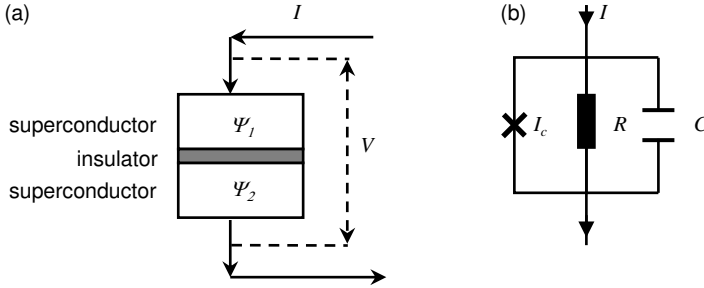


Figure 1.1: (a) Schematic picture of a Josephson junction. The macroscopic wave functions Ψ_1, Ψ_2 are indicated. (b) Equivalent circuit of the RCSJ model of a point junction. The cross represents an element carrying the Cooper pair current.

Δ was to examine tunneling processes between two superconductors, separated by a thin insulating barrier [NSS60; Gia60; CFP62]. In the barrier superconductivity is suppressed: The macroscopic wave functions of both superconductors penetrate into the barrier, but the amplitudes of the wave functions are reduced in comparison to their bulk values. If the barrier is thin enough the superconductors are *weakly* coupled by a small overlap of their macroscopic wave functions.

In 1962 B. Josephson explained the tunneling processes through a weak link as the quantum mechanical tunneling of Cooper pairs. He predicted two effects, the so-called *Josephson effects*. Soon afterwards, systems where two superconducting electrodes are coupled via an insulator, were named *Josephson junctions*, see for example Fig. 1.1 (a)⁴. The properties of a Josephson junction are mainly determined by the phase difference φ between the wave functions of the two superconducting electrodes

$$\varphi = \theta_2 - \theta_1. \quad (1.2)$$

Depending on the phase difference a stationary supercurrent I_s arises which is present at zero voltage

$$I_s = I_c \sin \varphi. \quad (1.3)$$

⁴There are various types of *weak links*. Besides the extensively studied SIS Josephson junctions (superconductor-insulator-superconductor), for this work also SNS (N=normal metal) junctions are important. An overview of further types of weak links is given in [BP82a; GKI04].

Eq. (1.3) is called *dc-Josephson effect*⁵. It should be mentioned here, that φ is gauge-invariant. It was shown [BP82b], that — in the presence of magnetic fields — the phase φ is given by

$$\varphi = \theta_2 - \theta_1 - \frac{2\pi}{\Phi_0} \int_1^2 \vec{A} \cdot d\vec{l}, \quad (1.4)$$

where the integration is performed across the junction, \vec{A} is the vector potential. $\Phi_0 = h/2e = 2.07 * 10^{-15}$ Wb is the *magnetic flux quantum*. I_c is the maximum (critical) current which can be sent dissipationless through the junction. It depends on the material of the superconducting electrodes, the respective barrier properties and the junction area. V. Ambegaokar and A. Baratoff [AB63a; AB63b] derived the critical current I_c of a SIS tunnel junction using a microscopic theory for direct tunneling as

$$I_c(T) = \frac{\pi}{2e} \frac{\Delta(T)}{R_n} \tanh\left(\frac{\Delta(T)}{k_B T}\right). \quad (1.5)$$

R_n is the resistance of the normal state of the tunnel junction, e denotes the electron charge, $\Delta(T)$ is the temperature dependent energy gap and k_B is the Boltzmann constant. At temperatures close to zero the critical current I_c is related to the normal resistance R_n as

$$I_c(0) = \frac{\pi}{2e} \frac{\Delta(0)}{R_n}. \quad (1.6)$$

In equilibrium the phase difference φ is not time dependent and the Cooper pair supercurrent is constant. If the phase difference φ is varying in time, a time-dependent voltage $U_J(t)$ occurs across the junction:

$$\frac{\partial \varphi}{\partial t} = \frac{2\pi}{\Phi_0} U_J(t). \quad (1.7)$$

Eq. (1.7) is called *ac-Josephson effect*. Using $V = \langle U_J(t) \rangle = \frac{\Phi_0}{2\pi} \dot{\varphi}$, one can calculate the time-averaged voltage drop across the junction. On the other hand, if a constant voltage is applied to the junction, Eq. (1.7) implies that the supercurrent through the junction oscillates with a frequency,

$$f_J = V/\Phi_0 = \left[\frac{483.6 \text{ MHz}}{\mu\text{V}} \right] V. \quad (1.8)$$

⁵Actually, Eq. (1.3) is a first-order-approximation of the supercurrent which is valid for SIS tunnel junctions; contributions of higher order, which are important for other types of Josephson junctions, will be discussed later, see Chap. 4.

Hence a Josephson junction converts dc voltage into an oscillating current, and acts like a nonlinear inductor in a circuit. The *Josephson inductance* L_J can be derived as

$$L_J = \frac{L_{J,0}}{\cos \varphi} \quad (1.9)$$

with $L_{J,0} = \Phi_0/2\pi I_c$.

1.3 Short Josephson junctions

1.3.1 RCSJ model

The dynamic behavior of a pointlike⁶ Josephson junction is described by a lumped circuit model, see Fig. 1.1 (b). The junction is represented by a parallel circuit of three different elements: an *ideal* Josephson junction, a resistor and a capacitor⁷. The first element is a nonlinear element obeying the Josephson relations Eqs. (1.3) and (1.7). The resistor takes the quasiparticle tunneling into account. Thirdly, a Josephson junction has a finite capacitance. This gives rise to a displacement current due to the time-dependent nature of the Josephson current. This model is called resistively and capacitively shunted junction model (*RCSJ-model*), proposed by W. C. Stewart and D. E. McCumber in 1968 [Ste68; McC68]. Applying Kirchhoff's rules to the circuit shown in Fig. 1.1 (b) the total current through a lumped Josephson junction is given by

$$I = I_c \sin \varphi + U_J/R + C\dot{U}_J. \quad (1.10)$$

I_c is critical current of the junction, C is its capacitance and I is the applied bias current⁸. R is the respective resistance, which in general depends on the voltage. Here, a linear dependence of the quasiparticle

⁶To be precise, one has to distinguish between a *pointlike* Josephson junction and a *short* junction. A pointlike junction is a theoretical simplification, assuming that there is no spatial variation of the phase difference across the junction. A short junction takes the spatial extension of real Josephson junctions into account, the phase difference may vary in space. A junction is short, if the lateral dimensions of the Josephson junction are small in normalized units, i.e., small in comparison to the Josephson penetration depth λ_J (see Chap. 1.4)

⁷For means of simplicity a noise contribution is neglected.

⁸As the resistance of Josephson junctions is small, usually of the order of 1Ω or less, in this work standard measurements are performed *current-biased*, i.e., a bias current is applied and the respective voltage drop across the Josephson junction is measured, compare Fig. 1.1 (a).

contribution is assumed (if necessary, the RCSJ model can be extended to a nonlinear version which takes the nonlinearity of $R(U_J)$ into account). Using Eq. (1.7) and normalizing the time to the inverse of the *Josephson plasma frequency*, i.e., $dt = \omega_P^{-1} d\tau$, with

$$\omega_P = 1/\sqrt{L_{J,0}C} = \sqrt{\frac{2\pi I_c}{C\Phi_0}} \quad (1.11)$$

we obtain the equation of motion for the phase difference

$$\gamma = I/I_c = \sin \varphi + \frac{1}{\sqrt{\beta_c}} \dot{\varphi} + \ddot{\varphi}. \quad (1.12)$$

In this notation the dots represent time derivatives with respect to the normalized time. The bias current I through a Josephson junction is normalized to the critical current I_c and is called γ . The Josephson plasma frequency ω_P is the resonance frequency of the circuit which is formed by the Josephson inductance $L_{J,0}$, see Eq. (1.9), and the capacitance C . This frequency determines the time scale of dynamical processes in the junction. The *McCumber parameter* β_c is given as

$$\beta_c = \frac{2\pi I_c R^2 C}{\Phi_0} \quad (1.13)$$

with $\beta_c = 1/\alpha^2$. α is the *damping coefficient*. $Q = \sqrt{\beta_c} = \omega_P RC$ is the *quality factor* of the junction.

Current-voltage characteristics

The dynamic properties of Josephson junctions are experimentally studied by measuring *current-voltage characteristics* (IVC). A bias current is applied and simultaneously the (time averaged) voltage drop V across the junction is measured in a standard four-point measurement. Two exemplary *IV* characteristics are shown in Fig. 1.2, one of an underdamped (a)/(c) and one of an overdamped (b) sample. Here, we concentrate on underdamped IVCs⁹. In contrast to overdamped ($\alpha > 1$) Josephson junctions, underdamped ($\alpha < 1$) Josephson junctions show a hysteretic behavior, see Fig. 1.2 (a)/(c). Their current-voltage correlation is bistable as for some current values the resistive state and the superconducting state are both solutions of the system. Three regimes

⁹IVCs are used throughout this thesis to study dynamic properties, thus we mainly deal with junctions in the underdamped limit when we study IVCs.

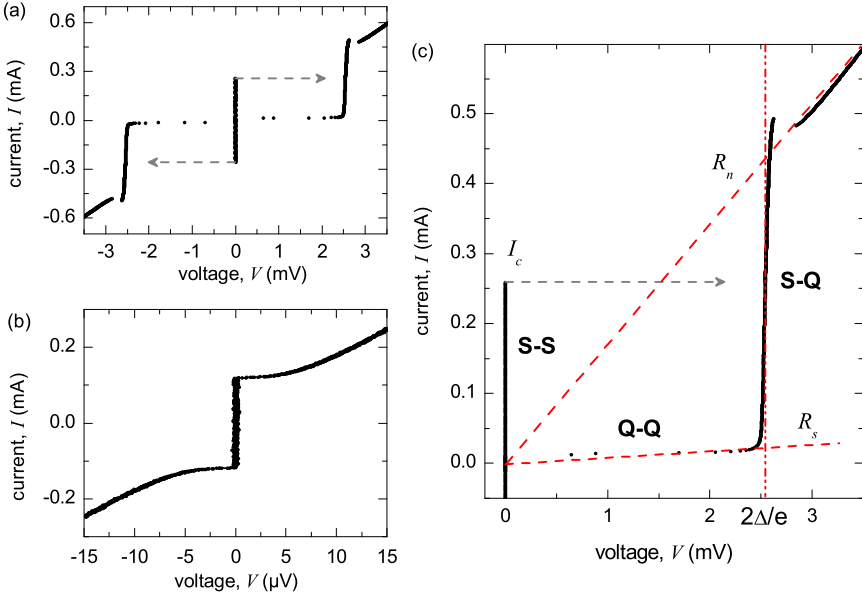


Figure 1.2: (a) IVC of a short Josephson junction in the underdamped limit at $T = 4.2$ K. *Hypres*, $5 \times 5 \mu\text{m}^2$, Nb/Al-Al₂O₃/Nb-trilayer technology. (b) IVC of a SIFS 0 junction in the overdamped limit at $T = 4.2$ K. $50 \times 50 \mu\text{m}^2$, Nb/Al-Al₂O₃/Ni₆₀Cu₄₀/Nb technology. (c) Enlargement of (a); R_n is the normal resistance, R_s the subgap resistance and I_c the critical current of the junction. Different tunnel regimes (S-S, S-Q, Q-Q) are indicated.

can be distinguished. The state with $V = 0$ is referred to as zero voltage state. The bias current is increased from zero to a critical value I_c . Up to this value, no voltage drop occurs across the junction, the current is carried only by Cooper pair tunneling (S-S). If the critical current is reached, the junction switches to the resistive state¹⁰ with $V \neq 0$. Since the Cooper pairs are now oscillating with zero net current the dc part of the current is carried by quasiparticles. The resistance of the junction is strongly nonlinear and depends on the respective voltage. If the currents are large (and thus the voltage is above the gap voltage $V_g = 2\Delta/e$), enough energy is transferred to the system to break the Cooper pairs during tunneling (S-Q). Then, the resistivity of the junc-

¹⁰The term "resistive" state might be misleading as the junction electrodes are still superconducting.

tion approaches the normal state resistance R_n . In case of SIS Josephson junctions, shown in Fig. 1.2, the precise shape of the gap region is influenced by the aluminum layer of the junctions. If the Al is not fully oxidized to Al_2O_3 , a so-called proximity-knee is visible: the small hysteretic regime around the gap [Ust09]. At voltages below the gap voltage V_g , the dc current is due to tunneling of quasiparticle (Q-Q) which are thermally excited. They give rise to the *subgap resistance* R_s . Thus this branch is called the *subgap branch* or *McCumber-branch*. As the occurrence of these quasiparticles is temperature dependent, R_s changes with temperature ($R_s \sim \exp(\Delta/k_B T)$). Decreasing the current on the McCumber branch of an underdamped Josephson junction at a certain current value, the so-called *return current* I_r , the junction switches back to the zero voltage state. The actual value of I_r depends on β_c and is influenced by several types of fluctuations [CFL88].

Whether a Josephson junction is underdamped or overdamped depends on the junction parameters, the junction type and the experimental conditions. As the damping parameter strongly depends on I_c , R and C , compare Eq. (1.13), these parameters are used — within the limits of the fabrication process — to adjust a junction to the desired properties. SIS Josephson junctions have a high resistance due to the oxide layer, thus they are usually underdamped at 4.2 K. In contrast to this, SFS (F=ferromagnet) Josephson junctions show a very low resistance and are thus overdamped at 4.2 K. Additionally, in an experiment the junction properties can often be changed from the underdamped to the overdamped limit, *e.g.*, by increasing or decreasing the temperature and the critical current, respectively.

1.3.2 Magnetic field dependence

As pointed out in Sec. 1.2, an externally applied magnetic field influences the phase difference via the vector potential. Since φ changes in the presence of magnetic field, so does the supercurrent I_s . The aim of this section is to derive the dependence of the critical current on magnetic field. Here, short junctions are considered, *i.e.*, the phase difference across the junction varies linearly in space (in one dimension).

An external magnetic field is applied in plane of the junction, see Fig. 1.3 (a). Magnetic field enters into the barrier and into the surface of the superconducting electrodes. The *effective magnetic thickness* d determines the penetration depth

$$d = 2\lambda_L + t_{\text{ox}}. \quad (1.14)$$

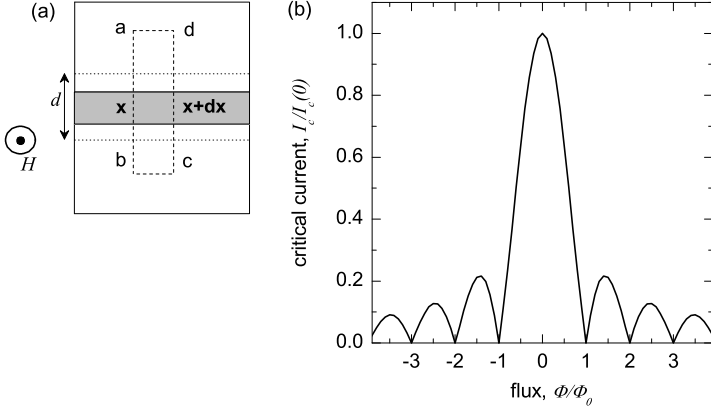


Figure 1.3: (a) Schematic cross section of a Josephson junction. A closed path including the barrier is indicated as a dashed line. d is the magnetic thickness of the junction. \mathbf{x} and $\mathbf{x}+d\mathbf{x}$ are two points inside the barrier. The magnetic field is oriented parallel to the plane of the junction. (b) Theoretically calculated dependence of the critical current on magnetic field.

t_{ox} is the thickness of the barrier¹¹. The magnetic flux inside the dashed contour is calculated as

$$\Phi = \oint \vec{A} \cdot d\vec{l} = \int_a^b \vec{A} \cdot d\vec{l} + \int_b^c \vec{A} \cdot d\vec{l} + \int_c^d \vec{A} \cdot d\vec{l} + \int_d^a \vec{A} \cdot d\vec{l}. \quad (1.15)$$

Replacing the first and third term in Eq. (1.15) by the gauge-invariant phase differences $\varphi(x)$ and $\varphi(x+dx)$ using Eq. (1.4), one gets

$$\frac{2\pi\Phi}{\Phi_0} = \varphi(x+dx) - \varphi(x) + \frac{2\pi}{\Phi_0} \left[\int_b^c \vec{A}(S) \cdot d\vec{l} + \int_d^a \vec{A}(R) \cdot d\vec{l} \right]. \quad (1.16)$$

The second and fourth term in Eq. (1.15) vanish, if the points a, b, c and d are chosen considerably deep inside the superconductors. Furthermore, the magnetic flux inside the dashed contour can be calculated as $\Phi = \mu_0 H d \times dx$, μ_0 is the vacuum permeability. Combining this with the equations Eq. (1.16) and Eq. (1.15) yields

$$\frac{\varphi(x+dx) - \varphi(x)}{dx} = \frac{d\varphi}{dx} = \frac{2\pi}{\Phi_0} \mu_0 d H, \quad (1.17)$$

¹¹Eq. (1.14) is an approximation [Wei69] valid in the limit of thick superconducting electrodes.

A constant magnetic field H causes a constant gradient of the phase difference across the junction. Inserting the integrated form of Eq. (1.17) into Eq. (1.3) results in¹²

$$I = \int_A j_c \sin \left(2\pi \frac{\mu_0 d H x}{\Phi_0} + C \right) dA. \quad (1.18)$$

Here, A is the area of the junction, $j_c = I_c/A$ is the critical current density. If j_c is considered to be homogeneous, Eq. (1.18) can be integrated¹³ in order to obtain the magnetic field dependence of the critical current I_c

$$I_c(H) = \left| I_c(0) \frac{\sin(\pi\Phi)/\Phi_0}{\pi\Phi/\Phi_0} \right|. \quad (1.19)$$

$I_c(0) = j_c(0) * A$ is the maximum supercurrent without applied magnetic field. Here, $\Phi = \mu_0 H d L$ with L being the length of the junction. The Josephson current oscillates sinusoidally with the coordinate perpendicular to the field. Eq. (1.19) is often called *critical-current diffraction pattern*, as its shape resembles the Fraunhofer pattern in optics. Its dependence is plotted in Fig. 1.3 (b) ($I_c(H)$ pattern). At the nulls of the critical current the junction length is an integer number of the wavelength of the supercurrent density oscillations. Therefore the supercurrent flows equally in both directions across the junction, resulting in a zero net current.

1.3.3 Resonances in short junctions: Fiske steps and Shapiro steps

Under certain experimental conditions, *resonances* are visible as fine-structures on the IVCs of Josephson junctions, often showing a regular voltage-spacing. Two types of resonances will be reviewed in the following: *Fiske steps* and *Shapiro steps*¹⁴. Both occur in short junctions due to synchronization processes.

¹² C is an arbitrary integrating constant, which has to be taken into account when one integrates Eq. (1.17).

¹³The result is maximized regarding the free parameter C .

¹⁴A nice introduction to the physics of Fiske steps and Shapiro steps can be found in [Sch97; Ust09].

Fiske steps

Fiske steps appear on the IVCs of Josephson junctions when measurements are performed in the presence of a magnetic field. As described in Sec. 1.3.2, the Josephson supercurrent oscillates sinusoidally if a magnetic field is applied in plane of the junction. Its oscillation wavelength is determined by the field value. If the wave vectors of these oscillations match the electromagnetic cavity modes of the junction, equally spaced resonant steps are visible on the IVCs. The resonance number n determines the number of half-wave lengths of the standing waves. The asymptotic voltage of the n -th Fiske step is given by

$$V_n^{\text{FS}} = n \frac{\Phi_0 \bar{c}}{2L}. \quad (1.20)$$

L is the length of the junction, \bar{c} is the *Swihart velocity*, compare Sec. 1.4. A complete analytical theory of Fiske steps was developed by I. O. Kulik [Kul65].

Shapiro steps

If a voltage drop occurs across a Josephson junction the supercurrent will oscillate with a frequency according to Eq. (1.8). If the junction is additionally irradiated by electromagnetic waves (microwaves), the oscillating supercurrent can lock onto the frequency of the irradiated microwaves. This locking mechanism leads to equally spaced steps of constant voltage on the current-voltage characteristics with

$$V_m = m f_{\text{ac}} \Phi_0. \quad (1.21)$$

$m = 0, \pm 1, \pm 2 \dots$ are the numbers of the respective Shapiro steps, f_{ac} is the frequency of the externally applied microwaves. Depending on the McCumber damping parameter, the microwave power of the externally applied microwaves (and thus the amplitude of the induced oscillating current I_{ac}) and the microwave frequency f_{ac} , the height of the Shapiro steps shows an oscillating behavior. If junctions in the overdamped limit are, *e.g.*, irradiated with frequencies close to the Josephson plasma frequency ($f_{\text{pl}} = \omega_P/2\pi$), the height of the Shapiro steps ΔI_m is approximated as

$$\Delta I_m \sim 2I_c |J_m(x)|. \quad (1.22)$$

I_c is the critical current of the junction, J_m is the m -th Bessel function. The argument x is proportional to I_{ac}/I_c . For $m = 0$, one gets the height

of the critical current as a function of applied microwave power. In the underdamped case Shapiro steps often show a hysteretic behavior. Their analysis is rather complicated and has gained considerable interests as it was studied in relation to the chaotic behavior of Josephson junctions.

1.4 Long Josephson junctions

In the following, *long* Josephson junctions are considered. A schematic drawing of a long Josephson junction is shown in Fig. 1.4. A long Josephson junction is defined as a spatially extended junction, whose length L in one dimension is larger than the *Josephson penetration depth* $L \geq \lambda_J$. The width W is usually smaller than λ_J . λ_J is the characteristic length scale of spatial variation of the phase difference φ , compare Fig. 1.4. As $\partial\varphi/\partial x \sim H$ the Josephson penetration depth indicates, how far magnetic field can penetrate into an extended Josephson junction.

1.4.1 The sine-Gordon equation

To derive the equation of motion of a long Josephson junction a lumped circuit model is used, see Fig. 1.5. A long junction is remodeled by an array of RCSJ-type lumped Josephson junctions. They are connected in parallel via superconducting electrodes. The spacing between neighboring junctions is dx . The superconducting electrodes are approximated

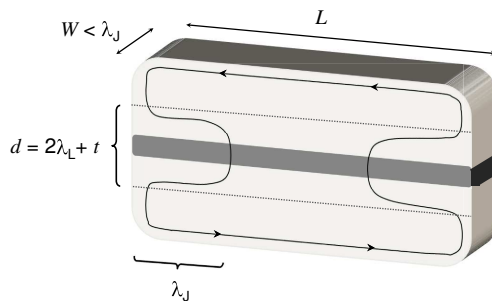


Figure 1.4: Schematic drawing of a linear long Josephson junction. L is the length of the junction, W is its width, d is the magnetic thickness. λ_J is the Josephson penetration depth. Circulating supercurrents are indicated by arrows.

as a parallel connection of an inductance L^* and a resistance R_s^* . The subscript s stands for surface, as the surface resistance of the Josephson junction is considered. Here, $L^* = L/\Delta x$, $C^* = C/\Delta x$, $j = I/\Delta x$, $\rho = R^*\Delta x$, $\rho_s = R_s^*\Delta x$, with Δx being a small section of the long junction. The current through node A is calculated according to Kirchoff's rules, compare [Ust09] or [BP82b]

$$\frac{\partial(I_1 + I_2)}{\partial x} = j - C^* \frac{\partial U_J}{\partial t} - \frac{U_J}{\rho} - j_c \sin \varphi, \quad (1.23)$$

with

$$I_1 = -\frac{\Phi_0}{2\pi L^*} \frac{\partial \varphi}{\partial x} \quad \text{and} \quad (1.24)$$

$$I_2 = -\frac{1}{\rho_s} \frac{\partial U_J}{\partial x}. \quad (1.25)$$

With $L^* = \mu_0 d$ being the specific inductance, $C^* = \epsilon\epsilon_0/t_{\text{ox}}$ being the specific capacitance, j_c the critical current density, j the bias current density, ρ the quasiparticle resistance per unit length, and using the ac-Josephson relation Eq. (1.7), Eq. (1.23) is transformed. Subsequently it is normalized using

$$\frac{t}{\omega_p^{-1}} \rightarrow t \quad \text{with} \quad \omega_p = \sqrt{\frac{2\pi j_c}{\Phi_0 C^*}} \quad (1.26)$$

$$\frac{x}{\lambda_J} \rightarrow x \quad \text{with} \quad \lambda_J = \sqrt{\frac{\Phi_0}{2\pi L^* j_c}}. \quad (1.27)$$

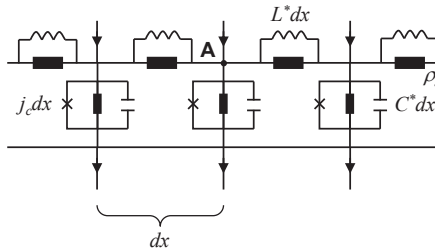


Figure 1.5: Lumped circuit model of a long Josephson junction.

ω_P is the Josephson plasma frequency. Thus, we normalize the spatial coordinate to the Josephson penetration depth and the time to the inverse Josephson plasma frequency. Eq. (1.23) can therefore be rewritten as

$$\varphi_{xx} - \varphi_{tt} = \sin \varphi + \alpha \varphi_t - \beta \varphi_{xxt} - \gamma. \quad (1.28)$$

A compact notation for the derivatives is introduced

$$\varphi_{xx} \equiv \frac{\partial^2 \varphi}{\partial x^2}; \quad \varphi_{tt} \equiv \frac{\partial^2 \varphi}{\partial t^2}; \quad \varphi_t \equiv \frac{\partial \varphi}{\partial t}; \quad \varphi_{xxt} \equiv \frac{\partial^3 \varphi}{\partial x^2 \partial t}. \quad (1.29)$$

Eq. (1.28) is called *perturbed sine-Gordon equation*. It is the equation of motion of 1-D long Josephson junctions. The respective boundary conditions can be adjusted to consider geometrical aspects and experimental conditions. The last three dimensionless coefficients in Eq. (1.28) are defined as

$$\alpha = \sqrt{\frac{\Phi_0}{2\pi j_c \rho_s^2 C^*}}, \quad (1.30)$$

$$\beta = \sqrt{\frac{2\pi j_c L^{*2}}{\Phi_0 C^* \rho_s^2}}, \quad (1.31)$$

$$\gamma = \frac{j}{j_c}. \quad (1.32)$$

α is the damping coefficient, β is a damping term which is due to surface losses of the superconducting electrodes and γ is the normalized bias current density. If the last three terms in Eq. (1.28) are small, they are called *perturbations*. In a simplified ansatz the perturbations are neglected and the classical *sine-Gordon equation* is solved

$$\varphi_{xx} - \varphi_{tt} = \sin \varphi. \quad (1.33)$$

To obtain an exact solution, an infinitively long junction is considered. The boundary conditions are given as

$$\varphi_x|_{x=\pm\infty} = 0. \quad (1.34)$$

There is a rich spectrum of linear and nonlinear electromagnetic excitations, which are solutions of Eq. (1.33). The most prominent solution throughout this thesis is

$$\varphi(x, t) = 4 \arctan \left[\exp \left(\pm \frac{x - vt - x_0}{\sqrt{1 - v^2}} \right) \right], \quad (1.35)$$

which describes a solitary wave, a soliton. It consists of a circulating supercurrent, which produces magnetic flux. Due to flux quantization in superconductors, this magnetic flux is equal to one magnetic flux quantum Φ_0 . It is hence called *Josephson fluxon* or *Josephson vortex*. As described before, Eq. (1.35) solves the ideal case of the unperturbed sine-Gordon equation. In experiment, always a bias current is applied and losses due to damping cannot be neglected. If a bias current is applied to the junction, due to the Lorentz force the fluxon is driven through the system with a normalized velocity $|v| \leq 1$. An *energy balance approach* shows [MS78; KM89], that in this case dissipation losses are compensated by the driving force. The soliton solution is still valid. For a given driving force and damping parameter a fluxon reaches a steady motion with a certain velocity. Eq. (1.35) is invariant with respect to a Lorentz transform. Thus, if the velocity of the fluxon is increased, its size shrinks due to Lorentz contraction and the magnetic field in its interior is increased. The limiting velocity for fluxons and electromagnetic waves in Josephson junctions is the *Swihart velocity* \bar{c}

$$\bar{c} = \lambda_J \omega_p. \quad (1.36)$$

\bar{c} is usually a few percent of the velocity of light in vacuum.

The simplest solution of the sine-Gordon equation is obtained in the small amplitude limit $\varphi \ll 1$, by linearizing Eq. (1.33). This results in linear wave solutions of the form

$$\varphi(x, t) = \varphi_0 \exp(i[kx - \omega t]), \quad (1.37)$$

where k is the wave vector and ω is the frequency of the linear waves. Again, $\varphi_0 \ll 1$. These small amplitude waves (electromagnetic waves) in Josephson junctions are named *Josephson plasma waves*. By substituting Eq. (1.37) into Eq. (1.33) the dispersion relation of the linear waves is calculated as

$$\omega = \sqrt{1 + k^2}. \quad (1.38)$$

The gap in the spectrum for small wave numbers is a characteristic feature of Josephson plasma waves. By measuring Fiske steps, plasma waves in Josephson junctions can be directly detected, see Subsec. 1.3.3. There are various other types of solutions existing for Eq. (1.33), like bound states of vortices and antivortices. For further information see [BP82b] or [Ust09].

1.4.2 Resonances in long junctions: zero field steps

As described for short Josephson junctions, resonant steps are observable on the IVCs of long Josephson junctions. Fiske steps and Shapiro steps can be measured as reviewed in Sec. 1.3.3. An additional type of equally spaced voltage steps, characteristic for long junctions, are *zero field steps*. Here, as indicated by the name, IVCs are taken in the absence of magnetic field. Physically, zero field steps are due to a spontaneous creation of Josephson vortices. The bias current through the junction is increased until the junction switches to the voltage state. Then, the bias current is reduced again. If this process is executed in the underdamped limit, a vortex (or antivortex)¹⁵ is created spontaneously due to some parametric instabilities. The vortex (or antivortex) is driven through the junction by the bias current and is reflected at the boundary as an antivortex (or vortex). These vortex/antivortex pairs are observed as resonant steps on the IVCs. It can be shown [BP82b], that the voltage position of zero field steps is calculated as

$$V_n^{\text{ZFS}} = \frac{\Delta\Phi}{\Delta t} = n \frac{2\Phi_0\bar{c}}{2L} = n \frac{\Phi_0\bar{c}}{L}, \quad (1.39)$$

n is the number of the n -th ZFS, thus n vortices (or antivortices) per time unit are cycling in the junction. Note, that the voltage spacing between zero field steps is twice larger than the voltage spacing of Fiske steps.

1.5 The pendulum analog

The equation of motion Eq. (1.12) of the phase difference across a short Josephson junction is identical to the differential equation which describes the dynamics of a damped, driven pendulum

$$K = mgL \sin \varphi + \kappa \dot{\varphi} + \Theta \ddot{\varphi}. \quad (1.40)$$

Here, K is the externally applied torque, m is the mass of the pendulum, L is its length and g is the acceleration due to gravity. φ is the angle of deflection of the pendulum. κ is the damping coefficient and Θ is the

¹⁵In annular junctions, a vortex+antivortex pair is created and forms a ZFS. This is due to topological constrictions in annular junctions. In linear junction only a vortex *or* only an antivortex is formed spontaneously. Thus, the voltage spacing of ZFS in annular junctions is twice larger than the voltage spacing of ZFS in linear junctions.

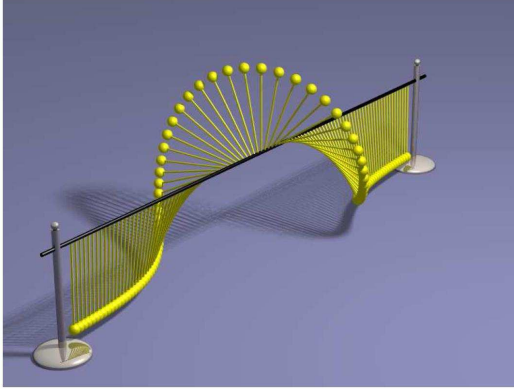


Figure 1.6: Mechanical model of a long Josephson junction: a chain of strongly coupled pendula. A fluxon is visible as a 2π turn. By courtesy of Dr. E. Goldobin.

momentum of inertia.

The analogy is pretty obvious: As a pendulum is deflected by an external torque K , the Josephson junction is driven by the bias current I . The phase difference between the two superconductors of a Josephson junction is equivalent to the angle of deflection of a pendulum. If the torque $K \leq mgL$ ($mgL \leftrightarrow I_c$), the pendulum is displaced by a certain angle. This state is stationary and corresponds to the zero voltage state of a Josephson junction. If the phase varies with time, in the case of a Josephson junction a voltage drop occurs. In the mechanical model the pendulum is rotating. Hence this state is called *whirling state* in both cases.

In the pendulum model the hysteretic behavior of the IV curve of a short *underdamped* Josephson junction is easily understood. Increasing torque is applied to the pendulum, until it starts rotating. When the driving force is subsequently decreased, the pendulum is decelerating. However, due to the inertia of the pendulum, the pendulum still rotates when the driving force is decreased below mgL . Depending on the damping coefficient, the pendulum can remain in the whirling state, even if the torque becomes very small. This explanation can be directly transferred to a short Josephson junction. Thus, the pendulum is a clear and demonstrative model to facilitate the understanding of Josephson physics.

As a short junction is described by the pendulum analog, a *long* Josephson junction is resembled by a chain of strongly coupled pendula, see

Fig. 1.6. In the mechanical model a fluxon is equal to a 2π -kink. If a kink is introduced into the system, the phase φ in the chain of pendula changes from zero to 2π . The two signs \pm in Eq. (1.35) account for the fact, that there is also an antikink solution. An antikink moves through the system with the same velocity as the kink, but in opposite direction. In Fig. 1.6 a fluxon is visible as a 2π twist in a chain of pendula.

Chapter 2

Fractional vortices in Josephson junctions

The following chapter introduces fractional vortices in Josephson junctions. We concentrate on *semifluxons* as a special type of fractional vortices¹. A fully-developed semifluxon carries a magnetic flux of $|\Phi_0/2|$, half of the magnetic flux quantum [BKS78; XMT95; GKK02]. Semifluxons are observed in so-called $0-\pi$ *Josephson junctions* which we discuss in the first section. Then, we examine the properties of semifluxons, paying special attention to the differences between fluxons and semifluxons. The consequences of the presence of semifluxons on the static properties of short and long $0-\pi$ junctions are reviewed.

2.1 $0-\pi$ Josephson junctions

Up to now in this thesis only conventional Josephson junctions were discussed. Conventional junctions are also called “ 0 Josephson junctions” because they have a current-phase relation of $I = I_c \sin \mu$ with $I_c > 0$ and the ground state phase² $\mu = 0$. Additionally, so-called “ π Josephson

¹In this thesis, we do not deal with *fractional* φ -vortices which are realized by using standard SIS junctions with a pair of tiny injectors. In these systems, the *topological* charge φ of the fractional vortex is freely selectable. By sending an arbitrary current through the injectors, in these systems an *arbitrary* phase shift can be created, see *e.g.* Refs. [GSG⁺04; GSKK04; BGS⁺07].

²In this chapter it is necessary to distinguish between the Josephson phase φ and the magnetic phase difference $\mu = \varphi - \theta$, with θ being an intrinsic phase difference.

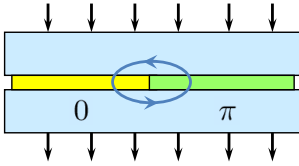


Figure 2.1: Schematic drawing of a $0-\pi$ Josephson junction. The 0 part is colored in yellow (light gray), the π part in green (dark gray). The semifluxon is depicted as a circulating current around the discontinuity point. The bias current is represented by arrows.

junctions” exist. In such structures the superconducting wave function changes its sign, *i.e.*, shifts its phase by π . This leads formally to a negative critical current I_c and the current-phase relation reads $I = I_c \sin \mu$ with $I_c < 0$. A π junction has $\mu = |\pi|$ in the ground state, *i.e.*, when no bias current is applied. Usually in experiment, it is sophisticated to distinguish a single 0 junction and a single π junction³. π Josephson junctions are intensively investigated, as they promise important advantages for Josephson junction based electronics. They are supposed to improve the performance of various classical and quantum electronic circuits, *e.g.*, they can be used in RSFQ logics [TGB97; TB98] to self bias the circuit and to reduce the number of bias resistors [OAM⁺06] and inductances [UK03]. In particular, they are suggested for Josephson junction based qubits [IGF⁺99; BGI01; YTTM05; YTM06].

Nowadays, several technologies allow to manufacture π junctions: Josephson junctions with a ferromagnetic barrier [ROR⁺01; KAL⁺02; OBF⁺06; WKG⁺06], nonequilibrium superconductor – normal metal – superconductor Josephson junctions [BMWK99; HPH⁺02] and quantum dot junctions [vDNB⁺06; CWB⁺06; JNGR⁺07]. There is a rather new suggestion to realize geometric π junctions in d-wave superconducting thin films [GIS07].

Furthermore, one can fabricate $0-\pi$ Josephson junctions. A schematic drawing of a $0-\pi$ junction is shown in Fig. 2.1. The ground state phase in such junctions has a value of 0 deep inside the 0-region (colored in yellow, light gray), and a value of π deep inside the π region (green, dark gray). There are several technologies to realize $0-\pi$ Josephson junctions. They were fabricated by utilizing d-wave superconductors [TK00; SAB⁺02; VH95; HAS⁺03; LTR⁺02] or were obtained by chance using a ferromagnetic barrier [DRAK⁺05; FVHB⁺06]. A very elegant way to produce symmetric and tunable $0-\pi$ junctions is the use of stan-

For 0 SIS junctions, $\mu = \varphi$. A precise definition of μ is presented below.

³There are phase-sensitive experiments like [ROVR01].

standard SIS junctions with a pair of tiny injectors (actually, these junctions allow one to study junctions with *arbitrary* phase shifts and thus arbitrary fractional vortices). A symmetric $0-\pi$ SIFS Josephson junction with two reference junctions was demonstrated recently [WKK⁺06].

To derive the equation of motion of the Josephson phase in a long $0-\pi$ junction [GKK02], the perturbed sine-Gordon equation (1.28) is modified by an additional term

$$\varphi_{xx} - \varphi_{tt} = \sin \varphi + \alpha \varphi_t - \beta \varphi_{xxt} - \gamma(x) + h_x(x) + \theta_{xx}(x). \quad (2.1)$$

As introduced in Sec. 1.4.1, $\alpha = 1/\sqrt{\beta_c}$ is the damping constant, β is a damping constant due to surface losses and $\gamma(x)$ is the normalized bias current density. $h(x) = 2H(x)/H_{c1}$ is the normalized magnetic field, with $H_{c1} = \Phi_0/(2\pi\mu_0 d\lambda_J)$. The last term takes the $0-\pi$ boundary into account: $\theta(x)$ is a step function which has a constant value of 0 or π and is π -discontinuous at the $0-\pi$ boundary. Thus, θ is the intrinsic phase difference of the system, it is order parameter-related. In general, if a junction has several $0-\pi$ discontinuities at different positions x_k , $\theta_{xx}(x)$ can be written as

$$\theta_{xx}(x) = \pi \sum_k \sigma_k \frac{\delta_k}{x} (x - x_k). \quad (2.2)$$

To simplify the analysis (especially for numerical investigations), it is convenient to replace the Josephson phase φ by the sum of two components:

$$\varphi(x, t) = \mu(x, t) + \theta(x). \quad (2.3)$$

We introduce the magnetic component μ , which is continuous. The physics of the system is governed by the magnetic component, as the magnetic field of the Josephson supercurrent and the energy of the systems is $\sim \mu_x$, see below. Eq. (2.1) can be rewritten for the magnetic component μ as

$$\mu_{xx} - \mu_{tt} = \cos[\theta(x)] \sin \mu + \alpha \mu_t - \beta \mu_{xxt} - \gamma(x) + h_x(x). \quad (2.4)$$

Eq. (2.4) is equivalent to the perturbed sine-Gordon equation Eq. (1.28).

2.2 Semifluxons

The pendulum model of a $0-\pi$ junction is shown in Fig. 2.2. The π shift of the total phase φ at the discontinuity point is realized as the

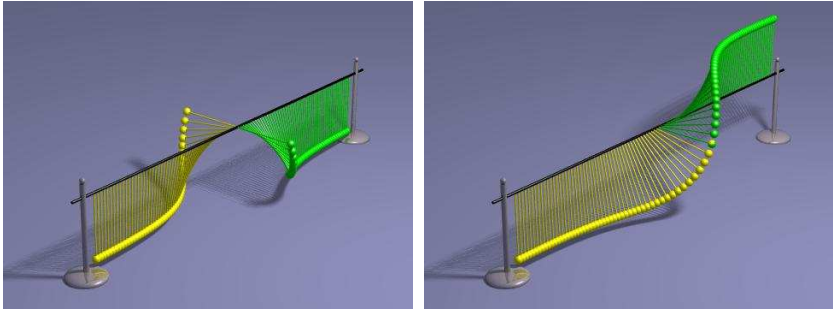


Figure 2.2: Pendulum model of a semifluxon in a long $0-\pi$ junction. On the left side the total phase φ is shown, on the right side the continuous magnetic component μ . By courtesy of E. Goldobin.

coupling of a fixed angle of 180° between two adjacent pendula (yellow and green), see left hand side of Fig. 2.2. A corresponding model for the Josephson phase μ is realized by having the negative gravitational force in the π part (right hand side). The ground state in the π part is a chain of pendula standing up. Thus, at the $0-\pi$ boundary μ changes continuously from 0 to π on the scale of λ_J . The bending of the phase around the discontinuity point results in the appearance of a local magnetic field $\propto d\mu/dx$. As supercurrents $\pm \sin[\mu(x)]$ circulate around the boundary, one deals with a pinned Josephson vortex. In the case of a very long $0-\pi$ Josephson junction ($L \gg \lambda_J$), the magnetic flux due to the pinned Josephson vortex is equal to $\Phi = \pm\Phi_0/2$ [GKK02]. If the $0-\pi$ Josephson junction length $L \lesssim \lambda_J$, the semifluxon does not fully fit into the junction⁴ and the flux $|\Phi| < \Phi_0/2$. Semifluxons were observed experimentally [HAS⁺03; KTA⁺05] and have been under extensive experimental and theoretical investigation during the last decade [KTR⁺96; KMS97; KTM99; KCK00; Ste02; HAS⁺03; GKK03; SvGV⁺03; ZG04; GSG⁺04; GKK04; GSKK04; NSAN06; BGS⁺07].

To derive an analytic expression for the shape of a semifluxon, we start from the static version of Eq. (2.4) in the Hamiltonian case, *i.e.*, without perturbations. We consider an infinitely long $0-\pi$ junction with a phase

⁴One has to distinguish carefully between *fractional* φ -vortices and the case where the semifluxon does not fully fit into the junction, thus, its *fraction* of flux is below $\Phi_0/2$. In the first case, the topological charge φ is arbitrary, while in the second case $\varphi = \pm\pi$, but $|\Phi| < \Phi_0/2$. The topological charge φ of a system is defined as the differences between $\mu(x)$ at $x = -\infty$ and $x = +\infty$.

jump at $x = 0$:

$$\mu_{xx}^{\mp} = \pm \sin \mu. \quad (2.5)$$

$\mu^{-}(x)$ refers to the left half of the junction, $\mu^{+}(x)$ to the right half. Taking into account the boundary conditions

$$\mu(-\infty) = 0, \mu(+\infty) = \pi, \mu_x(\pm\infty) = 0 \quad (2.6)$$

the solution of Eq. (2.5) is found as [BKS78; XMT95; GKK02]

$$\mu(x) = \pm \begin{cases} 4 \arctan [(\sqrt{2} - 1)e^{+x}] & : x < 0 \\ \pi - 4 \arctan [(\sqrt{2} - 1)e^{-x}] & : x > 0. \end{cases} \quad (2.7)$$

The polarity of the semifluxon is only defined by the sign of μ , not by θ , compare [GKK02]. A simple presentation for the polarity of semifluxons is given by the characters \uparrow (+) and \downarrow (-). The magnetic field of a semifluxon inside the $0-\pi$ junction is derived as

$$\mu_x(x) = \pm \frac{2}{\cosh[|x| - \ln(\sqrt{2} - 1)]}. \quad (2.8)$$

Again, the different signs account for the positive semifluxon (+) and the antisemifluxon (-).

In Fig. 2.3 (a) the shape of a semifluxon is plotted in terms of phase $\varphi(x)$ (red, dashed line) and $\mu(x)$ (black, solid line). The Josephson phase of a fluxon is also shown (black, dotted line). In Fig. 2.3 (b) the magnetic field distribution for both, fluxon and semifluxon, and in Fig. 2.3 (c) the supercurrent distributions of both are shown. In contrast to the fluxon, the magnetic field profile of the semifluxon shows a sharp cusp-like maximum. Its tails are the tails of the fluxon solution. The magnetic field in the center of the semifluxon $\mu_x(0) = \sqrt{2}$; in comparison, the field in the center of a fluxon is equal to 2. The supercurrent profile of the semifluxon, again, is sharper than the one of the fluxon. The spatial distributions of the supercurrents in both cases, fluxon and semifluxon, are on the scale of $\sim \lambda_J$.

To understand the spontaneous creation of a semifluxon (antisemifluxon) as the ground state(s) of a $0-\pi$ junction, it is helpful to write down the energy of the system. In analogy to the sine-Gordon equation the energy of an infinitely long $0-\pi$ junction is written in general as

$$U = \int_{-\infty}^{+\infty} \frac{1}{2} \mu_x^2 + (1 - \cos \mu \cos \theta) dx. \quad (2.9)$$

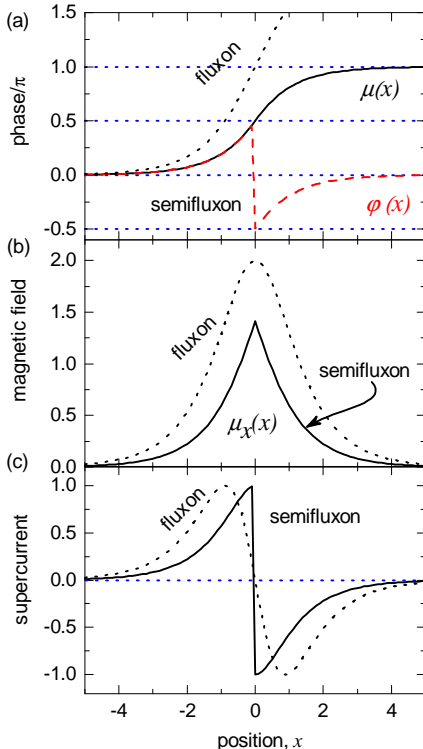


Figure 2.3: Comparison between the properties of fluxon and semifluxon. (a) Behavior of the total phase φ (red, dashed line) and the magnetic component μ (black, solid line) of the semifluxon. The Josephson phase of a fluxon is plotted as a black, dotted line. The magnetic field profile $\mu_x(x)$ of the fluxon and of the semifluxon are shown in (b) and the profile of the supercurrents for both is shown in (c). Modified from [GKK02].

The energy of a semifluxon, calculated [GKK03] by inserting Eq. (2.7) into Eq. (2.9), is given as

$$U = 16 \frac{\mathcal{G}^2}{1 + \mathcal{G}^2}, \quad (2.10)$$

with $\mathcal{G} = \sqrt{2} - 1$ (as it is true for the semifluxon)⁵, such that $U = 8 - 4\sqrt{2} = 2.343$. In contrast to this, the energy of the $\mu = 0$ flat phase state in a long junction is $\sim L$, *i.e.*, it linearly increases with length. For infinitely long junctions the energy of the flat phase diverges. Thus, the spontaneous creation of semifluxons is energetically favorable for (infinitely) long Josephson junctions.

Overall, the main differences between fluxons and semifluxons result from their totally different nature: Whereas a fluxon (antifluxon) represents an solitary *excitation* of a Josephson junction, the semifluxon

⁵Actually, expression (2.10) is valid for both fluxons and semifluxons. If we take $\mathcal{G} = 1$, this results in $U = 8$, the rest energy of a fluxon.

and its antisemifluxon represent the *degenerate ground states* of a $0-\pi$ junction. The fluxon can (more or less) freely move inside the junction. A semifluxon is pinned at the discontinuity point; even applying bias current might only deform it or change its polarity, but never liberates the semifluxon.

2.3 Static properties of $0-\pi$ junctions: a fingerprint of the semifluxon

What is happening if a bias current is applied to a $0-\pi$ junction? First, we consider an infinitely long Josephson junction in overlap geometry [GKK03]. The bias current exerts a driving force (Lorentz force) onto the semifluxon. As the semifluxon is pinned at the $0-\pi$ boundary, it is deformed by the bias current. Above a critical value $\gamma_c = 2/\pi \sim 0.63$ (depinning current) the semifluxon spontaneously flips and changes its polarity. To conserve the topological charge of the system, during the flipping process a fluxon is emitted. The fluxon is accelerated by the Lorentz force, producing a voltage drop. The antisemifluxon is again pinned, but exposed to the same driving force $\gamma > \gamma_c$. Analogously, it splits into a antifluxon and a semifluxon and the antifluxon leaves. Now, the system has returned to its initial state. If still $\gamma > \gamma_c$ the hole process is repeated; the semifluxon changes its polarity and emits fluxons and antifluxons.

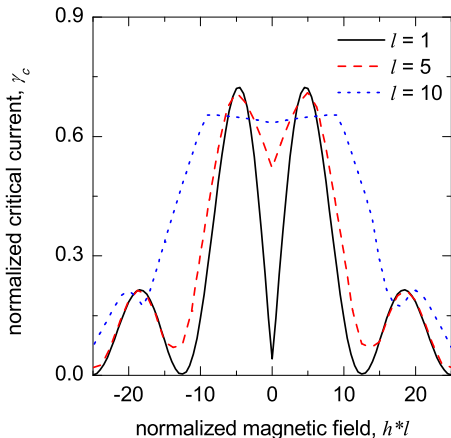


Figure 2.4: Numerically calculated $I_c(H)$ pattern of $0-\pi$ junctions of different lengths (black solid line: $l = 1$, red dashed line: $l = 5$, blue dotted line: $l = 10$). All junctions are symmetric, $\delta = 1$.

For $0-\pi$ junctions of finite length, we find a reduced⁶ value of γ_c . To gain deeper insights, we consider a $0-\pi$ junction in the opposite (short) limit ($L \ll \lambda_J$) [GGS⁺05]. As already mentioned, for $L \lesssim \lambda_J$ the semifluxon does not fully fit into the junction. The phase profile Eq. (2.7) is not a solution of the sine-Gordon equation (2.5), as the boundary conditions $\mu_x(\pm L/2) = 0$ are not fulfilled. However, a solution can be found by considering an infinite chain of antiferromagnetically ordered semifluxons: one has to place (mirror) semifluxons of opposite polarity at $x = -L$ and $x = +L$ (and so on). These semifluxons can hop from one $0-\pi$ boundary to the next, provided that they are not far apart. This process requires a relatively small driving force. Thus, by applying a (relatively small) bias current, the semifluxons switch positions by exchanging virtual fluxons. As flux is transferred through the boundaries, this results in a finite voltage drop. In general, depending on the junction length, by applying a bias current between $0 < \gamma_c < 0.63$ one drives a $0-\pi$ junction to a finite voltage state: The (anti)semifluxon changes its polarity and emits virtual (anti)fluxons.

In Fig. 2.4 numerically calculated magnetic field dependencies of the critical current of three $0-\pi$ junctions are shown. The $I_c(H)$ pattern were calculated using the ACTIVLLJJA.EXE software [act09]. The junctions are of different normalized lengths, ranging from the short to the long junction limit. All junctions are symmetric, $\delta = 1$. δ is the so-called *asymmetry factor*, defined as $\delta = j_c^\pi/j_c^0$. The main property of these $I_c(H)$ dependencies is a central dip around zero magnetic field $h = 0$, compare [Laz04]. In contrast to standard 0 Josephson junctions, see Sec. 1.3.2, there is no central maximum (provided that there is no parasitic flux trapped in the junction). The special shape of the $I_c(B)$ pattern with the central minimum around zero field is a characteristic feature of the $0-\pi$ boundary. In the short junction limit of a $0-\pi$ junction, the dip is very pronounced. The dip becomes shallower with increasing junction length l ; for junctions in the long limit it is rather a large plateau. The critical current values at zero field for different junction lengths vary between $\gamma_c^{l=0} = 0$ and $\gamma_c^{l=\infty} \sim 0.63$, see Fig. 2.4. It is easy to understand the different dip heights for different junction lengths: In the short junction limit at zero field, an infinite chain of antiferromagnetically ordered semifluxons/antifluxons is assumed to be a solution of the system. As the semifluxon chain is rather dense, switching processes occur at drastically lower bias currents in comparison to a single semifluxon in an

⁶For junctions of finite length L and width W , the critical current reduces to $I_c < \frac{2}{\pi}|j_c|LW$, with j_c being the critical current density of the 0 or π part.

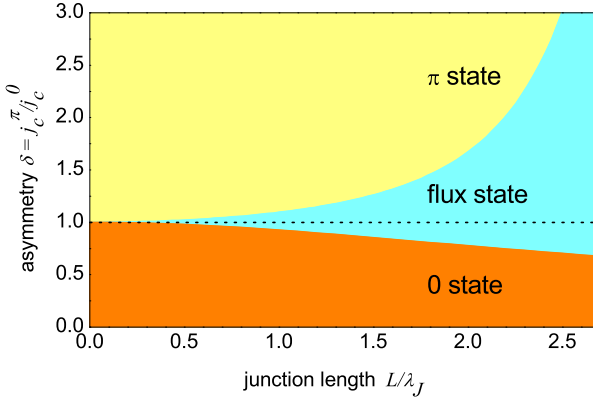


Figure 2.5: Ground state diagram of 0- π junctions. Depending on the junction length l and the asymmetry factor δ , the respective ground state solution is indicated: 0 state ($\mu = 0$, $\Phi = 0$), π state ($\mu = \pi$, $\Phi = 0$) or flux state. Only in the flux state $|\Phi| > 0$.

infinitely long junction. Thus, the depinning current (critical current) strongly depends on the junction length, it is lower the shorter is the junction.

In addition to the length, the precise shape of the $I_c(H)$ pattern of a 0- π junction crucially depends on several aspects. The main influence is due to the asymmetry between the 0 and π parts. An asymmetry between the critical current densities in both halves *e.g.* influences the height of the central minimum of the $I_c(B)$ pattern. Furthermore, the interplay between junction length and asymmetry factor determines whether the semifluxon or a flat-phase state are the ground state solution of the system. Ref. [BKS78] derives two transcendental equations which define the boundaries between different ground state solutions. A solution of the two equations is shown in Fig. 2.5. There, for different junction length and different asymmetries the respective ground state solution is indicated. 0 state and π state are flat phase solutions, having $\mu = 0$ and $\mu = \pi$ phase in both halves, respectively. These homogeneous states do not carry fractional flux. Only in the flux state region, a spontaneous semifluxon emerges. Note, that for short 0- π junctions the critical current densities in the 0 and π part must be rather equal, otherwise the semifluxon is not the ground state solution. Further aspects will be discussed in detail in Chaps. 5 and 6.

Chapter 3

Josephson junctions in the quantum regime

In this chapter the dynamics of the Josephson phase in different temperature regimes are reviewed. Another mechanical model for pointlike Josephson junctions is introduced: the *washboard potential*. According to this model a Josephson junction is described as a virtual particle moving in a tilted cosine potential. Three escape mechanisms of the particle out of the potential well are discussed: thermal activation, macroscopic quantum tunneling and resonant activation. Different damping regimes are discussed. At the end of this chapter, we study the consequences of a finite (long) junction length and of discontinuity points on the quantum properties.

3.1 The washboard potential

The phase dynamics of pointlike Josephson junctions were extensively studied in the literature [Lik86]. A junction can be described by the resistively and capacitively shunted junction (RSCJ) model, see Subsec. 1.3.1. The same equations of motion govern the dynamics of a point-like particle of mass m moving along the generalized coordinate φ in a so-called wash-board potential

$$U(\varphi) = E_J(1 - \cos \varphi - \gamma\varphi). \quad (3.1)$$

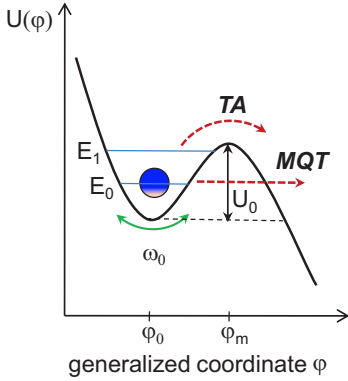


Figure 3.1: Virtual particle of mass m in a (tilted cosine) washboard potential $U(\varphi)$. ω_0 is the small amplitude oscillation frequency (eigenfrequency), U_0 the barrier height. φ_0 corresponds to the minimum, φ_m to the maximum of the potential. The energy levels in the well are indicated, likewise two escape mechanisms (TA: thermal activation, MQT: macroscopic quantum tunneling).

Here, γ is the normalized bias current, $E_J = I_c \Phi_0 / 2\pi$ is the Josephson coupling energy. At $\gamma = 0$ the particle is trapped in one of the local minima of the cosine potential and $V = \dot{\varphi} \Phi_0 / 2\pi = 0$. In the zero voltage state, the particle may perform small amplitude oscillations around the bottom of the well with the eigenfrequency

$$\omega_0(\gamma) = \omega_P (1 - \gamma^2)^{1/4} \quad (3.2)$$

with $\omega_P = (2\pi I_c / \Phi_0 C)^{1/2}$ being the Josephson plasma frequency. Again, I_c is the critical current of the junction, C its capacitance. If $0 < \gamma < 1$, the potential will be tilted but has still metastable minima, see Fig. 3.1. When $|\gamma| \rightarrow 1$ the minima disappear (the energy barrier vanishes), the particle can move down the potential. For $\gamma > 1$, always $\dot{\varphi} > 0$, the particle slides down the washboard potential with non-zero average velocity (finite voltage state). If thermal noise is neglected, the particle *only* starts moving if $\gamma \geq 1$. The respective potential barrier height U_0 depends on the bias current and is calculated from the potential difference $U(\varphi_m) - U(\varphi_0)$. φ_m is the position of the local maximum, φ_0 is the minimum position of the well. Thus, the potential barrier height is given by

$$U_0 = 2E_J \left[\sqrt{1 - \gamma^2} - \gamma \arccos \gamma \right] \quad (3.3)$$

$$\cong E_J \frac{4\sqrt{2}}{3} (1 - \gamma)^{3/2} \text{ for } 1 - \gamma \ll 1. \quad (3.4)$$

In analogy to the pendulum model, one distinguishes between the un-

derdamped and overdamped regime. In the underdamped regime the particle continues sliding down the potential wells if γ becomes < 1 . To retrap the particle in one well, it is necessary to reduce the potential gradient substantially by reducing the bias current. If the bias current reaches the retrapping current, see Sec. 1.3.1, the particle stops. In the overdamped limit, the particle is retrapped in one well, as soon as $\gamma < 1$.

3.2 Escape mechanisms of the Josephson phase in point junctions

3.2.1 Thermal activation

In nature, there is a variety of processes in which a system performs a transition between two distinct states by overcoming a potential barrier. Often, overcoming the potential barrier is due to thermal activation processes. Pioneering research in this field was already done a long time ago [Arr89; Kra40]. A rather recent review is given in [HTB90]. The authors developed a theory (TST = *transition state theory*) to describe thermally activated transitions between metastable states. The system of interest is described as a particle of an effective mass M , moving along a generalized coordinate q . The particle is subjected to an external potential $U(q)$ with a metastable minimum, compare Fig. 3.1. The height of the potential is given by U_0 . ω_0 is the small oscillation frequency (attempt frequency). As $\omega_0^2 = M^{-1}U''(q_0)$, the small oscillation frequency is determined by the curvature in the minimum of the potential well¹. Here, $U'' = \partial^2 U / \partial q^2$. The unstable barrier frequency ω_b is determined by the curvature of the potential barrier and given as

$$\omega_b^2 = \frac{-U''(q_m)}{M}. \quad (3.5)$$

The escape of a particle out of the well is described by a Langevin equation

$$M\ddot{q}(t) + M\zeta\dot{q}(t) + U'(q) = \xi(t), \quad (3.6)$$

ζ is the friction parameter, $\xi(t)$ is a stochastic force due to noise which is associated with a heat reservoir of temperature T .

¹We discussed one example of such a process in the last section: A short Josephson junction can be described as a particle in a washboard potential. The transition between two states is the transition from the zero-voltage to the finite-voltage state by applying a bias current.

In the *classical regime* (at sufficiently high temperatures), the particle is thermally activated (TA = thermal activation) over the potential barrier. The escape probability of the particle is discussed in terms of

$$\tau \equiv \Gamma^{-1}. \quad (3.7)$$

τ is the lifetime, Γ is the escape rate.

The probability of such a process follows the Boltzmann distribution and thus strongly depends on temperature. We consider the case of weak metastability, *i.e.*, U_0 is larger than the thermal energy $U_0 \gg k_B T$ and $U_0 \gg \hbar\omega_0$. Under the conditions, that (1st) there is a thermal equilibrium in the system and (2nd) the particle never returns to the well, the thermal escape rate Γ_{th} is given by

$$\Gamma_{\text{th}} = a_{\text{TST}} \frac{\omega_0}{2\pi} \exp\left(-\frac{U_0}{k_B T}\right), \text{ with } a_{\text{TST}} = 1. \quad (3.8)$$

Eq. (3.8) reflects the fact, that only particles whose energy is higher than the potential barrier U_0 can overcome the barrier. The escape rate depends on the attempt frequency ω_0 , the temperature of the environment *and* the dissipation in the system: The prefactor a is a friction dependent damping parameter. Escape rates which are calculated in the framework of the transition state theory, a_{TST} , are extremal. Usually, taking damping into consideration, the escape rates are lower in comparison to TST values, thus $a < 1$.

One has to distinguish between the low, moderate and high damping regime. All cases have been studied theoretically and experimentally. In the case of low damping [BHL83; RGP⁺98] the particle is weakly coupled to its environment and the time for thermalization is long compared to other processes in the system. Thus, there might be a non-equilibrium occupation of the states within the potential well. The highest states in energy ($U_0 - E \leq k_B T$) might be depleted. This results in a lowered escape rate with

$$a_{\text{LD}} = \frac{\gamma P \omega_0}{k_B T 2\pi}, \quad (3.9)$$

P depends on the potential under consideration, *e.g.*, for a cubic potential $P = 36U_0/5\omega_0$. In the case of moderate to high damping [VGJ⁺96], the particle might cross the barrier several times before it finally escapes from the well. Thus,

$$a_{\text{HD}} = \sqrt{1 + \left(\frac{\gamma}{2\omega_b}\right)^2} - \frac{\gamma}{2\omega_b}. \quad (3.10)$$

Last, the damping factor in the intermediate damping regime is given [BHL83] as

$$a_{\text{ID}} = \frac{4}{(\sqrt{1 + Qk_B T/1.8U_0} + 1)^2}, \quad (3.11)$$

$Q = \omega_b/\gamma$ is the quality factor. In the high as well as in the low damping regime the prefactor a deviates significantly from unity.

Transferring these results to the thermal escape of the Josephson phase of a small junction, the transition between two states is the transition from the superconducting zero-voltage state to a finite-voltage state. Here, the particle has a mass of $M = C(\Phi_0/2\pi)^2$. The potential is given by the washboard potential and the height was calculated according to Eq. (3.4). As thermal activation is only relevant for currents close to the critical current, U_0 is approximated by $U_0(1 - \gamma \ll 1)$ in Eq. (3.4). $\omega_0 = \omega_b$ is valid in case of the washboard potential.

Experimental determination of the escape rate of a Josephson junction

We experimentally investigate the escape rate of the Josephson phase by measuring switching current statistics with a time-domain technique. This method was suggested by T. A. Fulton and L. N. Dunkelberger [FD74; MDC87]. The junction is prepared in zero voltage state. The bias current is ramped up starting from $I = 0$ at a time $t = 0$ at a constant rate $\dot{I} = dI/dt$. At the time t_{sw} , the junction switches to a finite voltage state. The depinning process is statistically distributed, due to the presence of thermal fluctuations. The switching current I_{sw} is calculated as $I_{\text{sw}} = \dot{I} \times t_{\text{sw}}$. The switching current probability distribution $P(I_{\text{sw}})$ is found by accumulating a large number ($\sim 10^4$) of I_{sw} measurements and generating a histogram. The histogram is created by dividing the experimentally found values of switching currents into M intervals I_i (bins) of size ΔI . The number of events in each bin is normalized by the number of total events in the histogram. Each of the bins is labeled by the current value I_i at the middle of its interval. The probability distribution is given [FD74] as

$$P(I_{\text{sw}}) = \left(\frac{dI}{dt}\right)^{-1} \Gamma(I_{\text{sw}}) \exp\left[-\int_0^{I_{\text{sw}}} P(I') dI'\right] \quad (3.12)$$

$$= \left(\frac{dI}{dt}\right)^{-1} \Gamma(I_{\text{sw}}) \exp\left[-\int_0^{I_{\text{sw}}} \left(\frac{dI}{dt}\right)^{-1} \Gamma(I') dI'\right]. \quad (3.13)$$

$P(I_{\text{sw}})$ only depends on the bias current ramp rate \dot{I} and the escape rate Γ . Thus, by inverting Eq. (3.13) the escape rate Γ can be determined. To compare the experimental data Γ_{exp} with theory, one usually introduces the effective *escape temperature* T_{esc}

$$\Gamma_{\text{exp}} = a \frac{\omega_0}{2\pi} \exp\left(-\frac{U_0}{k_B T_{\text{esc}}}\right). \quad (3.14)$$

If there is no extra noise (*e.g.* electronic noise, which couples from the environment into the junction), the escape temperature is equal or close to the (bath) temperature.

To determine the escape temperature for an experimentally obtained activation process, the individual escape rate Γ_i of each bin is calculated as

$$\Gamma_i = \frac{\dot{I}}{\Delta I} \ln\left(\frac{\sum_{n=i}^M P_n \Delta I}{\sum_{n=i+1}^M P_n \Delta I}\right). \quad (3.15)$$

P_n is the discretized probability distribution related to the respective bin. With Eqs. (3.8), (3.4) and (3.2) one obtains

$$\left(\ln \frac{2\pi\Gamma_i}{a\omega_0(I_i)}\right)^{2/3} = \left(\frac{4\sqrt{2}E_J}{3k_B T_{\text{esc}}}\right)^{2/3} \frac{1}{I_{c,0}} (I_{c,0} - I_i). \quad (3.16)$$

$I_{c,0}$ is the fluctuationless critical current². T_{esc} and $I_{c,0}$ are not known, likewise ω_0 as it depends on the critical current. As Eq. (3.16) depends linearly on I , the unknown parameters can be determined with a recursive iteration process using a linear fitting routine: The maximum value of the switching current distribution $\langle I_{\text{sw}} \rangle$ is used as the first estimate of $I_{c,0}$. Then, ω_0 is calculated. With these values the left hand side of Eq. (3.16) is estimated; then a plot of the respective data is fitted linearly according to the right hand side of Eq. (3.16). From the fit new values for $I_{c,0}$ and ω_0 are obtained. As a first try $a = a_{\text{TST}}$ is chosen. Later, damping is considered to find the best agreement between experimental data and theoretical prediction. The statistical weights of Γ_i are considered, respectively. This process converges rather quickly [WLC⁺03]. Thus, one can calculate an effective temperature T_{esc} and $I_{c,0}$ for an experimentally obtained activation process³. The only parameters which

²Strictly speaking, $I_{c,0}$ is identical to the critical current I_c which was introduced in the dc-Josephson relation, see Eq. (1.3).

³An easy and detailed description of the - nowadays - standard data analysis can be found in [Wal01; WLC⁺03; Gab07]

are supplied to the self-consistent determination of T_{esc} and $I_{c,0}$ are the ramp rate \dot{I} and the capacitance C of the junction. Both are well-defined in experiment.

Furthermore, the standard deviation σ of $P(I_{\text{sw}})$ is often evaluated in experiment. According to [FD74; JGH⁺81; Gar95] the standard deviation scales as $\sigma \sim I_c^{1/3}$. To compare junctions with different critical currents, $\sigma^* = \sigma/I_c^{1/3}$ can be plotted in *reduced units*. As $\sigma \sim T^{2/3}$, the histogram width becomes more narrow when the temperature is decreased, as the thermal fluctuations decline. In the thermal regime, the standard deviation decreases with temperature.

3.2.2 Macroscopic quantum tunneling

The thermal activation of a particle out of the potential well is exponentially suppressed as the temperature of the bath is decreased, compare Eq. (3.8). In the limit of low damping and if the temperature is sufficiently low (*quantum regime*), a non-vanishing probability can be observed that the particle *macroscopically tunnels* through the barrier, provided that the barrier is small enough. This tunneling is *classically* forbidden, it is a typical feature of quantum mechanics. Thus, macroscopic quantum tunneling⁴ was regarded as a test if quantum mechanics is valid for *macroscopic* variables [Leg80; CL83]. Different Josephson systems were successfully used to prove this hypothesis experimentally, *e.g.*, the escape of the Josephson phase of small SIS junctions [JGH⁺81; DMC85; MDC87] and large area junctions [WLC⁺03], a superconducting ring interrupted by a Josephson junction [PLC⁺81], the escape of a Josephson vortex from a pinning potential [WLL⁺03; WLC⁺03] and many others [Sca69; CL83; BLT⁺05]. The discussion on the quantum properties of Josephson junctions has gained new interest as their possible application in solid state quantum information processing was suggested [MOL⁺99; IGF⁺99; MSS01].

⁴An important differentiation was made by [CL83]: “The phenomenon we shall be considering [as macroscopic quantum tunneling] is the macroscopic analog of the tunneling of an alpha particle out of a nucleus [...]. It is not like the Josephson effect in superconductors [...], which involve the system tunneling coherently, between two or more degenerate or nearly degenerate potential minima. From our point of view the crucial difference is that in the former type of phenomenon the phase relationship between the amplitudes for being on different sides of the barrier(s) can be neglected, since once outside the barrier the system never comes back and interferes with itself; for the latter type of phenomenon, on the contrary, it is crucial to take it into account.”

In this subsection we concentrate on the theoretical description of macroscopic quantum tunneling (MQT) of the Josephson phase of pointlike junctions and the experimental observation. To study macroscopic quantum tunneling of the phase similar switching current experiments are performed as described in the last subsection. With the time-of-flight technique histograms of switching currents are recorded. In contrast to thermal activation, the probability $P(I_{\text{sw}})$ due to quantum tunneling does not depend on temperature. If damping is neglected, the shape of the histograms is not influenced by temperatures. The width σ of $P(I_{\text{sw}})$ does not decrease with temperature, but stays constant. Thus, in experiment, the crossover between thermal activation and macroscopic quantum tunneling is observed if the standard deviation σ saturates.

Theoretically, macroscopic quantum tunneling can be described in the framework of the semiclassical *WKB* approximation (named after G. Wentzel, H. A. Kramers and L. Brillouin). If the system is initially localized in a metastable potential well and is isolated, the escape rate due to quantum tunneling is calculated [CL83] using a standard procedure as

$$\Gamma_{\text{qu}} = A_0 \exp(-B_0/\hbar) \quad (3.17)$$

with

$$A_0 = C_0 \omega_0 (B_0/2\pi\hbar)^{1/2}, \quad B_0 = 2 \int_0^{\varphi_m - \varphi_0} (MU(q))^{1/2} dq. \quad (3.18)$$

ω_0 is again the small oscillation frequency, M is the mass of the particle, $\varphi_{m,0}$ are the extremal points of the potential $U(q)$, compare Fig. 3.1. A_0 and B_0 are standard WKB expressions, C_0 takes into account the shape of the potential. A particular case is the *quadratic-plus-cubic* potential which might describe most systems of interest. Here [Leg84],

$$B_0 = \frac{36U_0}{5\omega_0}, \quad C_0 = (60)^{1/2}. \quad (3.19)$$

In nature, most systems show a complex interaction with their environments. In [CL83; Leg84] the authors study the influence of dissipation on the escape rate of macroscopic quantum tunneling (*Caldeira-Leggett theory*). As in the thermal regime, dissipation generally suppresses the escape rate. The authors derive a general expression for Γ_{qu} in the strong and low damping regime and apply their results to several potentials. Important in the framework of this thesis is the derivation of Γ_{qu}

of the Josephson phase of a short junction at zero temperature including linear (mainly) frequency-independent dissipation. In the quantum regime, $\hbar\omega_0 \gg k_B T$. The escape rate is given to lowest order in $1/Q$ by

$$\Gamma_{\text{qu}} = \frac{a_q \omega_0}{2\pi} \exp\left(-\frac{7.2U_0}{\hbar\omega_0} \left(1 + \frac{0.87}{Q}\right)\right) \quad (3.20)$$

with $a_q \sim (120\pi[7.2U_0/\hbar\omega_0])^{1/2}$. The escape temperature in the quantum regime can be estimated [CL83] as

$$T_{\text{esc}} = \frac{\hbar\omega_0/k_B}{7.2(1 + 0.87/Q)(1 - p_q)} \quad (3.21)$$

with $p_q \sim (\hbar\omega_P/7.2U_0) \ln a_q/(1 + 0.87/Q)$.

We introduce the *crossover temperature* T^* , at which the system changes from thermal (temperature dependent) to quantum (temperature independent) behavior. Approximately, this is the temperature, at which quantum fluctuations dominate thermal fluctuations. As already mentioned, this crossover is observed in experiment by the saturation of the standard deviation σ . In the limit $Q \gg 1$, T^* is approximated as

$$T^* \sim \frac{\hbar\omega_0}{2\pi k_B}. \quad (3.22)$$

A precise calculation of T^* is *e.g.* given in [GW84; HTB90]; there, damping is taken into account.

3.2.3 Resonant activation

A third escape mechanism of the particle out of the potential well is the *resonant activation* (RA). Here, the particle is resonantly excited by an external ac force at a frequency close to its eigenfrequency (Eq. (3.2)). We concentrate on the resonant activation of the Josephson phase of a pointlike junction by applying microwaves as an external ac force. An interpretation is given in the quantum and in the thermal regime.

In the classical picture of a Josephson junction being a particle in the washboard potential, resonant activation is interpreted as follows: In the ground state, the particle is trapped in the well and performs small oscillations with its eigenfrequency ω_0 . When an external force (*e.g.* microwaves) is applied periodically to the particle, energy is transferred. A maximum of energy is transferred, if the external frequency is close to the eigenfrequency of the particle. Then the particle may escape

out of the well [DMEC84]. At very low temperatures, in the limit of low damping, the particle picture has to be extended to take quantum effects into account. Besides the saturation of the standard deviation, another signature of the quantum regime is that there are *discrete energy levels* within the potential well. In Fig. 3.1 the ground state E_0 and the first excited state E_1 in the potential well are indicated. Both levels do not overlap. In contrast to a harmonic oscillator, the energy level spacing is not equidistant; the level spacing decreases with increasing energy. This is due to the non-harmonic nature of the washboard potential. It is only because of this anharmonicity, that excited states can be addressed individually. As the level spacing is not equidistant, a certain microwave energy $\hbar\omega_{\text{rf}}$ (rf= radio frequency) only interacts with certain transitions, provided that the width of the microwaves ω_{rf} is narrow enough. First, the particle is in the ground state. If photons (microwaves) are applied and the photon energy is, *e.g.*, equal to the energy level spacing between ground and first excited state,

$$\hbar\omega_{\text{rf}} = E_1 - E_0, \quad (3.23)$$

a transition between the states takes place by absorption of the photon. As tunneling from the excited states is enhanced exponentially (the height of the barrier is reduced by the energy of the excited state), the result is the same as in the classical picture: The particle may escape out of the well and the junction may switch from the zero-voltage to the resistive state. In contrast to thermal escape and macroscopic quantum tunneling, by applying microwaves the switching current statistics is bistable, compare Fig. 6.8.

In experiment, resonant activation is studied with the time-domain technique, but in presence of applied microwaves. Switching current histograms are recorded. Here, the histograms reveal a double-peak structure, see Fig. 6.8. This behavior is, *e.g.*, used to determine the transitions between several energy levels experimentally. As the bias current tilts the washboard potential, the respective energy spacing directly depends on the applied bias current. The resonance condition between microwave frequency and eigenfrequency of the junction is met in experiment, by varying the energy level spacing with bias current while keeping the microwave frequency fixed. By tracking the current position of the resonant peak for different frequencies of the external drive, the transitions between several energy levels (*e.g.* $E_0 \rightarrow E_1$, $E_1 \rightarrow E_2$, ...) of the samples are obtained. These features have been observed in experiment [MDC85] and have been interpreted as the population of several quantum levels in

the system. In the classical picture, one does not study different energy levels, instead the escape of the particle out of the well is examined. If external driving frequencies equal to $\omega_{\text{rf}} = n * \omega_0$, $n = 1/2, 1/3, \dots, 2, 3, 4 \dots$ are chosen, also a two-peak structure in the switching current histograms is observed. These branches are identified as *harmonic* pumping ($\sim \omega_0$), *superharmonic* pumping ($\sim n \times \omega_0$, n being an integer number) and *subharmonic* pumping ($\sim \frac{\omega_0}{n}$). The transitions are interpreted (quantum mechanically) as multiphoton mediated processes. They have been observed experimentally in [WDLU03; GJCC⁺04].

Whether a Josephson junction is described more accurately by a quantum system having several distinct energy levels, or by an anharmonic oscillator, depends on the respective damping/temperature regimes and the mass of the particle $m \sim C$. The effective damping resistance R as well as the capacitance C give rise to a energy level broadening [Lis08]

$$E \sim \frac{1}{RC}. \quad (3.24)$$

In the limit of low damping, the energy levels are usually narrow enough not to overlap. Increasing the temperature results in a broadening of the levels until they merge into a continuum. However, indications for the quantization of the energy levels at temperatures even above T^* were found by [SPRR97].

3.3 Consequences of finite length and phase discontinuity points on the escape mechanisms

In the framework of this thesis, phase escape mechanisms of junctions with a finite length (intermediate to long limit) and of junctions with a discontinuity point (phase shift of π) are considered. In contrast to pointlike junctions, these additional features lead to modifications of the phase escape mechanisms discussed so far. Studies regarding escape mechanisms in long junctions or junctions with trapped fractional flux deal with very special aspects of the problem. Only a few topics have been discussed in detail, there are still a lot of open questions. In this section, we briefly summarize some important findings which are relevant for this thesis. For further information the respective references should be considered.

Long Josephson junctions

If one considers phase escape processes in a *long* Josephson junction, the spatial dependence of the Josephson phase $\mu(x)$ has to be taken into account. A long junction is not described by a single particle moving in a washboard potential, but rather by a string. This string can overcome the barrier as a rigid string (lifted as a whole over the potential barrier): the phase difference is the same along the junction and does not depend on the spatial coordinate. In this case, the activation energy increases with increasing junction length. An increasing length leads to an enhanced critical current, thus to an enhanced coupling energy E_J and enhanced barrier U_0 . As a second activation mechanism in long junctions, the phase of the string can also bend, so that first a part of the string passes over the barrier and then it pulls the rest [CTC⁺96]. In this case the activation is related to the creation of a fluxon or antifluxon⁵. As the energy for the creation of a fluxon or antifluxon does not depend on the junction length (if $L \gg \lambda_J$), the activation energy does *not* depend on the junction length. In [CTC⁺96] it is shown, that usually for $0 < l < \pi$ the activation energy linearly increases with length, as in this regime the string passes the barrier as a whole. For $\pi < l < \infty$ the activation energy saturates and is equal to the creation energy of a fluxon or antifluxon $U_0/E_0 = 8$. There are several theoretical works on the nucleation of fluxons or antifluxons in infinitely long junctions, both in the thermal as well as in the quantum regime [HE84; NH86; SG90]. Activation processes for finite linear and annular long Josephson junctions were studied theoretically in [CTC⁺96; FWK⁺03; GK06]. Experiments are very rare, in [CTC⁺96] the authors use overlap as well as inline geometry junctions in the absence and presence of applied magnetic field. These measurements were done in the thermal regime. The authors studied the change of the activation energy as a function of magnetic field and junction length. In [CTC⁺97] it was shown experimentally, that in the presence of magnetic field — at least in the thermal regime — the internal dynamics in long junctions significantly influence the escape temperature.

Further studies [KI96; WLL⁺03; GJC04; Kem06] on long (annular) junctions examined the behavior of a Josephson vortex which is pinned by an applied magnetic field or an inhomogeneity: MQT of a fluxon was described [KI96] and already observed [WLL⁺03]. Both, spectroscopy

⁵This is true for linear junctions. As discussed in Subsec. 1.4.2, in annular junctions a fluxon+antifluxon pair is created.

measurements as well as escape rate measurements in the thermal and quantum regime revealed that this system behaves equivalently to point-like junctions. The problem can be mapped to an effective 1-dimensional potential.

Phase discontinuity points

In general, the presence of a phase shift (pinned fractional flux) changes the effective barrier height of the potential well in contrast to 0 Josephson junctions. Up to now there are only rare theoretical and experimental studies regarding fractional vortices as quantum objects. For symmetric **short** [GVS⁺09] $0-\pi$ junctions ($L \leq \lambda_J$) containing a fractional vortex, the theory of thermal activation and MQT was developed recently. As described in Sec. 2, a $0-\pi$ junction has a degenerate ground state. If the energy barrier — which separates the ground states — is small enough, the junction switches to the resistive state by emitting a fluxon. The excitation over the barrier might be due to thermal activation or macroscopic quantum tunneling. By introducing a collective coordinate Q , the authors [GVS⁺09] mapped the problem to a single particle in a double well potential. The estimations were done for an undriven, dissipationless system. The crossover temperature of a short $0-\pi$ junction was determined as

$$T^* \sim \frac{\hbar l \omega_0}{8\sqrt{3}k_B}. \quad (3.25)$$

As a criterion for quantum behavior they used

$$\frac{8\sqrt{3}\hbar\omega_0}{\pi^2 E_J \lambda_J l^2} \geq 0.1. \quad (3.26)$$

The authors estimated, that using short $0-\pi$ junctions with standard SIS parameters⁶ the quantum regime is hard to reach. Very low temperatures ($T \leq 30$ mK) should be used. As the junctions are rather short, it is very elaborate to read out the state of the fractional flux. The largest problem in experiment might be that the behavior of MQT is very sensitive to asymmetries between the 0 and π parts [GVS⁺09]. Another option is to use SIFS junctions for these experiments. Their critical current densities are orders of magnitude lower than for SIS junctions,

⁶For means of comparison: For standard Hypres-Nb/Al-Al₂O₃/Nb-technology junctions with $j_c = 100$ A/cm² quantum effects start to play a role as $l \leq 0.18$ ($L \leq 10$ μ m) and $T \leq T^* = 30$ mK.

thus their properties should lead to more manageable experimental parameters, *e.g.*, the junction length should be large in comparison to SIS junctions. On the other hand, a lower critical density leads to even lower crossover temperatures, which complicates the observation of the quantum regime. Likewise, it is difficult to fabricate highly symmetric $0-\pi$ junctions. Up to now there has been no experimental prove of reaching the quantum level with short $0-\pi$ junctions.

For **infinitely long** junctions the effective potential for the escape of a fractional vortex and its eigenfrequency was estimated analytically and numerically [VSK⁺09]. This work considers an *arbitrary* phase shift κ ; the calculations were done in the presence of bias current close to the critical current. Again by mapping the problem to a particle in a metastable potential, the authors predicted the escape rates as a function of bias current and topological charge in the quantum and classical regime. It was shown that vortices with a larger topological charge escape easier. In general, the presence of fractional flux lowers the potential barrier in comparison to junctions without trapped flux. For typical experimental parameters of Hypres-SIS-samples a crossover temperature in the range of $T^* \sim 100$ mK was estimated. Thermal escape of fractional vortices in long junctions was recently observed in experiment [KGB⁺09b]. Annular and linear SIS junctions with tiny injectors were used to create fractional vortices, κ could be tuned electronically. The authors studied in detail the dependence of the effective barrier height on junction length and on topological charge. To reach the quantum regime with fractional vortices in long junctions is an on-going research topic in the Tübingen-group⁷.

The eigenfrequencies of fractional vortices in long junctions were already obtained in experiment [BGS⁺07]. Annular junctions with injectors were used for microwave spectroscopy in the thermal regime at $T = 4.2$ K. The authors examined the eigenfrequencies as a function of topological charge and bias current. They found an excellent agreement between experimental data and theoretical predictions.

⁷Actually, to reach the quantum regime with long junctions carrying fractional flux is tried with two different technologies. 1st: SIS-technology with tiny injectors. 2nd: SIFS junctions.

Chapter 4

Josephson junctions with a ferromagnetic barrier

The interplay between superconductivity and ferromagnetism was studied theoretically during many decades [Buz05]. In general, (singlet) superconductivity and ferromagnetism are contrary effects. The coexistence of both, superconductivity and ferromagnetism, was discussed for homogeneous systems as well as for spatially separated systems. Here, we consider heterostructures which consist of thin superconducting/ferromagnetic (SF) multilayers. This in turn leads to new and interesting phenomena: SF multilayers had been suggested for the realization of π and $0-\pi$ Josephson junctions. In the following chapter, we briefly review the most important theoretical and experimental results regarding SFS/SIFS Josephson junctions. Then, we present theoretical explanations of the π state and its microscopic origin. The diffusive and the clean limit are discussed. At the end of the chapter we present a sample preparation method, which was used to fabricate Nb/Al-Al₂O₃/Ni₆₀Cu₄₀/Nb SIFS junctions with $0-$, π and $0-\pi$ coupling. These junctions are used throughout this thesis for experimental studies.

4.1 Introduction: history and state of the art

In Sec. 2.1 a π Josephson junction was introduced as having a current phase relation of $I = I_c \sin \mu$ with $I_c < 0$. The first one to predict

Josephson junctions with a negative critical current was L. Bulaevskii in 1977 [BKS78; BKS77]. He considered Josephson junctions having a barrier with magnetic impurities. In this case the Cooper pair electrons can perform a spin flip (by scattering at the magnetic impurities), leading to an additional tunneling channel. If this channel overtakes direct tunneling, the supercurrent becomes negative. Although the theoretical studies are rather old, it has just been during the last few years that considerable results have been achieved regarding the experimental realization of ferromagnetic π and $0-\pi$ Josephson junctions¹.

The first unambiguous experimental realization of Josephson junctions in the π state was provided by V. V. Ryazanov *et al.* [ROR⁺01]. They showed for $\text{Cu}_{0.5}\text{Ni}_{0.5}$ SFS junctions a non-monotonic behavior of the critical current dependence on temperature, with a sharp cusplike minimum. This temperature-induced $0-\pi$ transition was only observed for junctions with some specific thicknesses of the F-layer. Comparable temperature-induced $0-\pi$ transitions were also observed by [SBLC03] and [FVHB⁺06]. The authors used diluted ferromagnetic NiCu alloys as well. In 2002 T. Kontos *et al.* [KAL⁺02] presented experimental data of a thickness-induced $0-\pi$ transition. At the same time, these authors presented the first SIFS Josephson junction. They used a standard Nb/Al- Al_2O_3 /Nb technology with an additional layer of PdNi. An advantage of SIFS Josephson junctions is that their resistance-area product $R \times A$ can be tuned over orders of magnitude by varying the thickness d_I of the insulating barrier. A high $R \times A$ product facilitates voltage readout and allows to observe dynamic behavior of the junction due to low damping. Thus, these junctions can be used not only as phase batteries but also as active switching elements in superconducting electronic circuits. By contrast, SFS junctions have a small $R \times A$ product and are always in the overdamped limit. In 2006, V. V. Ryazanov's group reported the first experimental observation [OBF⁺06] of a two-node thickness dependence of the critical current, thus they showed two subsequent $0-\pi$ transitions in SFS junctions. Further thickness induced $0-\pi$ transitions with weak ferromagnets were observed by [BTKP02; WKG⁺06]. In 2006 two publications appeared, using strong ferromagnets as the Josephson barrier. J. W. A. Robinson *et al.* [RPB⁺06] prepared Co, Ni and Py junctions in the clean limit. They were able to observe several oscillations of the critical current vs. ferromagnetic layer thickness. Especially

¹Actually, the experimental observation of a π state in Josephson junctions containing magnetic impurities (which is the original idea of L. Bulaevskii), was proven just very recently [VGG⁺06].

their Co junctions showed a good agreement between experiment and theory. F. Born *et al.* [BSH⁺06] reported on multiple $0-\pi$ transitions on SIF(Ni₃Al)S junctions in the clean limit. For these samples a thick magnetic dead layer was assumed to interpret the experimental data. Additionally, the resolution of the experimental data is rather poor, the determination of individual oscillations is not stringent. In 2009 A. A. Bannykh *et al.* [BPS⁺09] reported on the first temperature-induced $0-\pi$ transition using a strong ferromagnetic Ni interlayer.

In general [GKI04], the supercurrent through a Josephson junction can be written as

$$I(\varphi) = \sum_{n \geq 1} I_n \sin(n\varphi) + J_n \cos(n\varphi). \quad (4.1)$$

The evolution coefficients I_n , J_n take *e.g.* microscopic details of the barrier/weak link into account. The cos-terms (usually) vanish as they are not invariant via time reversal. Only in a few cases the current-phase-relation Eq. (4.1) reduces to the familiar sinusoidal dc-Josephson relation Eq. (1.3). Thus, the determination of the current-phase-relation and the determination of higher order terms is crucial for understanding. First measurements on the current-phase relation of SFS Josephson junctions [FHO⁺04] did not show plausible hints for the existence of higher order harmonics. In 2004, H. Sellier [SBLC04] examined the current-phase-relation near the temperature-driven $0-\pi$ transition. They found a non-vanishing supercurrent fraction at the point of the $0-\pi$ transition which they interpreted as a $\sin(2\varphi)$ component. Strikingly, this residual supercurrent showed half-integer Shapiro steps when applying high frequency excitations.

Following the idea of L. Bulaevskii [BKS77], the signatures of π Josephson junctions were also demonstrated by embedding π junctions into superconducting loops [ROVR01; GAB⁺03; BBA⁺04]. This leads to a spontaneous flux of half of the magnetic flux quantum, which manifests itself as a spontaneously circulating supercurrent. If one of the Josephson junctions in a SQUID is a π junction, the $I_c(B)$ dependence is shifted by half a period.

π Josephson junctions are intensively investigated, as they promise important advantages for Josephson junction based electronics [TGB97; TB98], *e.g.* they can be used in RSFQ logics to self bias the circuit and to reduce the number of bias resistors [OAM⁺06] and inductances [UK03]. In particular, they are suggested for Josephson junction based qubits [IGF⁺99; BGI01; YTTM05; YTM06]. Additionally, as π junctions are

now available with a high quality and different parameter options, there was a huge interest to produce $0-\pi$ junctions as a further developmental step of π junctions.

An intentionally made symmetric $0-\pi$ SIFS Josephson junction with two reference junctions was demonstrated recently by M. Weides *et al.* [WKK⁺06]. Before that, $0-\pi$ Josephson junctions were realized by utilizing d-wave superconductors [TK00; SAB⁺02; VH95; HAS⁺03] or were obtained by chance using SFS junctions [DRAK⁺05; FVHB⁺06]. The $0-\pi$ SIFS Josephson junction of M. Weides had a high characteristic voltage $V_c = I_c R$ making direct transport measurements possible. The samples could be driven to the underdamped regime by decreasing the temperature below 4.2 K. Tuning the temperature, the same absolute critical current densities in both parts of the $0-\pi$ junction were achieved. A $0-\pi$ SIFS junction is a promising system to study the physics of semifluxons. One can also use $0-\pi-0$ SIFS structures to design semifluxon molecule qubits [KI97; GVC⁺05]. No restrictions in topology, low damping and good reproducibility make the phase modulated SIFS Josephson junctions good candidates for future logic elements.

Thus, SIFS 0 , π and $0-\pi$ Josephson junction technology can already be used to fabricate more complex superconducting electronic devices combining the dynamics of fluxons and semifluxons, *e.g.*, using RSFQ readout for semifluxon bits/qubits or ballistic fluxon readout [GSKK04; HFS⁺07].

4.2 Theory of π junctions

4.2.1 Microscopic origin

To understand the origin² of the phase change of the order parameter in ferromagnetic Josephson junctions, we first discuss the simple case of a S/N (superconductor/normal metal) or S/F bilayer, see Fig. 4.1. When Cooper pair electrons enter the normal metal (coming from the superconductor), they are not eigenstates of the system, thus they are in an evanescent state and decay³ (so-called *proximity effect*). The characteristic length scale for this decay is the correlation decay length ξ_N . On the

²An extensive overview on S/F structures is given in [Buz05].

³The dependence of the decay on the spatial coordinate depends on the respective regime: clean and diffusive limit are discussed in detail below.

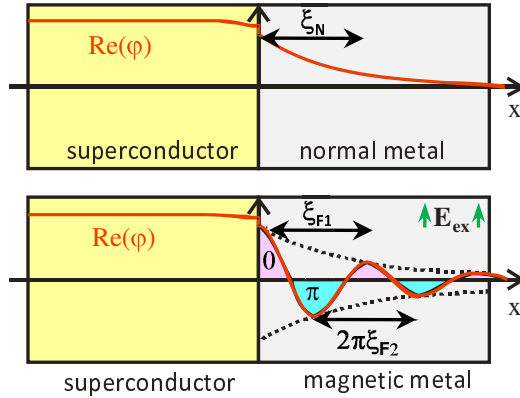


Figure 4.1: Spatial dependence of the superconducting order parameter φ (red, solid line) at the superconductor (yellow) /normal metal (white) and superconductor/ferromagnet boundary. The respective correlation decay lengths ξ_N (normal metal) and ξ_{F1} (ferromagnet) are indicated, as well as the correlation oscillation length $2\pi\xi_{F2}$. The direction of the exchange field E_{ex} is indicated by green arrows. Modified, from [Wei06].

other hand, the leakage of the Cooper pairs weakens the superconductivity near the interface. The superconducting order parameter inside the superconductor is reduced on a length scale of the Ginzburg-Landau coherence length ξ in the vicinity of the normal metal (*inverse proximity effect*)⁴. Due to the proximity effect, supercurrents can flow through metallic barriers, provided that the barrier is thin enough. In S/F structures, the situation is more complex. If Cooper pair electrons enter the ferromagnet, the amplitude of the superconducting wave function is suppressed due to the proximity effect, too. The respective correlation decay length is called ξ_{F1} . Additionally, the electrons experience the exchange field E_{ex} of the ferromagnet. The potential energy of the electrons is changed by the exchange energy $\pm E_{\text{ex}} = \mu_B B_{\text{ex}}$. The two signs account for the two spin directions. The electron with the energetically favorable spin (parallel to the exchange field) lowers its potential energy and — due to conservation of energy — increases its kinetic energy. The second electron of the Cooper pair (with the spin opposite to the exchange field) gains potential energy by lowering its kinetic energy. This results in a fi-

⁴This effect results in a decrease of the critical temperature T_c of thin superconducting films in contact with normal metal.

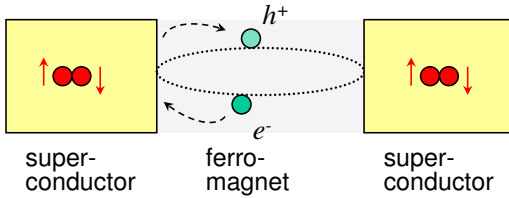


Figure 4.2: Schematic picture of Andreev reflection in a SFS sandwich. Both superconductors (yellow) contain Cooper pairs (red), in between the reflection of an electron into a hole is depicted.

nite center of mass momentum of the Cooper pair $2Q = 2E_{ex}/v_F$, where v_F is the Fermi energy in the ferromagnet⁵. By quantum mechanics, Q modifies the phase of the order parameter as $\theta_x = Qx$, which linearly increases with distance x from the S/F boundary. Since the original momentum of each electron can be positive or negative, the center of mass momentum can be positive or negative, and thus the phase of the order parameter can be positive or negative. Superimposing both possibilities, leads to an oscillating spatial variation of the superconducting wave function $\varphi \sim \cos(2Qx)$. The characteristic length scale of the oscillations is the correlation oscillation length $2\pi\xi_{F2}$. Taking both effects — the proximity effect and the influence of the exchange field — into account, the superconducting wave function penetrates into the ferromagnet in the form of damped oscillations [FF64; LO65], see Fig. 4.1.

To describe transport through S/F/S (S/N/S) interfaces, the *microscopic* theory of *Andreev reflection* can be used [And64; SBLC03]. An electron inside the ferromagnet (normal metal) which has an energy lower than the superconducting energy gap Δ cannot enter the superconductor. In Fig. 4.2 it is shown, how the electron is reflected (Andreev reflection) at the F/S (N/S) interface as a hole (and vice versa). A corresponding charge of $2e$ is transferred into the superconductor and forms a Cooper pair. This process leads to a supercurrent through the barrier. In the ferromagnet (in contrast to normal metal) the Andreev reflection depends on the spin splitting of the opposite spin bands, as the spin of the electrons/holes is reversed during reflection. As a result a Cooper pair

⁵This is related to the so-called *FFLO* state which was predicted long ago by A. I. Larkin and Yu. N. Ovchinnikov [LO65] and by P. Fulde and R. A. Ferrel [FF64] for superconducting ferromagnetic alloys. They predicted that pairing of Cooper pairs can still occur when the electron energies and momenta at the Fermi energy are not equal for the two spin directions. In this case the order parameter is spatially not homogeneous and contains nodes. At these nodes the phase changes by π .

with opposite spin directions appears in the superconductor.

After all, the phase shift of the superconducting order parameter in ferromagnetic π Josephson junctions is obvious. As the wave function is spatially oscillating inside the ferromagnetic barrier, the phase depends on the thickness d_F of the ferromagnetic barrier. If the thickness of the ferromagnetic barrier is smaller than half of the oscillation period, the wave function does not change sign. Thus we call this junctions 0 junctions, compare Chap. 2. If d_F is of the order of half the oscillation period, the superconducting wave function changes its sign, *i.e.*, shifts its phase by π while crossing the ferromagnet. S/F/S (S/I/F/S) structures show a non-monotonic dependence of the critical current on the barrier thickness⁶. The vanishing of I_c is due to the 0 to π transition – so-called *thickness-induced* 0- π transition. In this context it should be mentioned that the ratio between the correlation decay length ξ_{F1} and the correlation oscillation length $2\pi\xi_{F2}$ is crucial. If ξ_{F1} is large in comparison to $2\pi\xi_{F2}$, the superconducting wave function performs several oscillations before it is suppressed due to damping. In this case several phase shifts can be observed when the thickness of the ferromagnetic barrier is varied. If ξ_{F1} is much smaller than $2\pi\xi_{F2}$, it is not possible to observe the 0 to π transition by varying d_F . The ratio between both characteristic length scales in ferromagnets depends on the respective regime, as described below.

4.2.2 Diffusive vs. clean limit

Preparing ferromagnetic Josephson junctions raises the question, which ferromagnet to use. One can choose between weak and strong ferromagnets, between alloys and pure materials. In all cases the characteristic length of the induced superconductivity inside the ferromagnet is small compared to superconducting length scales inside the superconductor. This suggests the use of a microscopic theory to describe S/F multilayers. The following results were obtained solving the quasiclassical Eilenberger equations in the clean limit [Eil68] or the much simpler Usadel [Usa70] equations in the diffusive limit, in both cases for a S/F/S junction⁷.

⁶In experiment, as already mentioned in Chap. 2, a single 0 Josephson junction and a single π junction are indistinguishable, as one can only determine $|I_c|$.

⁷In ferromagnets $E_{\text{ex}} \gg k_B T$, thus the variations of the superconducting order parameters are large and cannot be described by the generalized Ginzburg-Landau functional.

In the clean limit, $l \gg \xi_{F1}$, l is the electron mean free path. In the case of an ideal clean material, $\xi_{F1} = \infty$. In reality, ξ_{F1} is reduced due to scattering effects, *e.g.* spin orbit or impurity scattering. However, in the clean limit, always $\xi_{F1} \gg \xi_{F2}$. The dependence of the critical current on the ferromagnetic thickness is calculated [Buz05] as

$$I_c R_n(d_F) = \frac{\pi \Delta^2 |\sin(4E_{\text{ex}} d_F / v_F)|}{16e E_{\text{ex}} d_F / v_F}. \quad (4.2)$$

Thus, the decay of the superconducting wave function is $\sim (1/x)$, it is long ranging. This dependency was observed experimentally in clean S/F structures by [Hal01].

In the diffusive⁸ limit $l \ll \xi_{F1}$. The scattering effects due to impurities, spin orbital or magnetic scattering are much stronger and both characteristic lengths are of the same order, $\xi_{F1} \sim \xi_{F2}$. The correlation decay length is estimated as $\xi_F \equiv \xi_{F2} = \sqrt{\hbar D / E_{\text{ex}}}$, D is the diffusion constant. Here, the dependence of I_c on d_F is given [Buz05] as

$$I_c R_n(d_F) \sim 2 \frac{d_F}{\xi_F} \frac{\cos(\frac{d_F}{\xi_F}) \sinh(\frac{d_F}{\xi_F}) + \sin(\frac{d_F}{\xi_F}) \cosh(\frac{d_F}{\xi_F})}{\cosh(\frac{2d_F}{\xi_F}) - \cos(\frac{2d_F}{\xi_F})}. \quad (4.3)$$

The superconducting wave function decays exponentially in the ferromagnet $\varphi \sim \exp(-\frac{x}{\xi_F})$, the decay is much stronger than in the clean limit.

Whereas scattering effects mainly influence the correlation decay length, the strength of the ferromagnet determines the correlation oscillation length. Strong ferromagnets like Fe, Co, Ni have a strong exchange field, thus their correlation oscillation length ξ_{F2} is comparably small. If they are prepared as high quality metals, they have only few impurities and are in the clean limit. Diluted alloys as PdNi or CuNi have a smaller exchange field, they are in the diffusive limit as they are compositions of different materials. If ferromagnetic Josephson junctions are fabricated using a strong ferromagnet, the decay length might be long and the superconducting wave function penetrates into the ferromagnet to a large extend. The correlation oscillation length is rather small, so several $0-\pi$ transitions should be observable before the superconducting wave function decays. However, it might be hard to resolve the $I_c(d_F)$ dependence for strong ferromagnets. In experiment the resolution of $I_c(d_F)$ is determined by the resolution of the layer thickness, if ξ_{F2} is getting too small,

⁸Sometimes called dirty limit.

the $0-\pi$ transitions cannot be resolved. If one chooses an alloy to have a larger correlation oscillation length which can be resolved in experiment, the decay of the correlation decay length might be too fast to observe a $0-\pi$ transition.

Another important point is the transparency of the junction barriers. Up to now only S/F/S structures were discussed, the transparencies of the barriers were neglected⁹. In the case of S/I/F/S junctions there is an asymmetry between the barrier transparencies. The S/F barrier, if assumed ideal, is highly transparent, $\gamma_{\text{SF}} \sim 0$, with γ being the transparency coefficient. The S/I boundary is not transparent, $\gamma_{\text{SI}} \gg 1$, it should be taken into consideration. A rather new calculation of the critical current dependency on ferromagnetic thickness for S/I/F/S junctions in the diffusive limit was calculated by [WKG⁺06; VGKW08]. In the limit of a thick ferromagnetic layer $d_F \gg \xi_{\text{F1}}$ and at $T \leq T_c$ the authors derived an analytic expression

$$I_c(d_F) \sim \frac{1}{\gamma_{\text{SI}}} \exp\left(\frac{-d_F}{\xi_{\text{F1}}}\right) \cos\left(\frac{d_F}{\xi_{\text{F2}}}\right). \quad (4.4)$$

The damped oscillatory behavior is clearly visible in this equation. The junctions, which are used throughout this thesis, are described using Eq. (4.4), compare [VGKW08].

In the diffusive limit, $\xi_{\text{F1}} \sim \xi_{\text{F2}}$ is valid for $E_{\text{ex}} \gg k_B T$. If $E_{\text{ex}} \sim k_B T$ the exchange field and the temperature are of same importance. In this case the correlation oscillation length and the correlation decay length should be written as [ROR⁺01; BSH⁺06]

$$\xi_{\text{F1,F2}} = \sqrt{\frac{\hbar D}{[E_{\text{ex}}^2 + (\pi k_B T)^2] \pm k_B T}}. \quad (4.5)$$

Eq. (4.5) shows that the correlation decay length ξ_{F1} increases when the temperature is decreased, whereas the correlation oscillation length ξ_{F2} decreases. Thus, by choosing proper junction parameters, a Josephson junction can be driven from a 0 to the π state (and vice versa) by varying the temperature. This is called *temperature-induced* $0-\pi$ transition and has been observed in experiment several times [ROR⁺01; ROVR01; SBLC03; SBLC04; WKG⁺06; BPS⁺09].

⁹Actually, to derive Eqs. (4.2,4.3) there are conditions for the transparencies on both sides. In contrast to SIFS junctions the transparencies are *equal* on both sides, thus we did not comment on them. For further information see [Buz05].

4.3 Fabrication of 0 - π SIFS Josephson junctions with reference junctions

Our SIFS Josephson junctions are fabricated in overlap geometry using Nb/Al- Al_2O_3 /Ni $_{60}$ Cu $_{40}$ /Nb technology [WTK06; WSK07]. Here, we briefly describe the fabrication process; a detailed description of the preparation process can be found in [Wei06].

First, a 160 nm thick niobium bottom electrode is deposited on thermally oxidized Si wafers (4×40 nm niobium, in between 2 nm of copper). For deposition a computer-controlled Leybold Univex 450B magnetron sputtering system is used. Then, a 5 nm aluminum layer is sputtered on top. The aluminum is oxidized in a separate chamber for 30 min at different oxygen pressures, depending on which value of critical current density j_c is desired. As a third layer a thin (2 nm) layer of copper is deposited, then the diluted Ni $_{60}$ Cu $_{40}$ alloy is deposited with thickness d_F . The copper interlayer is necessary to reduce the surface roughness and to guarantee a flat, homogeneous growth of the ferromagnetic alloy. To obtain junctions with a varying ferromagnetic thickness on the same wafer, the alloy is sputtered *wedge-shaped*. As the top electrode a 40 nm niobium layer is deposited. The patterning of the junction mesas is done using optical lithography and Ar ion beam milling. In total, a three photomask process is applied. The mesas are isolated using a selective niobium anodization process. Finally, a 300 nm wiring (niobium) is deposited.

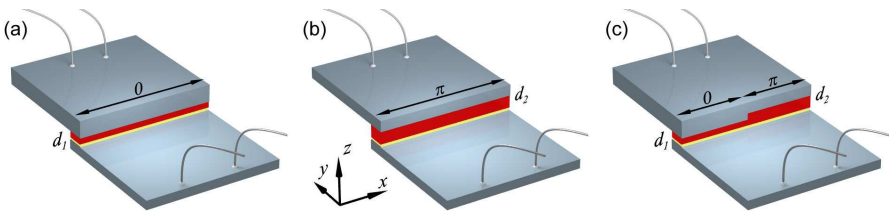


Figure 4.3: Schematic drawing of 0 (a), π (b) and 0 - π (c) SIFS Josephson junctions in overlap geometry. Top and bottom electrodes are colored in light blue (gray), the insulating barrier is yellow (light gray), the ferromagnetic barrier is red (dark gray). For the reference 0 junction $d_F = d_1$ (a), for the π junction $d_F = d_2$ (b). The ferromagnetic barrier of the 0 - π junction has a step-like change in the thickness d_F along the x axis (c).

As the thickness d_F of the ferromagnetic barrier is wedge-shape, Josephson junctions with 0 and π ground states are obtained on each wafer. To fabricate $0-\pi$ SIFS Josephson junctions with its respective reference junctions, the ferromagnetic layer is etched selectively along the wafer. The $0-\pi$ patterning is done after the SIFS multilayer deposition and before the junction mesas are defined by argon-etching and Nb_2O_5 isolation. For that purpose, first the niobium top electrode is selectively removed by dry etching with SF_6 . Then, a few nm of NiCu are taken off by Ar ion-etching. Afterwards, the top electrode is deposited again. Some junctions are etched along the whole junction, in other cases the ferromagnetic layer was selectively etched along one half of the junction, some junctions are not etched. In this way $0-\pi$ junctions are created out of the half-etched junctions [WKG⁺06]: One half of the junction has a F-layer thickness $d_F = d_1$ and, if taken separately, would be in a ground state with a phase drop of zero. The other half of the junction has a F-layer thickness $d_F = d_2$ and, if taken separately, would be in a ground state with a phase drop of π [WKK⁺06]. A schematic drawing of such a $0-\pi$ Josephson junction and its two reference junctions is shown in Fig. 4.3. The lengths of the 0 and π parts of the $0-\pi$ junction are equal with a lithographic accuracy of less than $1\ \mu\text{m}$. For each $0-\pi$ junction two reference junctions (one 0 junction with $d_F = d_1$ and one π junction with $d_F = d_2$), having the same length L as the $0-\pi$ Josephson junction, are fabricated in the same run. We assume that the critical current density j_c^0 is the same in the 0 sample and in the 0 -part of the $0-\pi$ junction. Similarly, j_c^π is assumed to be the same in the π Josephson junction and in the π -part of the $0-\pi$ Josephson junction.

Part II

Results

Chapter 5

Conventional characterization of SIFS Josephson Junctions

Previously to this thesis, Dr. M. Weides had successfully fabricated high quality SIFS junctions with Nb/Al-Al₂O₃/Ni₆₀Cu₄₀/Nb technology [WTK06; WSK07]. Using a step-like thickness modulation of the ferromagnetic layer [WKK⁺06], he had intentionally produced *triplets* of junctions, *i.e.*, 0- π junctions with 0 and π reference junctions, see Sec. 4.3. In first measurements the static properties of short, linear junctions were investigated [WKG⁺06; WKK⁺06]. It was shown that these SIFS junctions could be driven from the overdamped to the underdamped regime [WKG⁺06] by changing the temperature between 4.2 K < T < 2.5 K.

In this chapter we present continuative studies on the static and dynamic properties of 0- π SIFS Josephson junctions as well as of the corresponding reference junctions. Junctions of different lengths, ranging from the short ($l < 1$) to the long ($l \sim 5$) limit, and junctions of different geometries (linear and annular) are investigated. In the first section, sample geometries and parameters are summarized, the two measurement setups are described in brief. In the second section, we concentrate on the static properties of a short 0- π junction. A strong signature of the 0- π boundary is demonstrated by measuring the critical current as a function of two components (B_x , B_y) of an in-plane magnetic field. Then, peculiarities among the magnetic field dependencies of long junctions are

examined. In the third and fourth sections it is demonstrated, that SIFS junctions exhibit a rich dynamical behavior in the underdamped limit, such as resonant steps on the current-voltage characteristics. Varying the experimental conditions, zero field steps, Fiske steps and Shapiro steps are observed. The experimental evidence of *half-integer zero field steps* in $0-\pi$ SIFS junctions is presented. Experimental data are compared with numerical simulations and analytics. The last section summarizes the results of this chapter.

The intentions of these *conventional* studies are twofold: First, we want to test whether SIFS junctions exhibit a regular Josephson physics behavior. We address the question whether there are — in contrast to standard SIS Josephson junctions — differences in the dynamic and static properties of SIFS junctions which are due to the ferromagnetic layer. For this purpose we focus on the investigation of the reference junctions. Second, we concentrate on the physics of the phase shift, *i.e.* on the special properties which are due to the $0-\pi$ boundary. In this context the ferromagnetic layer is only a *tool* to realize the phase shift but not an object of matter. At each time, we precisely try to distinguish which features are related to the ferromagnetic layer or to the phase shift.

Parts of this chapter were published in J. Pfeiffer *et al.*, *Static and dynamic properties of 0 , π , and $0-\pi$ ferromagnetic Josephson tunnel junctions*, Phys. Rev. B **77**, 214506 (2008).

5.1 Samples and measurement techniques

Below we present data of several SIFS Josephson junctions. The samples are situated on four different chips (chip SFS64I, chip JJF16, chip SINFS-F11-Ig, chip AJJ19-H-sm). Usually, on each chip a $0-\pi$ junction with its two reference junctions is examined. Linear samples are produced in *overlap* geometry. Two different designs of the electrodes are used to bias the linear junctions. The annular junctions are designed in *Lyngby*-geometry [DDKP85]. Microphotographs of two linear $0-\pi$ junctions are shown exemplarily in Fig. 5.1, (a) is sample SFS64I/ $0-\pi$, (b) is sample JJF16/ $0-\pi$. Top and bottom electrodes are indicated, as well as the junction areas and the 0 and π parts. The geometrical dimensions and further junction parameters of all measured samples are summarized in Tab. 5.1, a detailed description of all samples can be found in the appendix. The thickness d_I of the insulating barrier is different between the

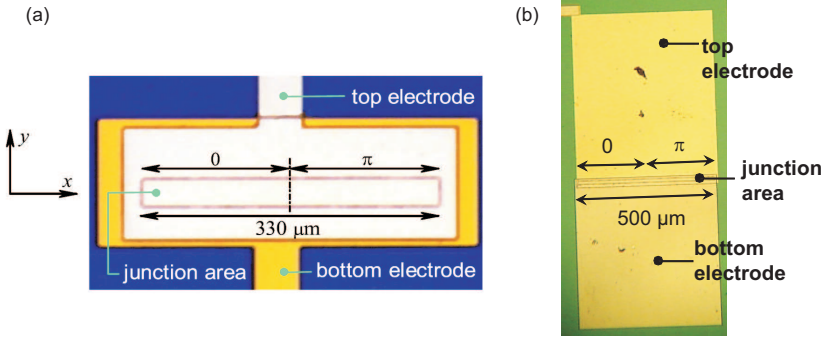


Figure 5.1: Microphotographs of two 0 - π junctions. (a) shows sample SFS64I/ 0 - π and (b) shows sample JJF16/ 0 - π . Top and bottom electrodes, the respective junction areas, the 0 and π parts, as well as the junction lengths are indicated. (a) is taken from [WKK⁺06].

four chips, resulting in different critical current densities, see Tab. 5.1. The critical current densities of the reference junctions are obtained by measuring their critical current dependencies on magnetic field, $I_c(B)$. For 0 - π Josephson junctions only the average value $j_c^{0-\pi} = (|j_c^\pi| + j_c^0)/2$ is quoted as a simplified picture. $j_c^{0-\pi}$ is used to calculate the normalized lengths l of the 0 - π Josephson junctions. In order to calculate l idle region corrections were taken into account [MCM95; Wal01]¹. Note that early measurements using sample set SFS64I were already published [WKK⁺06]. The measurements reported here were performed at least eight months later. It turned out that some parameters, *e.g.*, j_c values, slightly changed with time probably due to the clustering in the F-layer and degradation of the interfaces.

The measurements were carried out in a standard ^4He cryostat (University of Tübingen, custom-made) or ^3He cryostat (Oxford Instruments, Heliox). Pumping the helium bath of the ^4He cryostat, temperatures from 4.2 K down to 2.1 K are reachable. Using the ^3He cryostat, temper-

¹The idle-region is defined as the overlap-region between top and bottom electrodes which surrounds the Josephson junction area. The presence of the idle-region modifies the phase velocity of electromagnetic waves in contrast to the *naked* junction. There are two effects: Idle-region along the junction length increases the velocity of the electromagnetic waves (lateral idle-region, determined by W_i), idle-region at the extremities of the junctions decreases the velocity (longitudinal idle-region). Estimations for our SIFS samples showed, that longitudinal idle-region effects are comparably small, thus we neglect them.

id	j_c (A/cm ²)	l	L (μm)	W (μm)	W_i (μm)
SFS64I/0	2.1	0.72	330	30	50
SFS64I/ π	1.5	0.62	330	30	50
SFS64I/0- π	1.8	0.67	330	30	50
JJF16/0	13.4	3.1	500	12.5	10
JJF16/ π	4.5	1.8	500	12.5	10
JJF16/0- π	9.0	2.5	500	12.5	10
SINFS-F11-lg/0	16.6	4.0	500	10	5
SINFS-F11-lg/ π	23	4.7	500	10	5
SINFS-F11-lg/0- π	19.8	4.3	500	10	5
AJJ19-H-sm/0*	1.1	1.1	628	4	2
AJJ19-H-sm/ π	3.2	2.2	628	4	2
AJJ19-H-sm/0- π	2.2	1.6	628	4	2

Table 5.1: Parameters of the investigated samples. The critical current densities of chip JJF16 are measured at $T = 0.34$ K, the other values at $T = 4.2$ K. L is the length of the junction; for annular samples on chip AJJ19-H-sm L is the circumference. l is the respective normalized length. W is the width of the junction, W_i is the width of the idle region. The parameters of junction AJJ19-H-sm/0* are estimated from other samples on the wafer, as this sample is broken. Idle region corrections are considered according to Ref. [MCM95].

atures between 1.9 K and 310 mK are accessible. In both measurement setups several mu-metal and/or cryoperm shields are placed around the sample to shield it from the earth's magnetic field and other stray fields. Each sample could be prepared in a flux-free state by a cycling procedure, *i.e.*, the sample was warmed above the critical temperature and cooled down again. Within the ³He setup, an external magnetic field can be applied in-plane of the junctions, using the ⁴He cryostat a magnetic field can be applied in all three spatial directions. The samples were current-biased using a custom-made current source, the voltage signal was fed into custom-made preamplifiers. Current sources and preamplifiers were battery powered to provide low noise. At different temperature stages, commercial and custom-made filters were used. To record the experimental data the program GOLDEXI [Gol] was used.

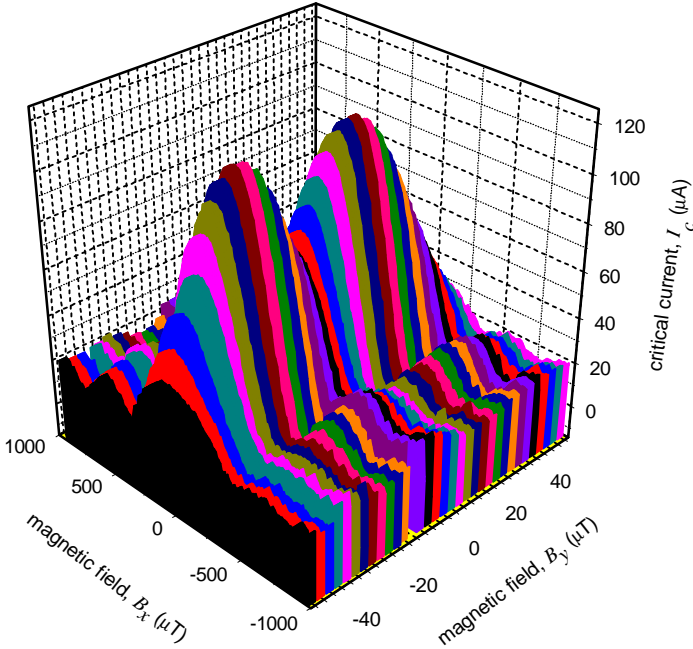


Figure 5.2: Experimental data of an $I_c^{0-\pi}(B_x, B_y)$ measurement of sample SFS64I/ $0-\pi$ at $T = 4.2$ K. The voltage criterion is $V_c = 0.5 \mu\text{V}$.

5.2 Static properties of $0-\pi$ SIFS junctions

5.2.1 Magnetic field dependence of short $0-\pi$ junctions

The static properties of sample set SFS64I are studied exemplarily by measuring the dependencies of the critical current on magnetic field $I_c(B)$. The junctions were cooled down in the absence of externally applied magnetic field and bias current to provide a flux free state. Magnetic fields with both x and y components can be applied in the plane of the junctions, compare Fig. 5.1. The $I_c^0(B_x, B_y)$ and $I_c^\pi(B_x, B_y)$ dependencies of the 0 and π reference junctions have almost perfect Fraunhofer patterns (data not shown) indicating a state without trapped parasitic flux². The maxima of the curves show a small offset from zero magnetic field presumably due to a weak net magnetization of the ferromag-

²Data of these reference junctions were already published in [WKK⁺06].

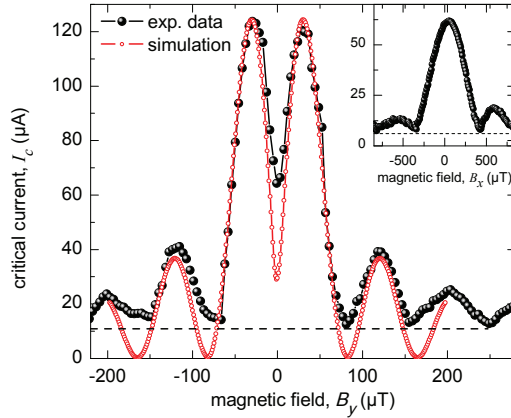


Figure 5.3: Comparison between experimental data and simulation of the $I_c(B_y)$ dependence, $B_x = 0$, at $T = 4.2$ K for $l = 0.67$ and $\delta = 0.71$ (sample SFS64I/ $0-\pi$). Inset: Dependence of the critical current on B_x at $B_y = 0$. The zero-level due to a voltage criterion of $V_c = 0.5 \mu\text{V}$ is indicated as a dashed line.

netic layer. These offsets from zero magnetic field were different in each cooldown, when the samples were cooled down from room temperature through their Curie temperature³. By applying only B_x , the field value at the first minimum of the $I_c(B_x)$ dependence is ~ 11 times larger than the corresponding value on the $I_c(B_y)$ curve. This is due to the ratio between the length L and the width W of the Josephson junctions on chip SFS64I ($L/W = 330/30$).

Fig. 5.2 shows the $I_c^{0-\pi}(B_x, B_y)$ dependence of junction SFS64I/ $0-\pi$. Applying magnetic field in x direction results in a rather symmetric Fraunhofer pattern, indicating that no substantial amount of parasitic flux is trapped in the junction or its electrodes. Noticeably, the height of the side maxima for negative values of B_x is reduced in comparison to the ones for positive B_x field values. A comparable asymmetric height of the side maxima is observed for many of our SIFS Josephson junctions. By applying magnetic field in y direction a well pro-

³The Curie temperature of a comparable NiCu film with 10 nm thickness was determined as $T_c = 225$ K [Wei06]. Furthermore, offsets from zero magnetic field are observed for almost all SIFS samples in this thesis. There is no clear correlation *e.g.* between strength of the offset and length of the junction. There only seems to be a correlation between samples on the same wafer: Among several fabrication processes the samples on *one* wafer show a similar behavior regarding the net offset.

nounced minimum around zero field becomes visible. This minimum is a characteristic feature of a $0-\pi$ Josephson junction [WVHL⁺93; KMS97; SAB⁺02; GKK02; GKK03]. Thus, Fig. 5.2 strongly indicates that the observed behavior is due to the step in the ferromagnetic barrier and not due to some other reasons. The calculated normalized junction length is $l = 0.67$ at $T = 4.2$ K. In contrast to earlier investigations of this sample [WKK⁺06] the idle region corrections [MCM95; Wal01] are taken into account. The magnetic flux of the semifluxon is roughly estimated as $\Phi = \Phi_0 l^2 / 8\pi \lesssim 2\% \Phi_0$. Thus, as the portion of the semifluxon is negligibly small, the minimum in the Fraunhofer pattern is a signature of the $0-\pi$ boundary, not of the pinned semifluxon. Although the junction is short in terms of λ_J ($l < 1$), I_c in the central minimum on the $I_c^{0-\pi}(B_y)$ dependence does not reach zero as it should be for a short Josephson junction [GSG⁺04]. The asymmetry factor is estimated as $\delta = j_c^\pi / j_c^0 = 0.71$, *i.e.*, the critical current densities in the 0 and π parts differ by about 30%. For such an asymmetry the ground state is fluxless [BKS77; BKS78]. To gain a deeper insight, simulations are performed using the ACTIVLLJJA.EXE software [act09]. In Fig. 5.3 the experimental data of an $I_c(B_y)$ pattern of sample SFS64I/ $0-\pi$, at $B_x = 0$ and at $T = 4.2$ K, are compared with simulations ($l = 0.67$, $\delta = 0.71$). For means of comparison, an $I_c(B_x)$ dependence at $B_y = 0$ is shown in the inset. The zero-level due to a voltage criterion of $V_c = 0.5 \mu\text{V}$ is indicated as a dashed line⁴. Although the overall agreement between experiment and numerics is pretty good, there are slight differences between both. In numerics, the height of both maxima is equal, whereas in experiment there is a small asymmetry. In simulation, the central minimum is deeper than in experiment (note, that even in simulations it is not equal to zero due to the asymmetry between 0 and π part). The most ostentatious difference is the occurrence of bumped side minima in experiment, which are not reproduced in simulations. Besides simple explanations for these differences (like trapped flux in the electrodes of the sample in experiment), there are fundamental reasons why our experimental data are not fully reproduced in numerics: We do not take magnetic properties of the ferromagnetic layer into account in our simulations. As already stressed, in experiment the central maxima of the magnetic field dependencies of the reference junctions are shifted along the field axis (for less than one period, data not shown). Thus, the samples on chip SFS64I might have a small in-plane magnetization. The ferromagnetic layer is in a multiple

⁴In experiment the zero-level is determined by the voltage criterion V_c as $I_{c,\min} = V_c/R$. R is the subgap resistance which is determined from IV measurements.

domain state, compare Ref. [SOR⁺08]. The remanent magnetization of the F-layer can be different in the 0 and π parts. Additionally, the effective magnetic thickness of the junction depends on the F-layer, resulting in asymmetric flux penetration in the 0 and π parts. M. Kemmler *et al.* [KWW⁺09] present an extensive study on the influences of a small field-dependent magnetization and a F-layer thickness dependent magnetic thickness on the $I_c(B)$ pattern of short SIFS junctions. They show that the magnetic properties of SIFS junctions strongly influence the $I_c(B)$ pattern and can result in bumped minima and asymmetric maxima.

5.2.2 Magnetic field dependence of long $0-\pi$ junctions

In this subsection, the magnetic field dependence of long ($l \sim 5$) Josephson junctions is examined. The junctions are cooled down in zero magnetic field, the external magnetic field B_y is applied in plane as described before⁵. The experimental data of sample SINFS-F11-lg/ $0-\pi$ at temperatures between $3.1 < T < 4.2$ K are shown exemplarily in Fig. 5.4. The minimum critical current $I_{c,\min}$ due to a voltage criterion of $V_c = 1 \mu\text{V}$ varies with temperature between $12.5 \mu\text{A} < I_{c,\min} < 33 \mu\text{A}$, thus the zero-level(s) are indicated as a broad, dashed line. As expected for long $0-\pi$ junctions, the central minimum around zero field is not very pronounced, it does not go down to zero critical current, see Sec. 2.3. The $I_c(B)$ pattern were measured in both field directions, the magnetic field was swept up and down resulting in the same experimental data. The central minima of the $I_c(B)$ pattern do not coincide with zero magnetic field, the curves are shifted to positive magnetic field values. The overall inclination of the $I_c(B)$ pattern to the right side is due to a self-field effect, which was proven by changing the polarity of the bias current. In this context, self-field corrections account for the fact that bias leads lead to magnetic field contributions. For sample SINFS-F11-lg/ $0-\pi$ the asymmetry factor at $T = 4.2$ K is calculated as $\delta = 1.4$; the magnetic flux in the ground state is estimated to be $\Phi = 74\% \Phi_0$.

In contrast to short $0-\pi$ junctions, there are two peculiar features in the $I_c(B)$ pattern of sample SINFS-F11-lg/ $0-\pi$ which should be noticed: First, as visible in Fig. 5.4, the side minima of the $I_c(B)$ of junction SINFS-F11-lg/ $0-\pi$ do not go to zero-level. Instead there seems to be an intersection between the minima and some linear branches, resulting

⁵In this measurement cycle a small custom-made coil was used. Unfortunately, this coil is not calibrated.

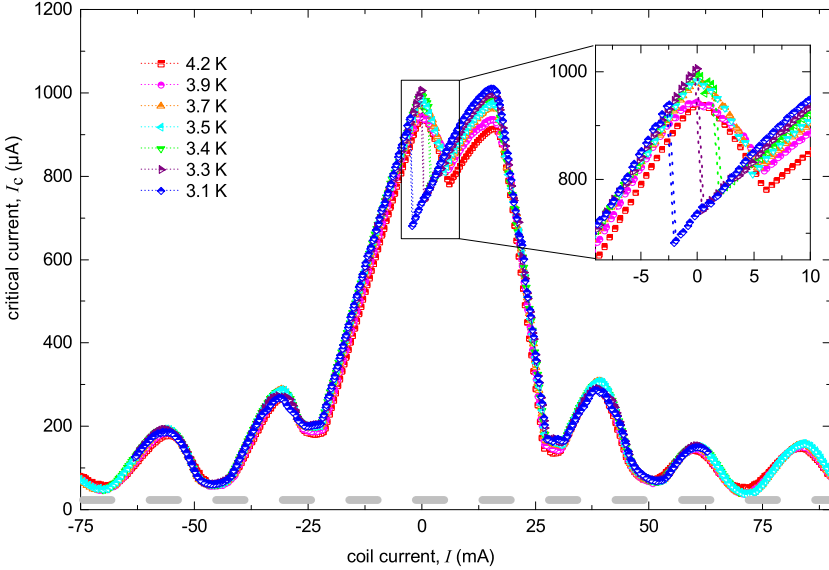


Figure 5.4: Experimental data of critical current vs. magnetic field dependencies of junction SINFS-F11-lg/ $0-\pi$ at different temperatures between $3.1 \text{ K} \leq T \leq 4.2 \text{ K}$. The inset shows an enlargement of the central minimum. The zero-level(s) due to a voltage criterion of $V_c = 1 \mu\text{V}$ are indicated as a thick, dashed line.

in flat plateau-like structures. The height of the respective plateau decreases with the number of the side minima, *e.g.*, the first plateau has higher critical current values than the next one.

Second, as the temperature decreases, starting from $T = 3.4 \text{ K}$, there is a jump occurring on the left maximum of the $I_c(B)$. The curve cannot be traced out continuously. At some magnetic field values the junction switches to a state with a lower critical current value. The switching point changes as the temperature decreases. The lower the temperature, the sooner (lower magnetic field values) the jump occurs. Thus, with decreasing temperature, the jump height gets larger. Interestingly, there is no clear correlation between the crossover to the underdamped limit ($T \sim 3.9 \text{ K}$) and the onsets of jumps ($T \sim 3.4 \text{ K}$) on the $I_c(B)$ dependence. Similar jumps on the magnetic field dependencies were also observed for the intermediate length junction JFF16/ $0-\pi$ and another $0-\pi$ junction located on wafer SINFS-F11-lg (data not shown). It has

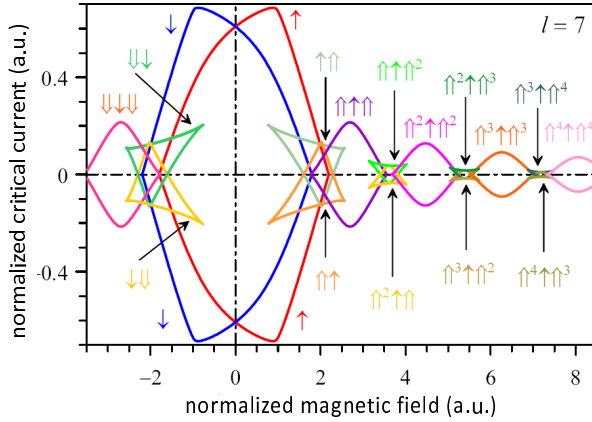


Figure 5.5: Numerically simulated critical current vs. magnetic field dependence of a long, symmetric $0-\pi$ junction ($l = 7$, $\delta = 1$). Modified from [GBA09]. Various fluxon/semifluxon configurations are indicated by arrows. \uparrow : fluxon, \uparrow : semifluxon.

to be pointed out that the longer the junction, the more pronounced is the observed asymmetry of the $I_c(B)$ pattern. Similar jumps were not found for $0-\pi$ junctions in the short limit.

A deeper understanding of the physics behind the $I_c(B)$ pattern is obtained by numerical simulations with the underlying sine-Gordon equation, compare Sec. 1.4.1. The calculations have been performed by E. Goldobin *et al.* [GBA09]. Using a stability analysis, the authors are able to obtain the $I_c(B)$ dependencies of long $0-\pi$ junctions as an envelope of bifurcation curves which correspond to different static solutions. In contrast to other studies, the authors resolve not only an envelope of *all* static solutions (switching to resistive state), but also the critical current of *each* individual solution. In Fig. 5.5 an $i_c(B)$ dependence of a symmetric ($\delta = 1$), long $0-\pi$ junction ($l = 7$) is shown exemplarily. Various fluxon/semifluxon configurations (\uparrow : fluxon, \uparrow : semifluxon) are visible. In simulation, at low magnetic field values both solutions, the semifluxon (red)/antifluxon (blue) solution, are found. At zero magnetic field both solutions coincide. At higher magnetic field values a number of more complex fluxon/semifluxon solutions exists. Their composition is indicated by arrows. In contrast to standard 0 Josephson junctions, each oscillation period is correlated with the appearance

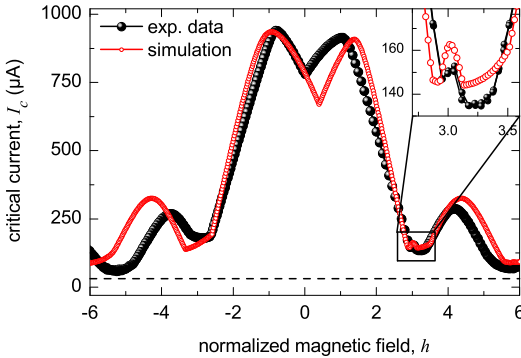


Figure 5.6: Comparison between experimental data (sample SINFS-F11-1g/0- π , black filled squares) and simulation (red open circles) for $l = 4.3$ and $\delta = 1.4$ at $T = 4.2$ K. The experimental data are self-field corrected. The zero-level due to the voltage criterion $V_c = 1 \mu\text{V}$ is indicated as a dashed line. Inset: Enlargement of the first side minimum.

of two additional fluxons (symmetric fluxon solution). As already seen in experiment, there are branches intersecting the oscillation minima. These branches carry an odd number of fluxons. In experiment only the envelope of the different states can be measured: Often, the state with the highest critical current at a respective magnetic field value is measured. For example at low field values, the respective semifluxon (\uparrow) / antisemifluxon (\downarrow) configuration depends on the orientation of the magnetic field: If the magnetic field direction is positive, the semifluxon is also pointing upwards (\uparrow), *i.e.* is oriented parallel to the magnetic field. This configuration is the energetically more favorable. If the magnetic field direction is negative, the semifluxon is pointing downwards (\downarrow), again parallel to the magnetic field⁶.

In Fig. 5.6 a comparison between numerical (red open circles) and experimental data (black filled squares) is shown. The experimental data of sample SINFS-F11-1g/0- π at $T = 4.2$ K are chosen ($l = 4.3$ and $\delta = 1.4$), the numerical simulations are performed with corresponding parameter values⁷. Here, only the transition to the resistive state is considered. To compare experiment with numerical calculations, the experimental data

⁶Actually, the orientation of the semifluxon also depends on the history of the system. Using an experimental trick, the semifluxon/antisemifluxon branches can be traced out completely, see next subsection.

⁷For simulations the ACTIVLLJJA.EXE software [act09] is used.

are self-field corrected and offset-corrected using the GOLDEXI maths tools [Gol]. The y -axis of Fig. 5.6 is given in physical units, the conversion of the numerical data is performed by adjusting the maximum value of the left maximum, both in numerics and experiment. The x -axis is chosen in normalized units as the coil was not calibrated. The magnetic field axis is normalized to the first critical field of a long Josephson junction, as introduced in Sec. 2.1. The lower limit of the I_c -detection due to a finite voltage criterion of $V_c = 1 \mu\text{V}$ is indicated as a dashed horizontal line. The comparison between numerical and experimental data reveals a good qualitative agreement. In both cases the central minimum is V-shaped. The shape of both maxima is not symmetric, in the experimental as well as the simulated case one maximum is wider than the other one. As already pointed out, in both cases the side minima do not go down to zero-level. This behavior can be easily explained by the existence of some odd fluxon/semifluxon branches. Even small features as peaks within the first side minimum on the right side are visible in experiment as well as in numerics, see inset of Fig. 5.6. Interestingly, this first side minimum has a complicated substructure: The plateau-like shape is due to the $\uparrow\uparrow$ solution for positive bias current (indicated in pale green in Fig. 5.5), the peak is a remnant of the $\uparrow\uparrow$ solution for negative bias current (orange in Fig. 5.5). However, there are differences between experimental data and simulations. In simulation, the central minimum is deeper than in experiment, and the oscillation period is a bit larger. The shape of the first side minimum on the left side is different in numerical and experimental data. As in the last subsection⁸, we interpret these differences as a fingerprint of the magnetic properties of the ferromagnetic layer. The offset of the $I_c(B)$ measurement from zero magnetic field is an indication for a small in-plane magnetization of the samples on chip SINFS-F11-1g.

Concerning the jumps on the $I_c(B)$ pattern shown in Fig. 5.4, theoretical work was done by G. Rotoli *et al.* [RSC⁺08]. In contrast to other studies, in this work, damping is a matter of interest and is changed in simulations. The authors predicted jumps on the magnetic field dependence and interpreted them as a switching between unstable fluxon/semifluxon configurations and the resistive state. They predict the $I_c(B)$ to be asymmetric with respect to the semifluxon polarity, thus the shape of the $I_c(B)$ depends on the initial state of the semifluxon. They identify so-called *flip-lines*, where the semifluxon changes polarity at lower bias currents than the critical current of the junction. These flip-lines

⁸Unfortunately, the model of M. Kemmler *et al.* is not applicable to long junctions.

should only be traced by preparing the semifluxon in a defined state, see next subsection. As the switching to the resistive state (by the emission of fluxons/antifluxons) is easier at low dissipation, the visibility of the asymmetry should depend on damping. These features are first observed in our experimental data, see Fig. 5.4. The lower the temperature (thus, the damping), the more pronounced is the asymmetry of the $I_c(B)$. In the measurements shown in Fig. 5.4 the asymmetry is only partially visible. Changing the polarity of the bias current is not sufficient to observe the reverse asymmetry (*i.e.*, we do not observe jumps in the right maximum). This might be due to the fact, that the $I_c(B)$ pattern of our SIFS junctions are not centered around zero magnetic field, they are shifted due to the remanent magnetization of the F-layer. Here, the magnetization of sample SINFS-F11-Ig/0- π is positive, shifting the whole $I_c(B)$ pattern at $T = 4.2$ K to positive field values. At $T = 3.4$ K the jump occurs at positive magnetic field values, at $T = 3.3$ K the jump occurs around zero field. Only at $T = 3.1$ K the curve switches at negative field values, and the semifluxon changes polarity *before* its energetically favorable magnetic field orientation is reached. We conclude, that the direction of the remanent magnetization might break the symmetry of the junction, *i.e.*, that the magnetization favors one orientation of the semifluxon. As already indicated, in order to trace unstable fluxon/semifluxon configurations, a special adapted measurement technique is necessary.

Captain's log: supplement

Here, we present $I_c(B)$ measurements of the annular sample AJJ19-H-sm/0- π . A microphotograph of the sample is shown in Fig. 5.7. Top and bottom electrodes are indicated, likewise the 0 and π parts. The junction is cooled down in zero magnetic field, as described before. The magnetic field is applied in plane of the junction, parallel to the diameter, which separates the 0 and π parts, see Fig. 5.7. By doing so, the junction behaves qualitatively as a linear 0- π junction — as an approximation, the annular, 2-dimensional geometry is projected onto a 1-dimensional line.

In Fig. 5.8 the experimental data of an $I_c(B)$ measurement of junction AJJ19-H-sm/0- π at $T = 4.2$ K are shown. The central minimum around zero magnetic field is a clear fingerprint of the 0- π boundary. The $I_c(B)$ pattern is highly symmetric, indicating the high quality of the junction and its uniform current distribution. At $T = 4.2$ K there is almost no

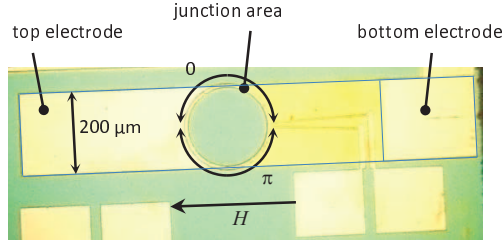


Figure 5.7: Microphotograph of sample AJJ19-H-sm/ $0-\pi$. The top and bottom electrodes are indicated, as well as the 0 and π parts. The magnetic field direction is depicted by an arrow.

offset from zero magnetic field observed, the shape of the side minima is surprisingly sharp, there are no typical indications of the F-layer like bumped or plateau-like minima. At $T = 4.2$ K no jump is visible on the $I_c(B)$ curve ($l = 1.6$, $\delta = 2.9$ at $T = 4.2$ K), but at $T = 2.8$ K a small asymmetry is visible, see Fig. 5.8 (b). The junction is of intermediate length, thus the jump height is expected to be rather small. We tried to trace out unstable fluxon/semifluxon configurations which are predicted in theory and were described in detail in the last subsection. We concentrate on the crossing of the two semifluxon solutions in the central minimum. In Fig. 5.8 (b) our *standard* $I_c(B)$ measurement is shown. The measurement software GOLDEXI [Gol] is designed in a way that the magnetic field is changed continuously. In Fig. 5.8 (c) the magnetic field is set to its initial value before measuring at each magnetic field value, *e.g.*, when sweeping from negative to positive magnetic field values, the initial value of the magnetic field is set to $B = -100 \mu\text{T}$. The negative to positive and positive to negative field sweep directions are done separately. In this way always the same semifluxon configuration is prepared *before* each measurement. Doing so, parts of the unstable semifluxon/ant semifluxon solutions could be traced out, see Fig. 5.8 (c). It is clearly visible that the system switches between the two states.

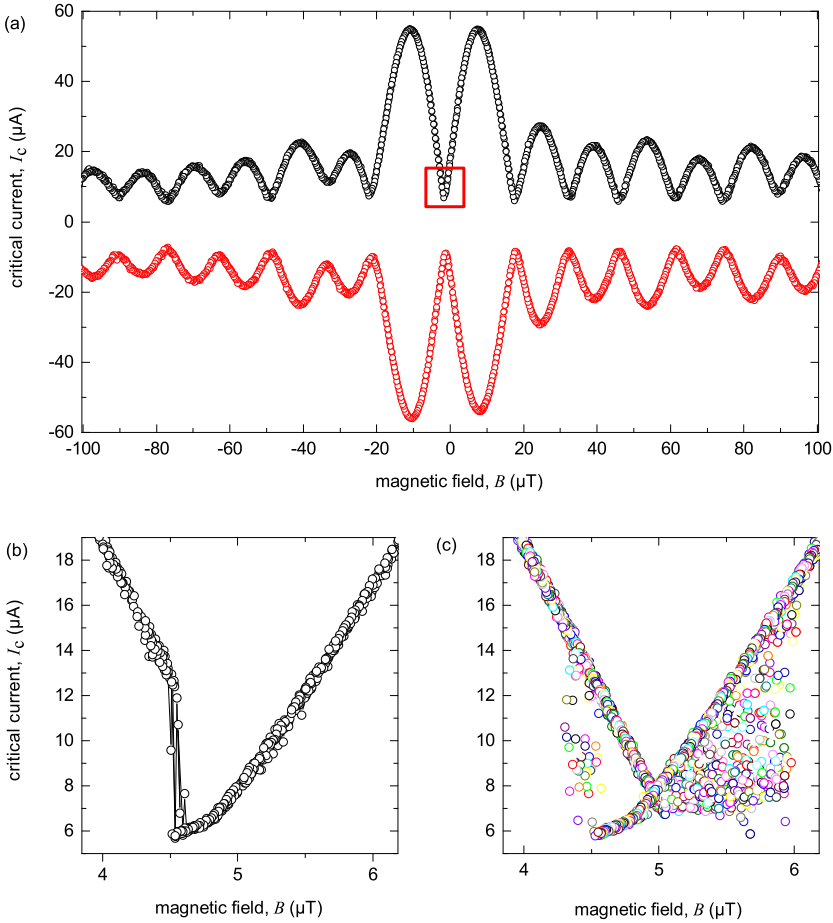


Figure 5.8: Experimental data of magnetic field dependencies of sample AJJ19-H-sm/0- π . (a) The positive and negative $I_c(B)$ pattern are measured at $T = 4.2$ K. The red box indicates the region which is enlarged in (b) and (c). The measurements in (b) and (c) are taken at $T = 2.8$ K. During measuring the $I_c(B)$ pattern in (c), the magnetic field is set to $\pm 100 \mu\text{T}$ before measuring at each magnetic field value. In (b) the magnetic field is increased continuously.

5.3 Dynamic properties of short and intermediate SIFS Josephson junctions

In the following, dynamic properties are studied by measuring current-voltage (I - V) characteristics (IVC). The IVC directly reveals the relationship between the average flux velocity v , which is proportional to the measured dc voltage V , and the driving force, which is proportional to the bias current I . Linear junctions in the short and intermediate length limit are considered. To observe dynamics, the junction under examination has to be in the underdamped regime. The SIFS junction parameters allow to investigate the overdamped as well as the underdamped regime by varying the temperature between 310 mK and 4.2 K.

5.3.1 Half-integer zero field steps

If IVC measurements are carried out in the absence of magnetic field or microwaves one will observe so-called zero field steps (ZFSs) on the IVC of a Josephson junction, provided the junction is long enough, see Subsec. 1.4.2. In the presence of magnetic field, Fiske steps emerge (see Subsec. 1.3.3) having a voltage spacing which is two times smaller than the one of ZFSs. Both are visible as resonant structures on the IVC curve.

ZFSs and Fiske step measurements are performed with the 0 and π junction of sample set SFS64I. In this measurement cycle, the $I_c(B_y)$ pattern of both reference junctions showed almost no offset from zero magnetic field⁹. In both cases, the dynamics follow exactly the expectations from standard 0 Josephson physics (data not shown). There are no peculiarities observable, which might be due to the ferromagnetic layer.

In case of sample SFS64I/0- π the first ZFS emerges at exactly *half* of the usual ZFS spacing, *i.e.*, exactly at *the same* voltage as the first Fiske step, in accordance to earlier predictions [Ste02; Laz04] and to experiments on 0- π Josephson junctions of other types [GSG⁺04]. Fig. 5.9 (a) shows IVC measurements of sample SFS64I/0- π taken at different T and

⁹Actually, the definition of ZFSs as resonances *without* applied magnetic field should be modified for SIFS junctions. ZFSs are observed in the central minimum (0- π junctions) or in the central maxima (reference junctions) of the $I_c(B)$ dependencies. If a SIFS junction shows an offset from zero magnetic field, the corresponding field value has to be *applied* to observe ZFSs. This is a fundamental difference between SIS and SIFS junctions: In case of SIFS junctions the system has to be prepared in its *own* zero field to observe ZFSs.

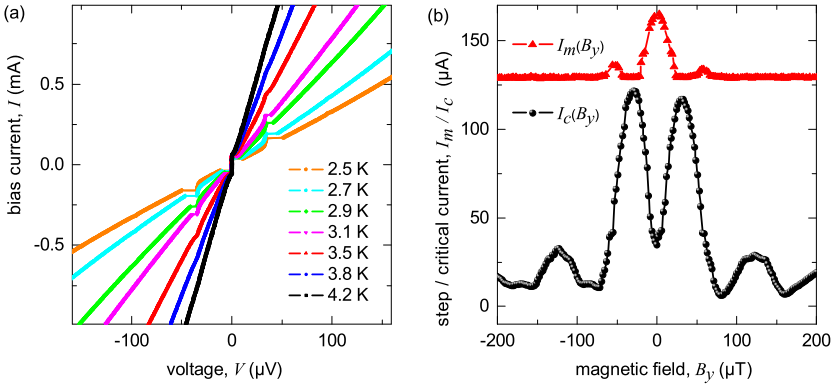


Figure 5.9: (a) Experimentally measured IVCs of Josephson junction SFS64I/0- π at different temperatures. At $T < 3.8$ K the half-integer zero field step emerges. (b) The dependence of the maximum step current $I_m^{0-\pi}$ of the first half-integer ZFS at $V = 35 \mu\text{V}$ on magnetic field B_y (red triangles), measured at $T = 2.5$ K. The $I_c^{0-\pi}(B_y)$ dependence is shown for comparison (black dots).

at $B = 0$ (for comparison see Fig. 5.9 (b): No offset from zero magnetic field is observed). At $V = 35 \mu\text{V}$, which is exactly the observed value of the Fiske step voltage spacing in this sample, a step is emerging for $T < 3.8$ K. The step appears due to the flipping of a fractional vortex (semifluxon) [GSG⁺04]. At zero bias current, for our Josephson junction length and j_c asymmetry, the ground state of the system is a flat phase state $\mu = 0$ (fluxless). As soon as a uniform bias current is applied, a fractional flux is localized at the 0- π boundary [GKK03]. Since the junction has a finite length, the interaction of the semifluxon with the boundary can be treated as the interaction of the semifluxon with an antisemifluxon (image) situated outside the junction at the same distance from the edge. There are two such images, one next to the left and one next to the right edge of the Josephson junction, compare Sec. 2.4. The bias current exerts a Lorenz force which pulls the fractional vortex. If the bias current is large enough, both the semifluxon and the image vortex flip, changing polarity and exchanging one flux quantum, which, in fact, is passing through the Josephson junction boundary. Then a similar process takes place between the fractional vortex (now of negative polarity) and another image, so one Φ_0 passes through the other Josephson junction boundary. Assuming that the maximum velocity of

flux transfer is the Swihart velocity \bar{c} , we calculate that the asymptotic voltage is exactly equal to the voltage of the first Fiske step.

In order to show that the observed step is indeed a ZFS, the maximum current $I_m^{0-\pi}$ of this step versus magnetic field B_y is measured, see Fig. 5.9 (b). The $I_m^{0-\pi}(B_y)$ dependence has a maximum in zero field and is decreasing with applied magnetic field — a typical behavior of a ZFS. The background value of $I_m^{0-\pi}$ corresponds to the current on the McCumber branch at $V \approx 35 \mu\text{V}$ below which the step cannot be suppressed in principle. Fig. 5.9 (b) additionally shows the $I_c^{0-\pi}(B_y)$ curve measured at the same temperature of $T = 2.5 \text{ K}$ for comparison. The minimum around $B_y \approx 0$, typical for $0-\pi$ Josephson junctions, is visible. Note that the amplitude of $I_c(B_y)$ is higher than in Fig. 5.2 as the temperature is lower. The next ZFS emerges at $\sim 100 \mu\text{V}$ ($n = 3/2$) and corresponds to one additional fluxon moving inside the $0-\pi$ Josephson junction. It is only very weakly visible in Fig. 5.9 (a), it is more pronounced at lower temperatures, see Fig. 5.10. Comparable measurements are performed for sample set JJF16 and show similar results (data not shown). In contrast to earlier measurements [GSG⁺04; Gab07] on artificial $0-\pi$ junctions, no substructures are observed on these half-integer ZFSs. There is no indication visible for the interaction between plasma waves and the step-like inhomogeneity of the junction, which often manifest as substructures on the steps of the IVC.

Up to now half-integer ZFS (hiZFS) have been observed only in artificial $0-\pi$ junctions [GSG⁺04]. To our knowledge, here we report on the first measurements of a half-integer ZFS in $0-\pi$ SIFS junctions.

Numerical analysis of resonances in short $0-\pi$ junctions

To gain a deeper insight into the dynamics of short $0-\pi$ junctions, numerical simulations are performed using the SKJJ32.EXE [Skj09] software which basically solves the underlying sine-Gordon equation. Exemplarily, IV measurements of sample SFS64I/ $0-\pi$ at $T = 1.5 \text{ K}$ are presented, see Fig. 5.10. The experimental data are obtained in the absence of applied magnetic field, the 0.5th and 1.5th ZFS are visible. The corresponding $I_c(B)$ pattern is symmetric and does not show signs of trapped flux¹⁰ (data not shown), thus no Fiske steps are observed. Simulations are done with parameters extracted from experiment ($l = 0.7$, $\alpha = 0.1$). The numerically calculated IV curve is superimposed with the experi-

¹⁰In this measurement cycle no offset from zero magnetic field is observed in the $I_c(B)$ dependence.

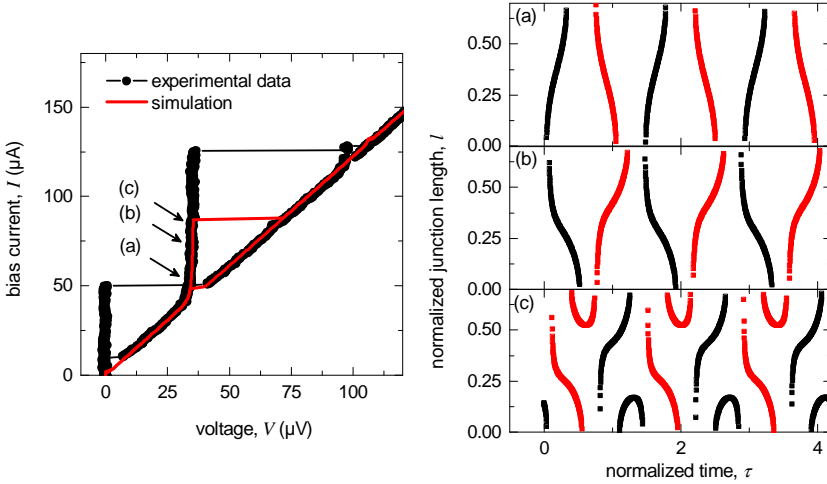


Figure 5.10: Left side: Comparison between experimental data (black filled dots) and numerically simulated (red line) hiZFSs ($n = 0.5, 1.5$), short junction limit. Experimental data: sample SFS64I/0- π was measured at $T = 1.5$ K in the absence of applied magnetic field. Simulations were done with $l = 0.7$ and $\alpha = 0.1$. (a), (b) and (c) indicate bias current values at which trajectories are tracked, see right side. Semifluxons are indicated as black lines, antisemifluxons as red lines.

mental data and shows a good qualitative agreement. The slope of the experimental curve as well as the position of the hiZFS is reproduced with high accuracy. The position of the 1.5th ZFS is at $106 \mu\text{V}$ in simulations, in experiment it is a bit lower. The height of the hiZFS is higher in experiment than in numerics, likewise the critical current. In experiment the depinning current might be higher than in simulations due to some inhomogeneities in the junction. The shape of the hiZFS is plain in both, experiment and numerics, there are no substructures visible on the half-inter ZFS.

In order to identify the modes of semifluxon motion, the trajectories of semifluxons are tracked at several bias current values on the hiZFS (indicated as positions a, b and c in Fig. 5.10). (a) is equal to a normalized bias current of $i = 0.5$, (b) is $i = 0.85$ and (c) corresponds to $i = 0.9$. We define the *center* of semifluxons as points with phase $\mu = \pi/2 + k\pi$, with k being an integer number. To trace the motion of the semifluxons, the time dependent positions x_i^{SF} are calculated for each t . The

index i accounts for the fact that several semifluxons can cycle through the junction. Note, that the semifluxon itself is still pinned at the $0-\pi$ boundary. Here, we focus on the *center* of semifluxons — these points can move inside the junction, if a voltage drop is occurring across the junction and if the phase μ is varying in time.

Fig. 5.10 (right hand side) shows trajectories at the indicated current values. The black lines represent the center of semifluxons, the red lines are centers of antisemifluxons which move in opposite direction. From the trajectories, one can deduce the velocity how fast the center of the semifluxon moves. At a normalized bias current of $i = 0.5$ the center of the semifluxon moves through the junction, leaves the junction at one side and enters the junction at the same side as an antisemifluxon. This cycle is repeated. If the current is increased to $i = 0.85$, the motion is similar, only one semifluxon/antisemifluxon is inside the junction at the same time, see Fig. 5.10 (b). Now, the motion looks a bit distorted, *i.e.*, the motion is not smooth. The antisemifluxon seems to decelerate and accelerate. At an increased driving force of $i = 0.9$, Fig. 5.10 (c), directly before the switching to the resistive branch, the situation looks totally different: The center of the semifluxon leaves the junction and another semifluxon enters it instantaneously at the other side (again as semifluxon).

5.3.2 Fiske steps

In the following, the experimental conditions are changed: By applying a magnetic field B_y to sample set JJF16 various Fiske steps were observed on the IVCs. The data presented below are obtained at $T = 340$ mK (underdamped regime).

The low voltage part of several IVCs of junction JJF16/ π at different magnetic fields in the range of $-105 \dots +105 \mu\text{T}$ is shown in Fig. 5.11 (a). Nine Fiske steps are observed with a high resolution. Similar Fiske step measurements were carried out with samples JJF16/ $0-\pi$ and JJF16/ 0 (data not shown). To summarize these measurements, in Fig. 5.11 (b) the voltage positions of Fiske steps versus step number are plotted for all three samples. The first four Fiske steps have an almost equidistant voltage spacing. For higher Fiske steps the voltage spacing between adjacent Fiske steps shrinks with increasing step number, indicating that the dispersion relation of electromagnetic waves is not linear. Possible reasons might be the layout of the junctions and the fabrication process: inhomogeneities in a junction result in a decreasing voltage

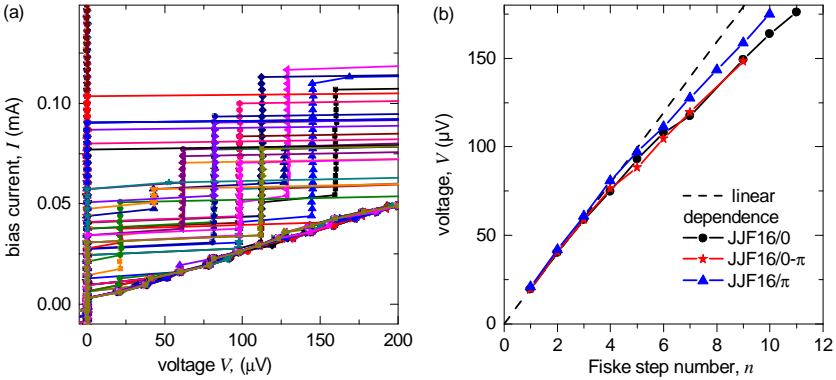


Figure 5.11: (a) Fiske steps on the IVCs of the junction JJF16/ π at $T = 340$ mK. The magnetic field is varied between $B_y = -105 \dots + 105 \mu\text{T}$. (b) Asymptotic voltage of the n -th Fiske step is plotted versus n for sample set JJF16. Taking into account only the first four Fiske steps $\Delta V = 19.9 \mu\text{V}$.

spacing of resonant steps on the IVC, compare Ref. [BMU96]. Local inhomogeneities are, *e.g.*, non ideal junction boundaries, where the profile of the critical current does not sharply go to zero but is smeared out. Likewise, the presence of a large idle region modifies an ideal reflection at the junction boundaries, which is true for our samples. As visible in Fig. 5.11 (b), the Fiske step voltage spacing of the π junction shows the smallest deviation from an equidistant voltage spacing, indicating a better homogeneity as compared to the 0 and $0-\pi$ junction. Note that the F-layer of the last two junctions (or parts of it) is etched during the fabrication process. The etching might cause additional inhomogeneities. This topic was already discussed in the literature as *material dispersion* [LB92; HSBJ94]. The authors had shown that due to idle region effects or a frequency dependent magnetic penetration depth, summarized as material dispersion, the dispersion relation of electromagnetic waves in Josephson junctions is not linear. Another explanation is that j_c^0 is more sensitive to variations in d_F (roughness) than j_c^π because d_1 and d_2 are chosen so that

$$\left| \frac{\partial I_c(d_F)}{\partial d_F} \right|_{d_F=d_1} > \left| \frac{\partial I_c(d_F)}{\partial d_F} \right|_{d_F=d_2}, \quad (5.1)$$

see Fig. 1 of Ref. [WKG⁺06].

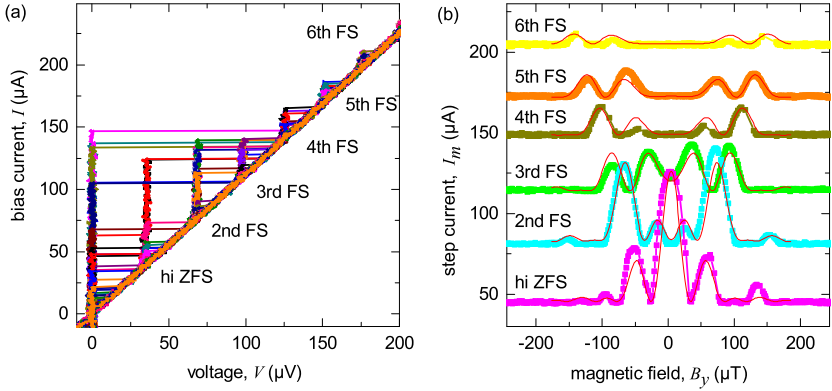


Figure 5.12: (a) Experimental data of Fiske steps on the IVCs of sample JJF16/0- π at $T = 310$ mK. The magnetic field is varied between $B = -200 \dots +200 \mu\text{T}$. hi= half-integer. (b) Maximum current amplitude of the n th Fiske step versus applied magnetic field at $T = 310$ mK. Solid line: Analytical calculations performed according to Ref. [NSAN06] using the experimental parameters of sample JJF16/0- π at $T = 310$ mK.

To calculate the capacitance of the junctions the voltage spacing of the first four Fiske steps is used. The capacitance per junction area is estimated as $C \approx 22.9 \pm 0.8 \mu\text{F}/\text{cm}^2$ which also includes idle region effects. From geometrical considerations the contributions of the idle region (C_i) and the *naked* junction (C_j) to the capacitance $C = C_i + C_j$ can be estimated. The respective capacitance is calculated as $C_{i,j} = \epsilon_0 \epsilon_{i,j} W_{i,j} L / d_T^{i,j}$, L being the length and $W_{i,j}$ being the width of the junction or idle region, compare Tab. 5.1.

Taking $\epsilon_i \sim 30$, $\epsilon_j \sim 10$ and $d_T^i = 120$ nm and $d_T^j = 0.4$ nm, the idle region has a capacitance of $C_i = 221.5$ nF/cm². The Swihart velocity in the naked junction is calculated as $\bar{c} = c \sqrt{d_T^j / \epsilon_j d_j}$ with c being the vacuum speed of light and $\mu_0 d_j$ being the inductance (per square) of the junction electrodes, resulting in $\bar{c} = 0.015c$.

Comparable Fiske step measurements have been performed for sample set SFS64I. The low voltage part of several IVCs of sample SFS64I/0- π at $T = 310$ mK is shown in Fig. 5.12 (a). The magnetic field is varied between $B = -200 \dots +200 \mu\text{T}$. In Fig. 5.12 (b) the dependencies of the maximum current of the Fiske steps on magnetic field are presented. The respective zero-level (offset) of each Fiske step in Fig. 5.12 (b) is

equal to the minimum current value, at which the respective Fiske step starts in Fig. 5.12 (a). Note, that every odd Fiske step is mixed with a half-integer ZFS, thus resulting in a finite step height (above the offset) even for $B = 0$. Our experimental data reproduce theoretical predictions rather well [NSAN06]. The authors of Ref. [NSAN06] used a perturbative scheme to calculate phase dynamics and the resulting resonances appearing on the IVC of Josephson junctions with an arbitrary number of $0-\pi$ singularities. As realized in the samples here, they considered the flat phase regime where no spontaneous flux is present in the ground state of a Josephson junction with finite length. Using the expressions (27) and (28) from Ref. [NSAN06] with the respective parameters of our samples it is possible to compare experiment and theory, see solid lines in Fig. 5.12 (b). The analytical calculations are performed in normalized units and converted to physical units by a fitting procedure: The magnetic field axis is adjusted by matching the first minimum of the $I_m^{0-\pi}(B_y)$ curve of the half-integer ZFS in experiment and theory. This conversion scheme is used for all six measurements. The y -axes are adjusted separately using a similar procedure. A very good agreement between the analytical predictions and the experimental data is found. The spacing of the minima, the height of the maxima as well as the overall shape of the curves are reproduced by theory [NSAN06].

As it was pointed out, each odd step is a mixture of Fiske step and half-integer ZFS. The amplitude $I_m(0)$ of the 3rd step is above the background level due to its ZFS contribution. For the 5th FS, $I_m(0)$ coincides with the background level as the ZFS contribution is vanishing.

5.3.3 Shapiro steps

Shapiro step measurements are carried out for sample set SFS64I, compare Subsec. 1.3.3. We study the question, whether half-integer Shapiro steps are observed for SIFS junctions. Half-integer Shapiro steps are observed with a voltage spacing of $\Delta V = \frac{1}{2}(f\Phi_0)$, as the doubling of the Josephson frequency is a consequence of a $\sin(2\varphi)$ current-phase relation. Thus, the occurrence of half-integer Shapiro steps is embedded in the ongoing discussion about non-sinusoidal current-phase relations in $0-\pi$ junctions, also compare Chap. 4. A 0 to π transition can be achieved in SFS or SIFS junctions as a function of temperature [ROR⁺01] or ferromagnetic barrier thickness [KAL⁺02]. Close to the $0-\pi$ transition the first order Josephson supercurrent vanishes, so the observation of a $\sin(2\varphi)$ component seems possible in the transition region. Half-integer

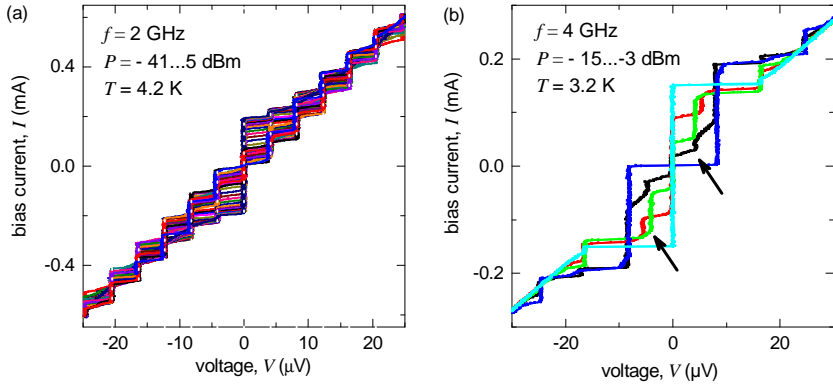


Figure 5.13: (a) Shapiro steps measured for junction SFS64I/0 at $T = 4.2$ K (overdamped regime). Microwaves are applied with a frequency of $f = 2$ GHz. (b) Experimental data of Shapiro step measurements of the same junction at $T = 3.2$ K (underdamped regime). Half-integer Shapiro steps are visible and marked by arrows.

Shapiro steps have been reported for SFS junctions in the vicinity of the minimum of I_c [SBLC04]. The authors attributed these steps to the $\sin(2\varphi)$ component. In other experiments [FVHB⁺06] half-integer Shapiro steps are explained with a non-uniform critical current density, without the need of an intrinsic $\sin(2\varphi)$ component. Thus, the conclusive explanation of the origin of half-integer Shapiro steps is still an open problem.

IVCs of sample set SFS64I are measured at different temperatures in the presence of applied microwaves. As an example, Shapiro step measurements for sample SFS64I/0 at $T = 4.2$ K and $T = 3.2$ K are shown in Fig. 5.13. Microwave frequencies of $f = 2$ GHz and $f = 4$ GHz are applied. In both cases resonant steps which fulfill the condition $\Delta V = f\Phi_0$ ($4.1 \mu\text{V}$ and $8.3 \mu\text{V}$, respectively) are observed. Additionally, half-integer Shapiro steps are detected which have a voltage spacing of $\Delta V = \frac{1}{2}(f\Phi_0)$. They are weakly pronounced and hardly visible for $f = 2$ GHz at $T = 4.2$ K. At $T = 4.2$ K the junction is in the overdamped regime. These experimental conditions are chosen to avoid chaotic dynamics. With transition to the underdamped regime and increasing frequency the half-integer Shapiro steps become more pronounced, see Fig. 5.13 (b).

In order to examine whether our half-integer Shapiro steps are due to

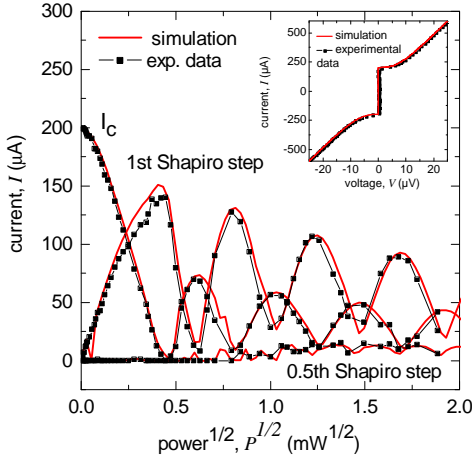


Figure 5.14: Dependence of the height of the 0th ($=I_c$), 1st and 0.5th Shapiro step on the applied microwave power. Experimental data and simulations are compared. Simulations are performed without taking the $\sin(2\varphi)$ component into account. Inset: Comparison between experimentally observed IVC and according to the RCSJ-model simulated curve. (sample: SFS64I/0 at $T = 4.2$ K, $f = 2$ GHz, $I_c = 202.8 \mu\text{A}$, $\beta_c = 0.8$)

a non sinusoidal current-phase relation, Shapiro step measurements for different excitation amplitudes are carried out. As an example, the experimental parameters I_c and R of sample SFS64I/0 at $T = 4.2$ K are obtained from experiment and are used for simulations. Current-voltage characteristics can be simulated according to the RCSJ-model¹¹, see inset of Fig. 5.14. A current-phase-relation is used with an additional $\sin(2\varphi)$ term, which can be weighted by a factor of ϵ . Shapiro steps are measured in experiment by radiating microwaves with a frequency of $f = 2$ GHz. As a first try simulations are performed without taking the $\sin(2\varphi)$ component into account ($\epsilon = 0$). In Fig. 5.14 the heights of the 0th, 1st and 0.5th Shapiro step are shown as a function of microwave power, both for numerics and experiment. For all three curves, the same x -axis scaling is used. One can see a perfect quantitative agreement between numerical simulations and experimental data. Although the $\sin(2\varphi)$ component is not taken into account, the half-integer Shapiro

¹¹The respective software was written by Prof. Dr. Reinhold Kleiner.

step appears in the simulations and reproduces the experimental data perfectly well. This is a result of a finite capacitance, *i.e.*, $\beta_c \neq 0$.

The simulations are repeated taking the $\sin(2\varphi)$ component into account (data not shown). As long as the second harmonic is small ($\epsilon \leq 0.1$), the experimental data are reproduced by the numerical simulations. As soon as the second harmonic contribution is higher than $\epsilon > 0.1$, the simulations deviate significantly from the experimental data. These data confirm the assumption, that the half-integer Shapiro steps are not due to a $\sin(2\varphi)$ contribution. Half-integer Shapiro steps are also observed for the samples SFS64I/ π and SFS64I/ $0-\pi$ (data not shown). The experimental data are reproduced in simulations without the need of a $\sin(2\varphi)$ component, too.

5.4 Dynamic properties of long $0-\pi$ SIFS junctions

5.4.1 Experimental data

In Fig. 5.15 experimental data of IV characteristics of sample SINFS-F11-lg/ $0-\pi$ at $T = 3.5$ K and 3.3 K are shown. Measurements are obtained in the same state as presented in Fig. 5.4. Here, the respective $I_c(B)$ pattern of junction SINFS-F11-lg/ $0-\pi$ reveals a strong offset from zero magnetic field. To study ZFSs as well as Fiske steps, experimental

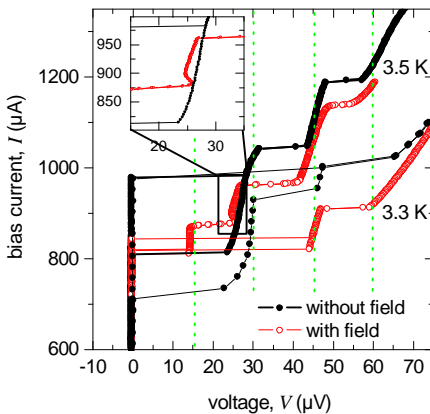


Figure 5.15: Experimental data of IV characteristics of sample SINFS-F11-lg/ $0-\pi$ at $T = 3.5$ K, and 3.3 K. The measurements are taken in the minimum (red open dots) and left maximum (black filled dots) of the $I_c(B)$ pattern. The Fiske step voltage position with a voltage spacing of $\Delta V = 15 \mu\text{V}$ is indicated as green dashed lines. Inset: Enlargement of IVCs at $T = 3.5$ K.

data were obtained in the minimum of the $I_c(B)$ pattern with applied magnetic field (red open dots), and in the left maximum without applying magnetic field (black filled dots)¹². The Fiske step voltage spacing $\Delta V = 15 \mu\text{V}$ is indicated as dashed green lines. With applied magnetic field (in the minimum of the $I_c(B)$ pattern), the 0.5th ZFS, the 1st ZFS and the 1.5th ZFS are observed. This is in contrast to short $0-\pi$ junctions, where only the 0.5th ZFS and the 1.5th ZFS are observed in zero field. Integer and half-integer ZFS are mixed in the long junction SINFS-F11-lg/ $0-\pi$, a behavior which was not observed in short $0-\pi$ junctions. The step of 0.5th order is identified as a hiZFS by measuring $I_m(B)$, the other steps as higher order Fiske steps (data not shown). Measuring IVCs in the left maximum of junction SINFS-F11-lg/ $0-\pi$, a 1st order step and a 1.5th order step are visible. In the inset of Fig. 5.15 an enlargement of the 1st ZFS in the current range between $839 \mu\text{A} < I < 980 \mu\text{A}$ at $T = 3.5 \text{ K}$ is shown. A back-bended substructure is visible. A comparable substructure on a ZFS was measured for another long ($5 \sim l$) $0-\pi$ junction of chip SINFS-F11-lg in experiment, but not for the respective reference junctions.

5.4.2 Numerical analysis

To gain a deeper insight into the properties of ZFS in long $0-\pi$ junctions, simulations are performed without applying magnetic field¹³. In contrast to short and intermediate $0-\pi$ junctions, in long $0-\pi$ junctions the appearance of integer and half-integer ZFS in the absence of magnetic field crucially depends on the junction length. If the junction length is very long (*e.g.* $l > 8$), half-integer and integer ZFS are observable at the same time *without* applied magnetic field. In Fig. 5.16 a numerically simulated IVC of a $0-\pi$ junction with length $l = 5$, $\alpha = 0.1$ is shown. The parameters are comparable to the experimental parameters of junction SINFS-F11-lg/ $0-\pi$ shown in the last subsection. Here, two half-integer ZFS ($n = 1.5, 2.5$) are visible (the 0.5th ZFS is suppressed). No Fiske steps or integer ZFS are observed without applied magnetic field.

In Fig. 5.16 the 1.5th ZFS has a very pronounced, back-bended substructure between $0.15 < i < 0.20$ – which looks very similar to the back-bended structure which was observed in experiment for sample SINFS-F11-lg/ $0-\pi$, compare Fig. 5.15. On the 2.5th ZFS in Fig. 5.16

¹²We remind the reader of the discussion of ZFS as steps in zero field of the sample's own magnetic field.

¹³The software SKJJ32.EXE [Skj09] is used.

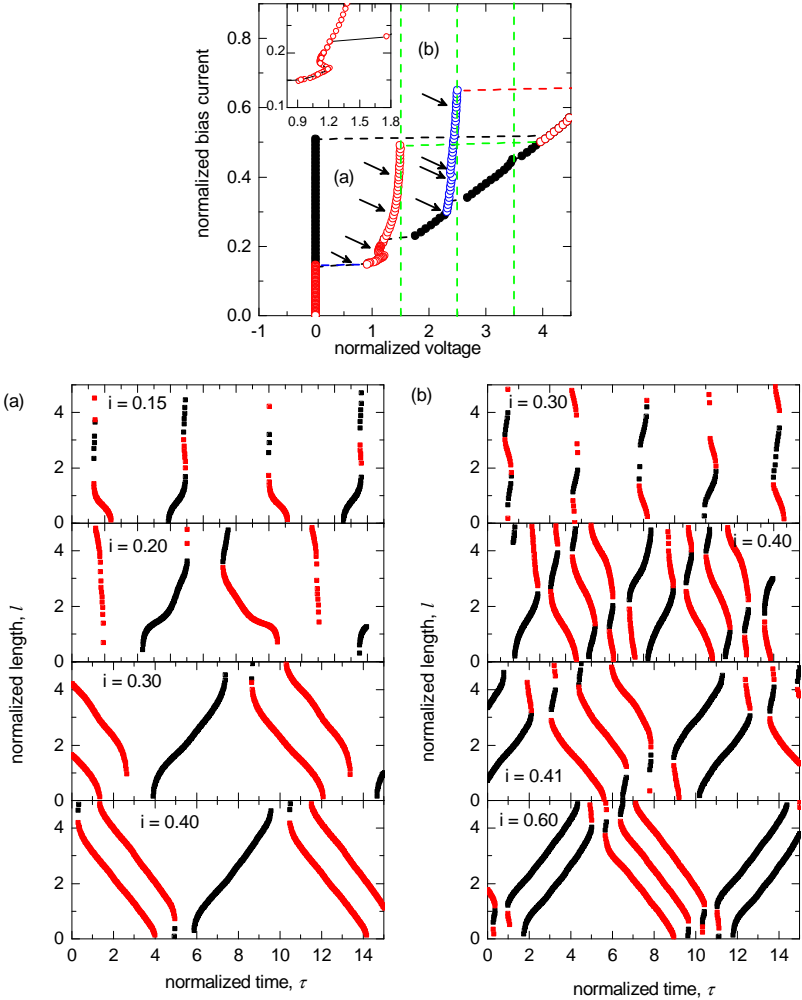


Figure 5.16: Simulated IVC of a long $0-\pi$ junction ($l = 5$, $\alpha = 0.1$) with 1.5th ZFS (red open dots) and 2.5th ZFS (blue open dots). The zero voltage branch is calculated separately (black dots). Inset: Enlargement of knee-region of the 1.5th ZFS. (a) Trajectories of semifluxons (black squares) and antisemifluxons (red) at $i = 0.15, 0.20, 0.30, 0.40$ on the 1.5th ZFS. (b) Trajectories on the 2.5th ZFS at $i = 0.30, 0.40, 0.41, 0.60$.

there is a very small substructure between $0.40 < i < 0.41$. These sub-steps, or satellite steps, emerge starting¹⁴ from an intermediate length $l > 2$. To identify the dynamics, several trajectories of semifluxons on both steps are shown in Fig. 5.16. In (a), the trajectories at different current positions on the 1.5th ZFS are plotted. At $i = 0.15$ the motion is standing-wave-like, with almost equal distance between the moving centers of the semifluxons/antifluxons. On the knee-region at $i = 0.20$ the movement is totally distorted. At $i = 0.30$ and $i = 0.40$ the states show a broken symmetry, one center of a semifluxon moves forward, and two antifluxons move backward. This exactly corresponds to $n = 3/2$. The two antifluxons bunch and move in a group (1 antifluxon). Thus, in this presentation one fluxon is depicted as a motion of two semifluxons with equal polarity. On the 2.5th ZFS the behavior is similar, see Fig. 5.16 (b). First ($i = 0.30$), there is a kind of standing-wave-like motion. Around the knee-structure ($0.40 < i < 0.41$) the situation changes. The motion converts into a bunched, broken symmetry state, with two semifluxons (1 fluxon) and three antifluxons (here it is not possible to tell which pair of the three lines corresponds to the antifluxon), $n = 5/2$. Thus, in contrast to short $0-\pi$ junctions with plain half-integer ZFS, in long $0-\pi$ junctions the dynamics change on each half-integer ZFS: the mode changes from a Fiske-step-like mode at the bottom of the step to a bunched semifluxon mode at its top. We might have observed the change between a Fiske-step-like mode and bunched-motion modes on *one* ZFS in experiment, where back-bending is observed.

Overall, there is a qualitative agreement between numerics and experiment: The general shape of the ZFS as well as the substructures, which are seen in experiment, are reproduced in numerics. Interestingly, the satellite steps occur without applied magnetic field in numerics; in experiment they are observed in the central minimum of the $I_c(B)$ pattern. There are quantitative discrepancies: the step number and order is not the same. The first observable step in experiment is the hiZFS, in numerics it is the 1.5th ZFS. This might be due to the fact that in the experiment presented here, there is no clear definition of *without* and *with* magnetic field. Additional to the discussed offset from zero magnetic field due to a remanent magnetization of the F-layer, there is a non-vanishing component of the magnetic field which is due to the bias current (self-field effect). Thus it is not surprising that in the experiments presented here, there is a mixture of steps (integer, half-integer

¹⁴Calculations were performed by Dr. E. Goldobin, not published yet.

ZFS, Fiske steps). Additionally, the F-layer might encourage configurations which are not considered in the simple sine-Gordon simulations presented above.

5.5 Conclusions

In this chapter the results of detailed experimental and numerical studies on the *static* and *dynamic* properties of 0 , π and $0-\pi$ SIFS Josephson junctions were presented. Four sets of samples were used: chip SFS64I (short, linear samples), chip JJF16 (intermediate length, linear samples), chip SINFS-F11-lg (long length, linear samples), chip AJJ19-H-sm (intermediate length, annular samples). All samples were underdamped at sufficiently low temperatures below $T = 4.2$ K. Depending on the experimental parameters Fiske steps, zero field steps and Shapiro steps were observed on the IV characteristics. The dynamic properties of 0 and π SIFS junctions are, as expected, quantitatively similar to standard SIS junctions. Concerning the static properties, there are differences between SIFS and SIS junctions. The offset from zero magnetic field in the $I_c(B)$ dependencies as well as bumped minima and asymmetric maxima often happen for SIFS junctions.

An $I_c^{0-\pi}(B_x, B_y)$ dependence of a short $0-\pi$ junction revealed a clear fingerprint of the $0-\pi$ boundary: the central minimum around zero field. The differences between the $I_c(B)$ pattern of short and long $0-\pi$ junctions were studied in detail. For long $0-\pi$ junctions complicated, metastable fluxon/semifluxon configurations were verified in experiment. Numerical simulations support the data analysis.

Half-integer Shapiro steps were observed on the current-voltage characteristics of 0 , π and $0-\pi$ Josephson junctions. This does not necessarily imply the presence of the second harmonic in the current-phase relation, but may be present due to the finite capacitance of the Josephson junctions. The analysis of a short overdamped Josephson junction in the framework of the RSJ model, confirmed this picture.

Half-integer zero field steps were found on the IV characteristics of short $0-\pi$ Josephson junctions. The step current dependencies for several Fiske and zero field steps were measured experimentally and the results were analyzed analytically. To our knowledge, this is the first time when a half-integer zero field step is reported for “natural” $0-\pi$ Josephson junctions, as opposed to “artificial” $0-\pi$ Josephson junctions with current injectors [GSG⁺04]. The dynamics of the phase or the flux on the half-

inter ZFS in short junctions were identified by simulating the trajectories of the semifluxon. Comparable measurements of long $0-\pi$ junctions revealed complicated substructures (satellite steps) on the ZFS in experiment and in numerics. At these substructures the system changes between a Fiske-step-like motion and a bunched mode. The satellite steps were only observed for $0-\pi$ junctions, but not for the respective reference junctions.

Chapter 6

Escape of the Josephson phase in SIFS junctions: From thermal to quantum regime

In this chapter we study phase escape mechanisms in SIFS Josephson junctions. $0-\pi$ junctions as well as the respective reference junctions in the short and intermediate limit are considered. The measurement setups and measurement techniques are briefly described. In Sec. 6.2 magnetic field dependencies of thermal excitations of samples in the short junction limit are measured, around $T \sim 200$ mK, and compared with numerics. Simulations of the activation energy which take the j_c -asymmetry of the $0-\pi$ junction into account are compared with experimental data. The results of escape rate measurements at temperatures between 0.5 K down to 25 mK are shown. The data are analyzed in the framework of thermal activation theory of a pointlike Josephson junction. Different methods to take damping into account are applied. In Sec. 6.3 resonant activation is experimentally studied. Using microwave spectroscopy, the eigenfrequencies of 0 , π , and $0-\pi$ Josephson junctions (short and intermediate length) at temperatures around $T \sim 350$ mK are investigated. Harmonic, subharmonic and superharmonic pumping is observed in experiment and the experimental data are compared with numerical simulations. The last section of this chapter summarizes its

id	j_c (A/cm ²)	l	L (μm)	W (μm)	W_i (μm)
SINFS-13H-sm/0	50.4	0.69	50	10	5
SINFS-13H-sm/ π	40.0	0.61	50	10	5
SINFS-13H-sm/0- π	48.3	0.68	50	10	5

Table 6.1: Parameters of sample set SINFS-13H-sm. The critical current densities are measured at $T = 200$ mK. L is the physical length of the junction, l is the normalized length. W is the width of the junction, W_i is the width of the idle region in physical units. Notations are chosen according to Ref. [MCM95].

main results¹.

With these studies we contribute to the very current, ongoing discussions on the quantum properties of SIFS Josephson junctions. We discuss the possibility that SIFS junctions exhibit additional noise contributions in contrast to SIS junctions. This additional noise might be due to the F-layer. We comment on the applicability of SIFS junctions as parts of quantum circuits. Additionally, we address the question how finite length effects and the presence of phase shifts change the effective barrier height and the phase escape mechanisms in comparison to the simple pointlike junction model.

6.1 Samples and measurement techniques

Thermal activation experiments are performed using a junction triplet located on chip SINFS-13H-sm (short limit). The sample parameters are given in Tab. 6.1. The spectroscopy data are obtained using sample set SFS64I (short limit) and JF16 (intermediate length). The last two sets were characterized in Chap. 5. All samples are linear, designed in overlap geometry. Again, by decreasing the temperature below $T < 4.2$ K all junctions could be driven from the overdamped to the underdamped limit.

The phase escape measurements and spectroscopy measurements were carried out in (a) a standard ³He cryostat (actually the same as used in Chap. 5) (Oxford Instruments, Heliox) and (b) a dilution refrigerator (self-made at the WMI Garching, Munich). Using the ³He cryostat, tem-

¹I particularly thank Dr. Tobias Gaber for his help with the experiments and data analysis presented in this chapter.

peratures between 1.9 K and 310 mK are accessible, the dilution refrigerator has a base temperature of about 25 mK. In both setups, cryoperm shields are placed around the sample to shield it from the earth magnetic field and stray fields. In the ^3He setup as well as the dilution refrigerator a homogeneous external magnetic field can be applied in-plane of the junctions in a controlled way. In this chapter, the external magnetic field is always applied parallel to the step in the ferromagnetic layer. As the samples are very sensitive to residual magnetic fields, special care has been taken to ensure a parasitic-flux-free state. Especially in the dilution refrigerator, a series of filter stages is used for both the bias current and the voltage sensing lines. At different temperature stages commercial feed-through filters, RC filters and custom-made copper powder filters are used [Lis08; LU08].

The escape of the Josephson phase is investigated by measuring switching current statistics with a time-domain technique [FD74], as introduced in Subsec. 3.2.1. In brief, the sample is current biased by a custom-made low-noise battery-powered current source. The bias current is ramped up starting from a small negative offset and is ramped at a constant rate \dot{I} . If the current passes $I = 0$, the measurement is started ($t = 0$). At the time t_{sw} , which is measured using a counter with a 20 GHz stabilized clock (Stanford Research Systems, SR620), the voltage detector detects that the junction switches to a finite voltage state. Each switching event is detected by feeding the preamplified voltage signal from the sample to a custom-made trigger circuit with adjustable threshold. The switching current I_{sw} is calculated as $I_{\text{sw}} = \dot{I} \times t_{\text{sw}}$. The switching current probability distribution $P(I_{\text{sw}})$ is found by accumulating a large number ($\sim 10^4$) of measurements of I_{sw} and generating a histogram. The standard deviation σ of $P(I_{\text{sw}})$ is further evaluated as a function of temperature. At least in the short junction limit [FD74; JGH⁺81; Gar95] a scaling of $\sigma \sim I_{\text{sw}}^{1/3}$ is expected, thus for sake of comparison $\sigma^*(T) = \sigma/I_{\text{sw}}^{1/3}$ is sometimes plotted in reduced units².

To determine the eigenfrequencies of the junctions spectroscopy measurements were performed. For this purpose, microwaves (Rhode und Schwarz, SMR40) in the frequency range between 1 and 15 GHz are applied to the junctions by placing an antenna above the sample. The microwave power (at the output of the source) was varied in the range of $-100 \dots 20$ dBm. A detailed description of the setups and measurement techniques is published elsewhere [WDLU03; WLC⁺03; Gab07; Lis08].

²Note, σ^* still weakly depends on the relative ramp rate \dot{I}/I_{sw} .

6.2 Escape rate measurements of short SIFS Josephson junctions

Preface

During the last years there was a growing interest among different groups to characterize SIFS junctions in the quantum regime. K. Madek *et al.* [MBW⁺06] examined short π junctions (Nb/Al-Al₂O₃/Ni₆₀Cu₄₀/Nb technology) produced by M. Weides. The authors were the first to report on escape rate and on resonant activation measurements of a π SIFS junction down to $T = 20$ mK. Interestingly, they observed a saturation of the standard deviation slightly below $T \sim 100$ mK, which is much higher than the crossover temperature expected from pointlike junction theory. Their results were not published up to now, but were presented during several conferences [MBW⁺06].

Independently, almost at the same time (beginning of 2007) we started escape rate and resonant activation measurements on the 0 , π and $0-\pi$ junctions on chip JJF16. Our main advantage at this time (and still on) was that we were (are) the only group having working *triplets* for their studies. Thus our main interest — besides the characterization of SIFS junctions in the quantum regime — was to study the *differences* between the quantum properties of a $0-\pi$ SIFS junction *and its* SIFS reference junctions. At this time, we did not have a working triplet in the short length limit. The at this time available junction triplet JJF16 is of intermediate length. We were aware of the fact that the intermediate length of these samples could complicate data analysis and their interpretation. The most surprising results of our experiments in 2007 and 2008 were, that the JJF16/ 0 and the JJF16/ $0-\pi$ junctions showed very high crossover temperatures ($T = 120\dots150$ mK)³, comparable to the crossover temperature observed in [MBW⁺06]. These crossover temperatures could not be interpreted in the framework of the pointlike junction model, compare Eq. (3.22). The measured saturation temperatures were at least one order of magnitude higher than expected. We interpreted the saturation of the standard deviation as due to additional spin noise in the F-layer and concluded that the crossover to the quantum regime in SIFS junctions might be strongly influenced by the quantum fluctuations in the ferromagnetic layer. Additionally, in our experiments we observed an enhanced $\sigma(T)^*$ dependence of the $0-\pi$ junction in compar-

³The JJF16/ π junction could not be measured due to technical problems.

ison with its reference junctions. We interpreted this additional noise as a fingerprint of the semifluxon, a phenomenon which is known for SIS junctions with injectors [KGB⁺09a].

At the beginning of 2009 M. Aprili and his coworkers [PA09] published results on escape rate measurements of a π junction (Nb/Al-Al₂O₃/Ni₁₀Pd₉₀/Nb technology) down to $T = 350$ mK. In contrast to our findings and the results from K. Madek *et al.*, the authors did not find any evidence for additional noise, especially not for excess spin noise which is due to the presence of the F-layer. Although their experiments only consider the thermal regime of π junctions, their findings raised reasonable doubts on our results, in particular as we could not fully interpret our experimental data. Thus, intensive numerical studies were initiated in our group⁴.

The main results of these numerical studies concern $0-\pi$ junctions: If one takes into account the asymmetry of the critical current densities in the 0 and π part of a SIFS $0-\pi$ junction, the fingerprint of the semifluxon is often hidden by the asymmetry effects on the standard deviation⁵ σ . If we want to see a fingerprint of the semifluxons in experiments, we will have to bias a long, preferably not too asymmetric $0-\pi$ junction at magnetic fields around the central minimum of the $I_c(B)$ pattern. The influence of the semifluxon is strongest around the minimum; it vanishes around the maxima.

In contrast to other systems, *e.g.*, artificial $0-\pi$ junctions with injectors, our systems combine several difficulties during data analysis: First, we deal with SIFS junctions. Up to now it is not totally clear, whether there is an influence of the F-layer on phase escape mechanisms. Second, we examine $0-\pi$ junctions with a j_c asymmetry, typically $j_c^\pi \neq j_c^0$. This asymmetry, in turn, influences the effective barrier height. Third, the phase shift of the $0-\pi$ junction itself changes phase escape mechanisms. Forth, due to the limited number of samples we sometimes deal with intermediate length samples; their length effects additionally complicate data analysis. After the ineffective (because hardly interpretable) experiments on the quantum properties of the JJF16 junctions we broke down the problems into several pieces. In the following, to make the system as controllable as possible and data analysis as simple as possible, we re-

⁴These numerical studies were mainly performed by Dr. T. Gaber.

⁵In particular, for the j_c asymmetry of junction JJF16/ $0-\pi$, numerical simulations showed, that any consequence due to the presence of the semifluxon is strongly reduced compared to the symmetric case. Thus our interpretation of the enhanced $\sigma(T)^*$ dependence of the $0-\pi$ junction as being a fingerprint of the semifluxon was wrong.

strict ourselves to junctions in the short limit. With our new knowledge we start escape rate measurements with (now available) new samples, located on chip SINFS-H13-sm (short length limit). As motivated in the last chapter, we study phase escape mechanisms of the reference junctions in detail. Then, we examine the influence of the $0-\pi$ boundary on the phase dynamics; the experimental data are compared with numerical simulations which take the j_c -asymmetry into account.

6.2.1 Phase escape in magnetic field

In this subsection switching current measurements of samples SINFS-13H-sm/0, SINFS-13H-sm/ π and SINFS-13H-sm/ $0-\pi$ are presented as a function of magnetic field. We examine the magnetic field dependence of thermal excitations before examining switching current measurements at different temperatures, because we want to characterize the state of the junctions via $I_c(B)$ measurements first. Doing so, we guarantee a flux-free state of the samples. Additionally, $\sigma(B)$ measurements help us to identify interesting points of the $I_c(B)$ curve, at which, *e.g.*, a fingerprint of the semifluxon is observable. At these points, switching current measurements at different temperatures should be performed.

Each probability distribution $P(I_{sw})$ of switching currents is obtained by recording 10^4 individual switching events. The bias current is ramped at a rate of $\dot{I} = 0.0199$ A/s. The measurements are performed at $T = 200$ mK or $T = 300$ mK. The magnetic field is always swept from negative to positive field values. The experimental data are obtained using a custom-made LABVIEW data acquisition software and analyzed using a custom-made MATLAB analysis software⁶. The method for data analysis was described in Subsec. 3.2.1, it basically performs an iterative regression scheme to fit $\ln(2\pi\Gamma_i/a\omega_0(I_i))^{2/3}$. The escape temperature T_{esc} and the fluctuation-free critical current $I_{c,0}$ are obtained as fitting parameters⁷. In this subsection damping is not considered, $a_{TST} = 1$.

In Fig. 6.1 experimental data of escape rate measurements and their dependence on magnetic field is shown. On the left side of Fig. 6.1, the mean switching current vs. magnetic field of all three junctions is plotted. The reference junctions exhibit a regular Fraunhofer pattern, there is no substantial amount of parasitic flux trapped. The $I_c(B)$ pattern of

⁶The data acquisition software was written by Kai Buckenmaier, the analysis software was written by Dr. Tobias Gaber.

⁷The capacitance per junction area of the SINFS-13H-sm samples (which is needed to estimate ω_P) is obtained from Fiske step measurements as $C \approx 35$ $\mu\text{F}/\text{cm}^2$.

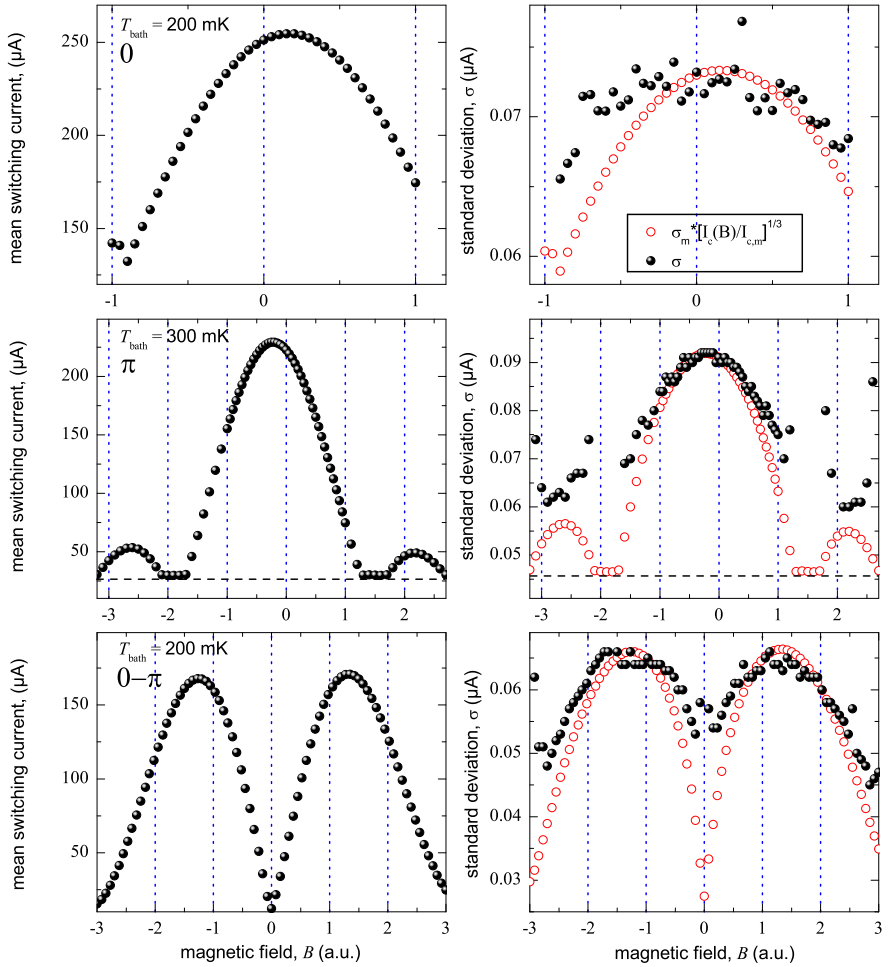


Figure 6.1: Experimental data of switching current measurements of samples SINFS-13H-sm/0, SINFS-13H-sm/ π and SINFS-13H-sm/0- π at $T = 300 \text{ mK}$ and $T = 200 \text{ mK}$, respectively. Left side: mean switching current dependence on magnetic field. Right side: $\sigma(B)$ is compared with the standard deviation of a short junction calculated as $\sigma = \sigma_m * [I_c(B)/I_{c,m}]^{1/3}$, $\sigma_m = \sigma @ I_{c,m}$. The voltage criterion is indicated as a dashed line.

the $0-\pi$ junction agrees pretty well with predictions from theory, compare Sec. 2.3. The $I_c(B)$ dependencies of the reference junctions are not centered around zero magnetic field, but are slightly shifted (presumably) due to a finite magnetization of the F-layer. For sample SINFS-13H-sm/ π the voltage criterion is indicated as a dashed line. On the right side of Fig. 6.1 the dependence of the experimentally obtained standard deviation on magnetic field is shown (black, filled dots). For means of comparison the standard deviation vs. magnetic field of a short junction is drawn (red, open circles). These data are obtained by calculating $\sigma_m * [I_c(B)/I_{c,m}]^{1/3}$. σ_m is the respective value of the standard deviation at $I_{c,m}$, where $I_{c,m}$ is the maximum value of critical current in magnetic field. In this way, the standard deviation is plotted in reduced units (regarding the $I_c^{1/3}$ dependence of the standard deviation), but can be compared with the experimental data of the respective junction. The comparison between experimental data and short junction theory reveals, that the samples SINFS-13H-sm/0, SINFS-13H-sm/ π , and SINFS-13H-sm/ $0-\pi$ are described by the simple short junction model with a good accuracy in the region of the $I_c(B)$ maxima. The dependence of their standard deviation on magnetic field, (mainly) follows the expectations from short junction theory. On the other hand, the limits of our measurement scheme are revealed: Generally, the standard deviation is not decreasing in experiment as it is doing in theory, see *e.g.*, the standard deviation around the central minimum of the $0-\pi$ junction or around the first side minima of the π junction. This is mainly due to resolution restrictions of the measurement scheme, discussed in detail below. It is not due to an additional noise contribution from the coil current.

To gain further insights, numerical simulations are performed to study the effective barrier height of the potential as a function of magnetic field. The simulations are done using the ACTIVLLJJA.EXE software [act09]. The numerical approach follows an ansatz developed by M. G. Castellano *et al.* [CTC⁺96; KGB⁺09b]. As in the case of point contacts, the escape process of a spatially extended junction (with a $0-\pi$ phase shift) requires thermal activation over the potential barrier. The respective barrier height is defined as the difference between the minima solutions and the adjacent saddle solutions/maxima of the potential, $U(\varphi_m) - U(\varphi_0)$, see Sec. 3.1. The static version of the underlying sine-Gordon equation is solved numerically by using a shooting algorithm, in order to determine all possible static solutions.

In Fig. 6.2 (a) a comparison between experimental data and numerics of sample SINFS-13H-sm/ π is shown. The upper part of the figure shows

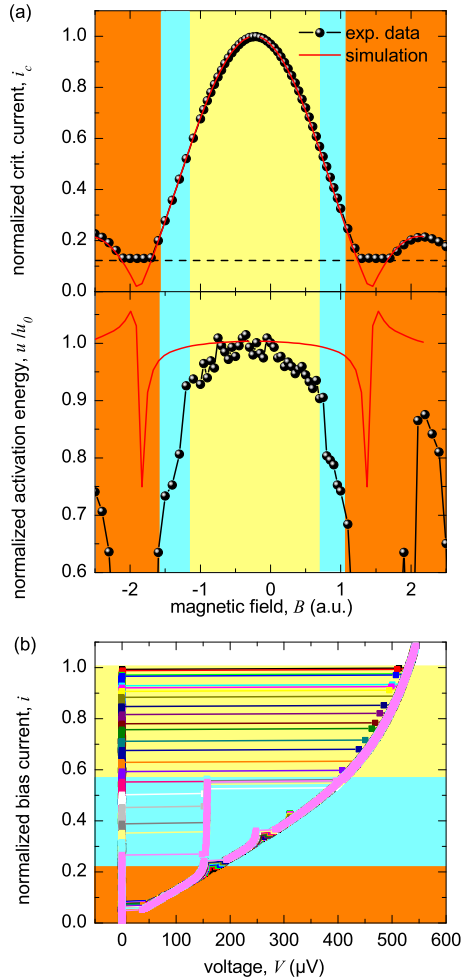


Figure 6.2: (a) Comparison between experimental data (black dots) and simulation (red, solid line, $l = 0.61$) of the critical current and activation energy dependence on magnetic field (SINFS-13H-sm/ π). Three different resolution regimes are distinguished. Yellow: high resolution, blue: intermediate, orange: weak. The voltage criterion is indicated as a dashed line. (b) Series of IVCs showing Fiske steps at $T = 170$ mK.

the mean switching current vs. applied magnetic field. The experimen-

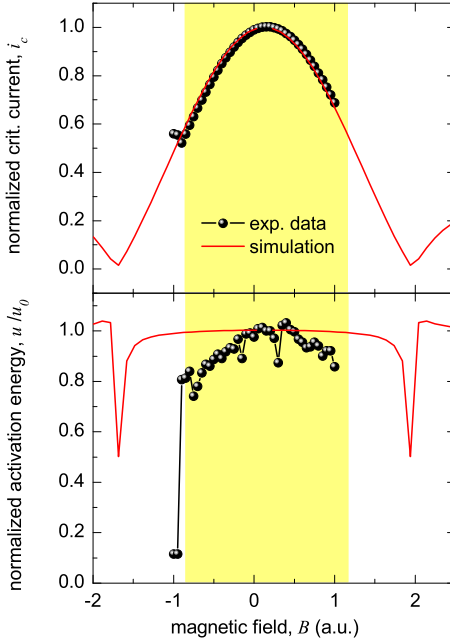


Figure 6.3: Switching current measurements in applied magnetic field (SINFS-13H-sm/0). Black dots: experimental data. Solid, red line: simulation ($l = 0.69$). The high resolution regime is indicated as in Fig. 6.2.

tal data are indicated as black, filled dots, the simulations are shown as a solid, red line. The simulations were done with parameters extracted from measurements of sample SINFS-13H-sm/ π ($l = 0.61$). The experimental data of the mean switching current are normalized to its maximum value, likewise the simulated values. The numerically calculated curves are shifted along the magnetic field axis to match with the experimental data. The magnetic field axes of numerics is scaled such that the side minima coincide with experiment. The agreement between the experimentally obtained $I_c(B)$ dependence and numerics is excellent. In the lower part of Fig. 6.2 (a) the activation energy of the sample is analyzed. The normalized activation energy u/u_0 can be calculated from the experimentally observed escape temperature in comparison with the bath temperature

$$u/u_0 = T_{\text{bath}}/T_{\text{esc}}. \quad (6.1)$$

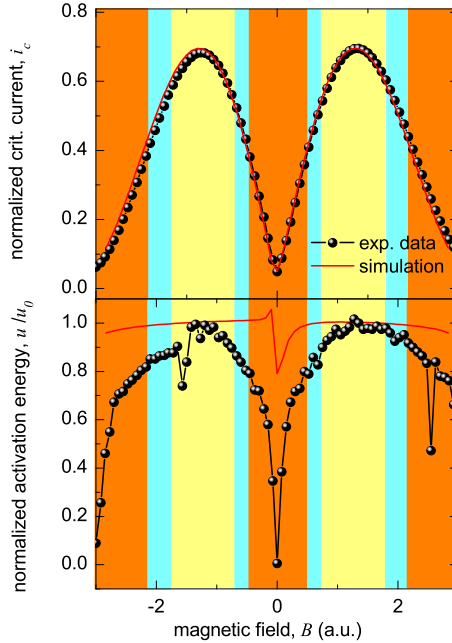


Figure 6.4: Switching current measurements in applied magnetic field (SINFS-13H-sm/0- π). Black dots: experimental data. Solid, red line: simulation ($l = 0.68$). Three different resolution regimes are distinguished as in Fig. 6.2.

$u_0 = \Delta U/E_J$ is the activation energy of a pointlike junction as a function of magnetic field, u is the activation energy of the junction under examination. The magnetic field axes scaling is taken from the $I_c(B)$ dependencies. Three different regions are indicated in Fig. 6.2. They correspond to different regimes of experimentally achievable I_c resolution. The resolution of the critical current determination (and the out-of-it calculated parameters) is proportional [WLC⁺03] to

$$\delta t_{\text{stop}} \sim 1/\Delta V, \quad (6.2)$$

δt_{stop} are the variations in the stop signal; ΔV is determined by switching the junction from its zero voltage state to the resistive state. Thus δt_{stop} depends on the voltage jump. The higher the voltage jump to the resistive state, the lower is δt_{stop} , *i.e.*, the higher the resolution of the measurement. For means of illustration, Fiske step measurements

at comparable temperatures ($T = 170$ mK) are shown in Fig. 6.2 (b). To facilitate the comparison with Fig. 6.2 (a), the bias current is plotted in normalized units. Within the yellow marked region, the junction switches from the zero voltage state to the subgap branch. The yellow regime indicates the best experimental resolution which can be obtained with our measurement scheme. At higher magnetic field values (blue region) the junction does not switch to the subgap branch, but to the first Fiske step. This voltage jump is much lower, thus the resolution of our measurement is reduced. Within the orange region our measurement scheme is hardly applicable, the critical currents and the voltage jump is rather small. Thus, the resolution is pretty poor.

Comparing experimental data and numerical simulations of the activation energy, the experimental data of sample SINFS-13H-sm/ π are reproduced fairly well by the simulated graph of the short junction theory, see Fig. 6.2 (a). As expected from short junction theory, in the yellow regime, the normalized activation energy/escape temperature hardly depends on magnetic field. The drastic reduction of resolution (which is equivalent to an enhanced noise contribution), is clearly visible in the experimental data of sample SINFS-13H-sm/ π : At the borders of the yellow regime, when the junction switches to the first Fiske step, there is an abrupt decrease of normalized activation energy. Comparable measurements of the activation energy in the presence of applied magnetic field are shown for samples SINFS-13H-sm/0 and SINFS-13H-sm/0- π , see Figs. 6.3 and 6.4. The different resolution regimes for samples SINFS-13H-sm/0 and SINFS-13H-sm/0- π were determined analogously from respective Fiske step measurements (data not shown). The overall behavior is similar to the one of the π junction: Inside the yellow region the normalized activation energy determined in experiment coincides pretty well with numerics for both samples, SINFS-13H-sm/0 and SINFS-13H-sm/0- π . At the boarders of the yellow regime of junction SINFS-13H-sm/0, an abrupt reduction of resolution is observable. Concerning junction SINFS-13H-sm/0- π , in numerics (calculated for $l = 0.68$), there is a small, extraordinary feature visible around zero magnetic field: a kink-like structure which occurs due to the 0- π boundary. Unfortunately, this feature is not observed in experiment, as it is hidden in the region of poor experimental resolution.

We conclude, that the dependence of the effective barrier height of short 0, π and 0- π junctions can be interpreted in the framework of thermal activation theory of a short junction. Within regions of high resolution (yellow), numerics of short junctions reproduce our experimental data

fairly well. But even inside the yellow regimes, for all three junction types, the activation energy vs. magnetic field dependencies decrease a bit too fast in comparison with simulations. To study this behavior correctly, the dependence of the experimental resolution (*i.e.* the voltage jump) on applied magnetic field should be taken into consideration. To improve the data analysis, Dr. T. Gaber included an additional noise term into the simulations which considers the voltage jump vs. critical current dependence to be linear ($\Delta V = \text{const} \times I_c$) [Gab09]. These new simulations show an excellent quantitative agreement with our experimental results. In contrast to standard SIS junctions these corrections are necessary due to the low I_c and R values of SIFS samples, leading to poor experimental resolution. Even in the underdamped limit, for SIFS junctions there is no sudden jump to the gap region; the subgap branch shows a linear behavior with relatively small subgap resistances.

6.2.2 Phase escape at different temperatures

In this subsection switching current measurements of samples SINFS-13H-sm/0, SINFS-13H-sm/ π and SINFS-13H-sm/ $0-\pi$ are presented at different temperatures. Again, for each switching current histogram 10^4 individual measurements are collected, the ramp rate is $\dot{I} = 0.0199$ A/s. The temperature is varied between base temperature $T \sim 25$ mK and $T = 500$ mK. The experimental data of the reference junctions are obtained without externally applied magnetic field. Switching current measurements of the $0-\pi$ junction are performed in both maxima of the $I_c(B)$ pattern, thus during these measurements magnetic field is applied. Comparable measurements are not possible near the central minimum (where the influence of the semifluxon is strongest), as in this region the experimental resolution of the measurement scheme is too low. The junctions are measured in the same states as presented in the last subsection. Thus, no substantial amount of parasitic flux was trapped in the samples during measurements. In this subsection, a custom-made MATLAB analysis software is used which provides several models to take different damping regimes into account, compare Subsec. 3.2.1. In contrast to the data analysis method described in Subsec. 3.2.1 which performs an iterative regression scheme to fit $\ln(2\pi\Gamma_i/a\omega_0(I_i))^{2/3}$ and was used in the last subsection, here, the switching probability distribution is fitted directly with a least square fit. Using Eq. (3.15), a probability distribution $P_i(I_{c,0}, R, T)$ can be calculated which is compared with the experimentally measured probability distribution. The quality of the fit

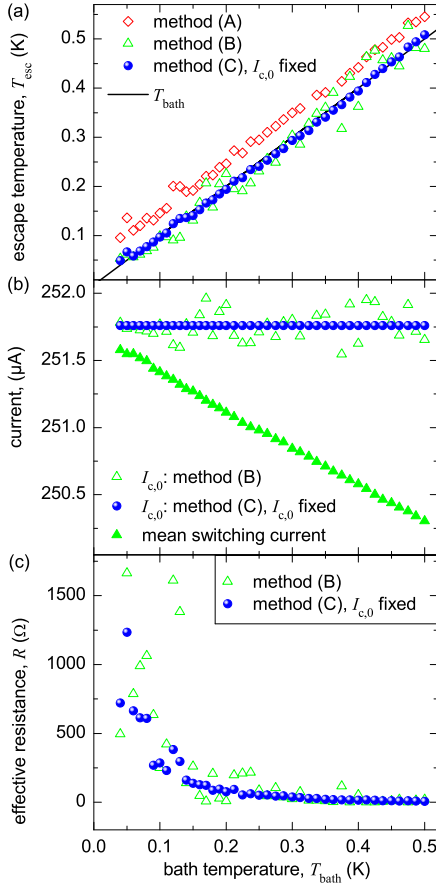


Figure 6.5: Experimental data of switching current measurements (sample SINFS-13H-sm/0). In (a) T_{esc} vs. T_{bath} is plotted, in (b) $I_{c,0}$ and the mean switching current vs. T_{bath} , in (c) the respective effective resistances vs. T_{bath} . Three models are used for data analysis. Method (A): no damping, method (B): intermediate damping, $I_{c,0}$ and R are free fitting parameters, method (C): $I_{c,0}$ is fixed.

is controlled by applying a χ^2 -test.

First, phase escape measurements of junction SINFS-13H-sm/0 are performed. The histogram width becomes more narrow when the temperature is decreased (data not shown) as the thermal fluctuations decline.

The standard deviation decreases with temperature as it is expected in the thermal regime (data not shown). In the temperature range between $T = 25 \dots 500$ mK there is no saturation of the standard deviation visible. Fig. 6.5 (a) shows the escape temperature (analyzed with three different methods) plotted vs. bath temperature (solid, black line). The escape temperature monotonically decreases with decreasing bath temperature. Method (A) is evaluated taking no damping into account, $a_{\text{TST}} = 1$ (red, open squares). Here, T_{esc} is systematically higher than T_{bath} by $\sim 50 \dots 60$ mK. Method (B) takes damping into account, an intermediate damping fitting routine is applied. As a first try (green, open triangles), the fluctuation-free critical current $I_{c,0}$ as well as the effective resistance R are used as free fitting parameters. As visible in Fig. 6.5 (a), with this method the escape temperature is comparable to the bath temperature. Unfortunately, it scatters rather strongly around the bath temperature. Taking a closer look, see Fig. 6.5 (b), reveals that $I_{c,0}$ for method (B) is nearly constant, its distribution is rather small ($\Delta I/I_{c,0} = 0.19\%$). Method (C) uses the same fitting routine as method (B). The only difference between both is, that in method (C) $I_{c,0}$ is fixed and is replaced by its mean value which was calculated in method (B), indicated in Fig. 6.5 (b) as solid, blue dots. Reducing the number of fit parameters, improves the evaluation of the escape temperature drastically, see Fig. 6.5 (a). Using method (C), the theoretically predicted escape temperatures coincide with the bath temperatures, the agreement is excellent⁸. The mean switching current, shown in Fig. 6.5 (b), decreases monotonically with increasing temperature, as expected. In Fig. 6.5 (c) the effective resistance for method (B) (green, open triangles) and method (C) (blue, solid dots) is plotted. For method (B) as well as method (C), the effective resistance R exhibits a clearly decaying behavior, it seems to decrease exponentially. For higher temperatures $T > 100 \dots 200$ mK the effective resistance is fitted with a few ohms. For means of comparison, the subgap resistance R_s which was determined by IV measurements is around $\sim 3 \Omega$. Below 100 mK, the resistance increases by at least one order in magnitude. We only use an intermediate damping regime routine for data analysis.

Comparable switching current measurements and data analysis are performed for sample SINFS-13H-sm/ π and sample SINFS-13H-sm/0- π , see Figs. 6.6 and 6.7. The results are quantitatively similar. Without damping (A) the escape temperatures show an $\sim 50 \dots 70$ mK offset

⁸Actually, these results are also a proof for the quality of our measurement setup. There is no additional external noise, *e.g.* electronic noise.

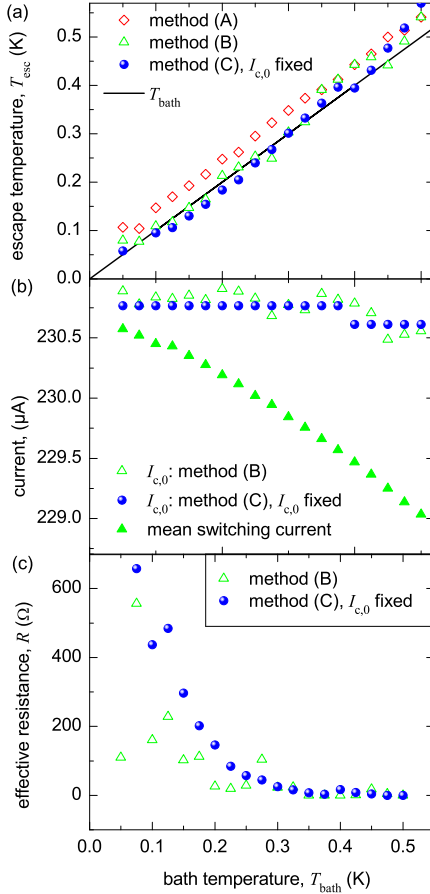


Figure 6.6: Experimental data of switching current measurements (sample SINFS-13H-sm/ π). In (a) T_{esc} vs. T_{bath} is plotted, in (b) $I_{c,0}$ and the mean switching current vs. T_{bath} , in (c) the respective effective resistances vs. T_{bath} . Method (A), (B) and (C) are the same as used in Fig. 6.5. Here, $I_{c,0}$ is fixed within segments.

in comparison to the bath temperature. Taking (intermediate) damping into account (B and C), improves the agreement between bath and escape temperature significantly. For both samples (SINFS-13H-sm/ π and SINFS-13H-sm/0- π), method (C) shows a smaller deviation from the bath temperature. Here, $I_{c,0}$ calculated by method (B) is not as constant

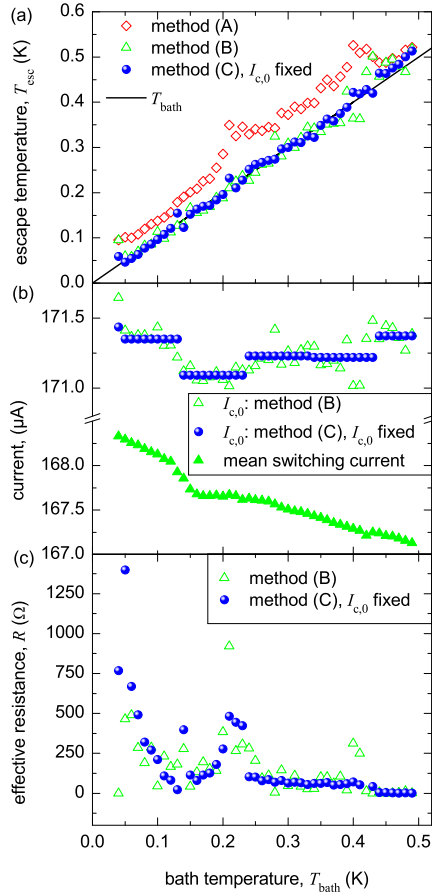


Figure 6.7: Switching current measurements (the experimental data are taken in the right maximum of the $I_c(B)$ of sample SINFS-13H-sm/ $0-\pi$). In (a) T_{esc} vs. T_{bath} is plotted, in (b) $I_{c,0}$ and the mean switching current vs. T_{bath} , in (c) the respective effective resistances vs. T_{bath} . Again, method (A), (B) and (C) are same as used in Fig. 6.5 and $I_{c,0}$ is fixed within segments.

as for sample SINFS-13H-sm/ 0 . Thus, $I_{c,0}$ is taken as fixed within some segments. The respective segments are chosen by sight, see Figs. 6.6 (b) and 6.7 (b). The overall behavior of the effective resistance of sample SINFS-13H-sm/ 0 is recovered for samples SINFS-13H-sm/ π and SINFS-

13H-sm/0- π . Above $T = 200$ mK the resistance has a value of a few ohms. Below this temperature the effective resistance increases significantly. Especially the data analysis for sample SINFS-13H-sm/ π seems to exert an exponential dependence of the resistance. Sample SINFS-13H-sm/0- π exhibits a strange feature between $100 \text{ mK} < T < 220 \text{ mK}$, it is visible in the mean switching current dependence vs. temperature as a dip and as a maximum in the $R(T)$ dependence. This feature remains unclear, it is observed in switching current measurements in both maxima of the $I_c(B)$ pattern. The origin of the strong increase of the effective resistance for our SIFS samples with decreasing temperature is not understood yet. It is even unclear whether this feature is due to some physical reasons, which are, *e.g.*, special for SIFS Josephson junctions. One might speculate whether it is due to the opening of an additional gap which is induced inside the ferromagnet. Another, much simpler reason might be, that it is a kind of artefact due to problems with the fitting routine, which we have not found yet. It is difficult to check the $R(T)$ dependence using another measurement scheme, *e.g.* IV measurements. At higher temperatures ($T > 200$ mK), the fit values ($\sim 10 \Omega$) seem to agree with subgap values of the current-voltage characteristics ($\sim 3 \Omega$). Below these temperatures it is not possible to determine the supgap resistance with IV measurements, as this measurement scheme is resistive and produces a large heat input which in turn increases the actual sample temperature. Additional switching current measurements on further SIFS samples are necessary to solve the question of the exponential dependence of the effective resistance. If further measurements support our findings, one might develop an additional scheme to directly measure the resistance at very low temperatures.

6.3 Microwave spectroscopy of short and intermediate length SIFS Josephson junctions

Additional studies on the resonant activation of the Josephson phase were performed by microwave spectroscopy on samples in the short (chip SFS64I) and intermediate length limit (chip JJF16), cf. Tab. 5.1. The eigenfrequencies of 0- π junctions as well as of the reference junctions were examined to answer the question whether a fingerprint of the semifluxon is observable. Special interest was paid to length effects. All microwave

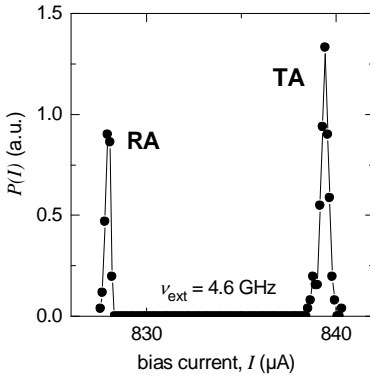


Figure 6.8: Example of a switching current histogram (JJF16/0) with two peaks: the resonant activation peak (RA) and the thermal activation peak (TA). The microwave frequency is $\nu_{\text{ext}} = 4.6$ GHz, $T = 320$ mK.

spectroscopy experiments were done around $T \sim 350$ mK, in the thermal regime.

The experimental data were obtained by irradiating the junctions with microwaves of frequencies close to $\nu_0 = \omega_0/2\pi$, cf. Eq. (3.2). As a starting point ω_P was estimated with the respective capacitance C obtained from Fiske step measurements and I_c from the $I_c(B)$ pattern. Switching current measurements were carried out simultaneously. The measurements were performed for different microwave power levels. At low power values the switching current distribution is comparable to the one without microwaves — no resonant excitation is observed. At some higher power values (the particular value depends on the coupling between antenna and sample) in addition to the thermal escape peak around I_c a resonant activation peak becomes visible at lower switching currents, see exemplarily Fig. 6.8. By tracking the current position of the resonant peak for different frequencies of the external drive ν_{ext} , the eigenfrequencies $\omega_0(\gamma)$ of the samples are obtained. This is done under the condition that the amplitudes of the resonant peak and of the initial escape peak are nearly equal.

First, samples on chip SFS64I were examined (short junction limit). The junctions were characterized by taking $I_c(B)$ measurements at $T = 345$ mK. Exemplarily, the $I_c(B)$ pattern of sample SFS64I/0- π is shown in Fig. 6.9. The $I_c(B)$ is highly symmetric, indicating a high quality of the junction and a homogeneous current distribution⁹. The magnetic field dependencies of the reference junctions are very regular, too, their maxima are centered around zero magnetic field (data not shown). Mi-

⁹The precise shape of the $I_c(B)$ with its bumped side minima is studied in detail in [KWW⁺09] and was already discussed in Sec. 5.2.

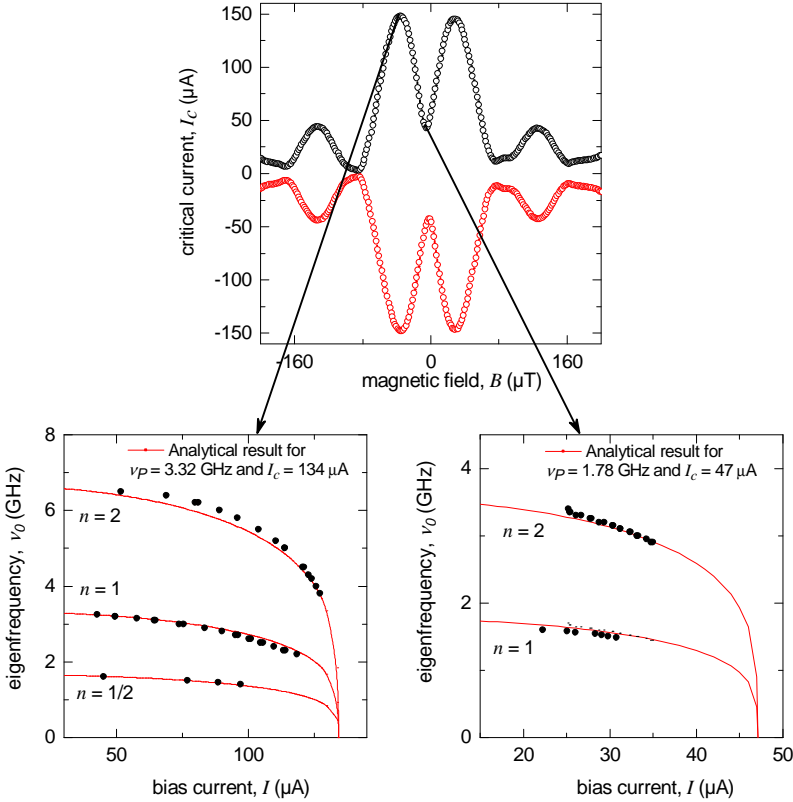


Figure 6.9: Resonant activation of the short junction SFS64I/0- π at $T = 345$ mK. (a) Experimental data of critical current vs. magnetic field dependence at $T = 345$ mK. Microwave spectroscopy is done in the left maximum and the central minimum of the $I_c(B)$ pattern. Harmonic ($n = 1$), subharmonic ($n = 1/2$) and superharmonic ($n = 2$) branches are indicated. Analytical fits are plotted as red, solid lines; the respective fit parameters are indicated. Experimental data are plotted as black, solid dots.

crowave spectroscopy was done for sample SFS64I/ π (data not shown) and sample SFS64I/0- π . The experimental data of sample SFS64I/0- π are obtained in the left maximum (see left side of Fig. 6.9) and in the central minimum (see right side of Fig. 6.9) of the magnetic field

dependence¹⁰. As the junction is in the short junction limit, there is no jump near the central minimum which could complicate switching current measurements. The eigenfrequencies are plotted as a function of bias current, see Fig. 6.9. In both graphs, several branches are visible. We identify these branches as harmonic pumping ($\sim \nu_0$), superharmonic pumping ($\sim n \times \nu_0$, n being an integer number) and subharmonic pumping ($\sim \frac{\nu_0}{n}$). To analyze the spectroscopy data, as a first try, the eigenfrequencies are fitted according to the pointlike junction model

$$\nu_n = \frac{n\omega_0(\gamma)}{2\pi}, \quad (6.3)$$

by using the ORIGIN 7.5 standard fitting tool for least square fits. I_c and $\nu_P = \omega_P/2\pi$ are taken as fitting parameters. The results are shown in Fig. 6.9 as solid red lines. The respective fit values for I_c and ν_P are indicated. The values for I_c and ν_P obtained from the fit are very close to the ones estimated from Fiske step measurements and from $I_c(B)$ pattern (values in the left maximum of the $I_c(B)$ pattern: $I_{c,\text{exp}} = 128 \mu\text{A}$ / $I_{c,\text{fit}} = 134 \mu\text{A}$, $\nu_{P,\text{exp}} = 3.24 \text{ GHz}$ / $\nu_{P,\text{exp}} = 3.32 \text{ GHz}$. Values in the central minimum: $I_{c,\text{exp}} = 39 \mu\text{A}$ / $I_{c,\text{fit}} = 47 \mu\text{A}$, $\nu_{P,\text{exp}} = 1.79 \text{ GHz}$ / $\nu_{P,\text{exp}} = 1.78 \text{ GHz}$.)

The fit according to the pointlike junction model (Eqs. (3.2) and (6.3)) reproduces quantitatively the experimental spectroscopy data of sample SFS64I/0- π . The experimental microwave spectroscopy data of sample SFS64I/ π are reproduced by the pointlike junction model fit with high accuracy, too (data not shown). There is not discrepancy between the eigenfrequencies according to the pointlike junction model and the experimental data. The experimental spectroscopy data of sample SFS64I/0- π do not show a signature of the fractional flux pinned at the 0- π boundary (not even the experimental data in the minimum of the $I_c(B)$ dependence show a fingerprint of the semifluxon). The main reason is, that the portion of semifluxon in junction SFS64I/0- π is rather small ($\Phi \sim \Phi_0 l^2/8\pi < 2\% \Phi_0$), compare Sec. 5.2. It is too small to have an observable influence, neither in the maximum nor in the minimum of the $I_c(B)$ dependence. Second, the samples are SIFS rather than SIS samples, but there seems to be no influence of the F-layer on the eigenfrequencies. The main influence of the F-layer is the reduction of the

¹⁰In contrast to the last subsection, microwave spectroscopy can be performed near the central minimum of the $I_c(B)$ pattern. Here, the low resolution of the measurement scheme is not crucial, as we only track the mean peak position of the histograms. This tracking is done by sight.

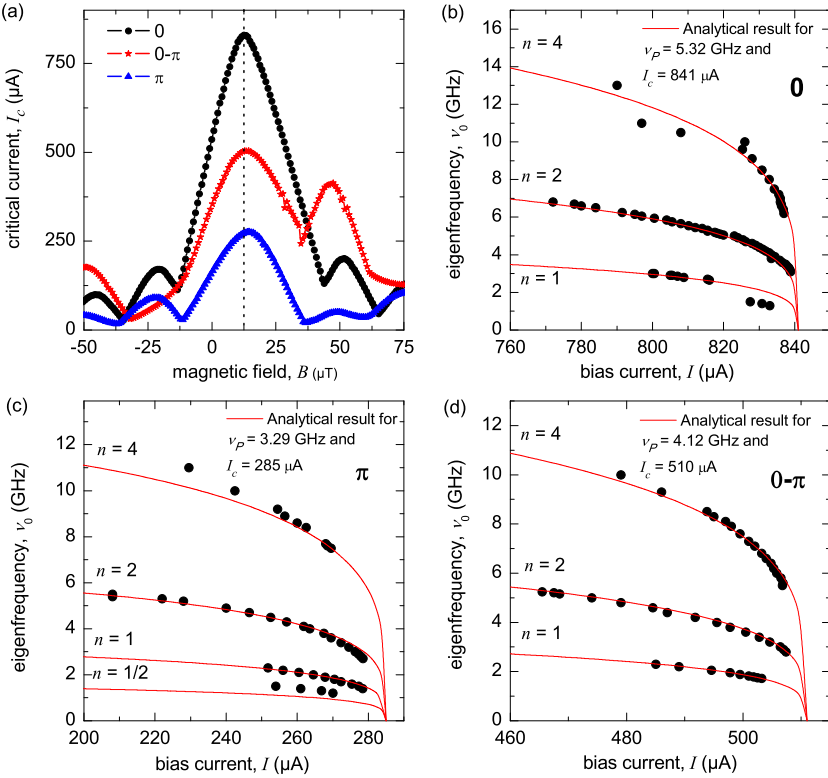


Figure 6.10: Resonant activation of the intermediate length samples JJJ16/0, JJJ16/ π and JJJ16/ $0-\pi$ at $T = 320$ mK. (a) Experimental data of the critical current vs. applied magnetic field of the three samples at $T = 320$ mK. The dotted line indicates the measurement positions for microwave spectroscopy. $\nu_0(\gamma)$ dependencies for the 0 (b), π (c) and $0-\pi$ (d) Josephson junction. Harmonic ($n = 1$), subharmonic ($n = 1/2$) and superharmonic ($n = 2, 4$) branches are indicated. The parameters I_c and ν_P of the analytical fits (solid red lines) are given. Black dots show experimental data.

critical current (which is considered in ω_P). Overall, regarding resonant activation of the Josephson phase, short 0, π and $0-\pi$ SIFS junctions can be described by the same pointlike junction theory as short 0 SIS junctions.

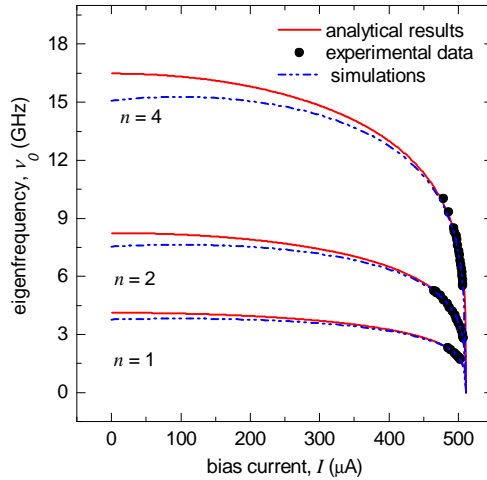


Figure 6.11: Comparison between experimental data (black, filled circles), analytical fit (red, solid line) and numerical simulations (blue, dash dotted line) of the microwave spectroscopy data of junction JJF16/0- π at 320 mK.

In a second measurement cycle, the intermediate length samples on chip JJF16 were studied. Here, the JJF16/0- π junction carries a magnetic flux of $\Phi \sim \Phi_0 l^2 / 8\pi = 25\% \Phi_0$ at $T = 320$ mK. Both reference junctions exhibit an almost regular Fraunhofer pattern indicating no substantial amount of parasitic flux, see Fig. 6.10 (a). Note however, that both curves are not centered around zero magnetic field, but shifted by $\sim 12 \mu\text{T}$. This shift and also the asymmetries in the side lobes of the Fraunhofer pattern might occur due to a finite magnetization of the F-layer [KWW⁺09] and were different in every cooldown. For the 0- π junction the characteristic dip in the middle of the $I_c(B)$ is visible, being a signature of the 0- π boundary [WKK⁺06]. By coincidence, the left maximum at $\sim 12 \mu\text{T}$ coincides with the maxima of the two reference junctions. The microwave spectroscopy measurements were performed at the maxima of the $I_c(B)$ patterns (see dotted line in Fig. 6.10 (a))¹¹. Fig. 6.10 (b) - (d) shows the measured eigenfrequencies of the three

¹¹Here, switching current measurements are difficult in the minimum of the $I_c(B)$ pattern of the intermediate 0- π junction, as the minimum reveals a jump of I_c which slightly shifts with temperature, compare Subsec. 5.2.2. Thus, the region around the central minimum is highly instable in experiment and not appropriate for long-lasting switching current measurements.

samples JJF16/0, JJF16/ π and JJF16/0- π as a function of bias current. We again observe harmonic, superharmonic and subharmonic pumping. To analyze the spectroscopy data, as a first try we used the pointlike junction model (Eq. (6.3)) for fitting the eigenfrequencies. The results are shown in Fig. 6.10 as solid red lines. The respective values for I_c and ν_P are indicated as before. The fit values are pretty close to the experimentally determined ones: $I_{c,\text{exp}}/I_{c,\text{fit}} = 0.98\dots 1.0$, $\nu_{P,\text{fit}}/\nu_{P,\text{exp}} = 0.80\dots 0.85$ for all three junctions. Again, although the samples are in an intermediate length limit, the fit according to the pointlike junction model perfectly reproduces the experimental data. The fit according to the pointlike junction model neither takes the asymmetries of our 0- π junctions nor the 0- π boundary into account, but even seems to be appropriate for intermediate SIFS 0- π junctions. Although the JJF16/0- π junction carries a significant portion of semifluxon, it is not visible in experiment.

To answer the question why we do not observe the semifluxon in experiment, we perform numerical simulations of the eigenfrequencies of the JJF16/0- π junction¹². These simulations take the different $j_c^0 \neq j_c^\pi$ in the 0 and π regimes and the finite length of the junction into account. For given junction parameters and fixed bias current, in a first step we find a stable static¹³ solution $\mu_0(x)$ of the sine-Gordon equation

$$\mu_{xx} - j_c(x) \sin(\mu) = \gamma. \quad (6.4)$$

We next assume that the phase $\mu(x, t)$ can be written in the form

$$\mu(x, t) = \mu_0(x) + \sum_n \psi_n(x) e^{i\omega_n t}, \quad (6.5)$$

i.e., it performs small oscillations around the static solution $\mu_0(x)$. The eigenfunctions $\psi_n(x)$ and the eigenfrequencies ω_n are found as solutions of the Schrödinger-like equation

$$-\psi_{xx} + j_c(x) \cos(\mu) \psi = \omega^2 \psi. \quad (6.6)$$

From all eigenfrequencies we choose the lowest one, ω_0 , and plot it as a function of γ in Fig. 6.11. To plot the eigenfrequency in physical units, we have to multiply our simulation results obtained in normalized units

¹²The numerical simulations were done by Dr. E. Goldobin.

¹³In fact we solve the dynamic sine-Gordon equation and wait until the solution has relaxed to a static one.

by the plasma frequency (the higher branches are calculated by multiplying the obtained eigenfrequency with appropriate integers n). In Fig. 6.11 we use the scaling which provides the best fit to the experimental data. From Fig. 6.11 we easily see why our experimental data are reproduced by the simple pointlike junction model. The experimental data are located in a parameter range where both descriptions — the simple pointlike junction model and the more accurate numerical simulations — coincide. Length effects and the signature of the $0-\pi$ boundary should be observable in a parameter range which is not accessible with our experimental setup: The lowest values of dc bias current need larger microwave amplitudes to produce a significant number of switching events. Thus, the experimental observation of data values in the low bias current range is limited by the microwave power of our setup. From our studies we conclude that, to see a clear fingerprint of the semifluxon in microwave spectroscopy, long $0-\pi$ junctions should be measured at a field position near the central minimum. As discussed in the last section, the influence of the semifluxon is strongest in the minimum of the $I_c(B)$ pattern.

6.4 Conclusions

In this chapter, we presented the results of escape rate measurements and microwave spectroscopy measurements of short and intermediate length ferromagnetic Josephson junctions. We developed a deep understanding of the effective barrier height of short SIFS Josephson junctions as a function of applied magnetic field. The activation energy can be described in the framework of the thermal activation theory of short Josephson junctions, for 0 , π as well as $0-\pi$ junctions. The escape temperature coincides with the temperature of the environment, almost regardless of the applied magnetic field. Taking resolution-dependent corrections into account, simulations reproduce our experimental data with a good accuracy. There is no indication for a deviation from standard SIS samples which is due to the F-layer, *e.g.*, additional spin noise. There is no broadening of the switching current histograms due to the coil current, indicating the high quality of our experimental setup.

Thermal escape rate measurements were performed in the temperature range between 0.5 K...25 mK. As expected in the case of intermediate damping, the escape temperature is equal to the temperature of the environment, $T_{\text{esc}} = T_{\text{bath}}$. The junctions are described by the pointlike

junction model with a high accuracy, taking damping into account. As expected from the pointlike junction model ($T^* < 10$ mK), there is no saturation of the standard deviation vs. temperature visible. The data presented here are all in the *thermal* regime. The probability distribution of the switching currents are precisely remodeled by the lumped junction model, even in the low temperature regime. These are the first measurements of SIFS Josephson junctions down to 25 mK which proof the well behavior of these junctions. It might be important to know for quantum applications that these devices are not limited due to poor noise properties. As expected in the short limit, we do not observe any difference between SIFS junctions with 0 , π and $0-\pi$ coupling.

Finally, we experimentally determined the eigenfrequencies of short and intermediate $0-\pi$ junctions and their respective reference junctions by microwave spectroscopy. The spectroscopy data were obtained in the thermal regime, at $T \sim 350$ mK. We observed harmonic, subharmonic and superharmonic pumping. The experimental data were compared with numerical simulations of the short junction model and revealed a good agreement between theory and experiment.

Summary

In the framework of this thesis, we presented detailed studies on ferromagnetic (SIFS) $0-\pi$ Josephson junctions with their respective 0 and π reference junctions (so-called *triplets*). The samples were characterized by determining their *static* and *dynamic* properties. We measured magnetic field dependencies of the critical current, $I_c(B)$, and current-voltage characteristics, IVC, by using a standard ^4He - and ^3He -cryostat. In contrast to studies published so far on SFS/SIFS Josephson junctions, we examined samples of different geometries (*linear* and *annular*) and of different length (ranging from the *short* to the *long* length limit). In total, the results of five junction triplets were presented throughout this thesis. One should note, that our SIFS samples exhibit comparatively high critical current densities (up to $j_c = 40 \text{ A/cm}^2$ in the π state). *Phase escape* experiments were performed in the *thermal* regime by measuring switching current statistics. The experimental conditions in the dilution refrigerator could be varied by applying external magnetic field or microwaves and by changing the temperature between $25 < T < 500 \text{ mK}$. At sufficiently low temperatures, $T < 4.2 \text{ K}$, all samples were *underdamped*.

The motivation for our studies was twofold: First, we wanted to figure out, whether the additional F-layer has any influence on the Josephson physics, *i.e.*, whether there is any difference between the static and dynamic properties of SIS Josephson junctions and of SIFS Josephson junctions. Thus, we focused on the investigation of the 0 and π coupled reference junctions. Concerning their static properties, the reference junctions often exhibited a behavior which is typical for SIFS junctions, but is not observed for standard 0 SIS Josephson junctions: The $I_c(B)$ dependencies of the reference junctions showed an offset from zero magnetic field. This might be due to a finite magnetization of the ferromagnetic layer, which is changing whenever the sample crosses its Curie-

temperature. The offset was not constant and the precise shape of the $I_c(B)$ pattern slightly changed with (almost) every cooldown (although no parasitic flux was trapped!). Regarding the dynamic properties of the reference junctions, we observed no discrepancy from standard Josephson physics. Depending on the respective experimental conditions, Fiske steps, zero field steps and Shapiro steps were verified, exactly as expected from theory. There was no indication for a second harmonics contribution to the current-phase-relation. Regarding the phase escape measurements, we found no indication that the additional ferromagnetic layer changes the escape mechanisms of the Josephson phase. Switching current measurements were performed in the presence of magnetic field at a constant temperature $T = 200$ or 300 mK. We developed a deep understanding of the effective barrier height of short SIFS samples as a function of magnetic field. Numerical simulations revealed, that the activation energy can be described in the framework of short junction theory. Furthermore, phase escape experiments were carried out at temperatures between $25 \text{ mK} < T < 500 \text{ mK}$. As predicted from theory, for the experimental parameters of the samples used in this thesis, we did not observe the crossover to the *quantum* regime. The data presented here were all obtained in the *thermal* regime. Taking damping into consideration, the probability distributions of the switching currents were precisely remodeled by the lumped junction theory. As expected in the case of intermediate damping, the escape temperatures coincided perfectly with the bath temperatures. Using microwave spectroscopy, the eigenfrequencies of 0 and π junctions were investigated. We observed harmonic, subharmonic and superharmonic pumping. The experimental data were compared with pointlike junction theory and showed an excellent agreement. Overall, we did not find any indication for additional spin noise due to the presence of the ferromagnetic layer. Our SIFS Josephson junctions could be described according to standard Josephson theory. It might be important to know for quantum applications that the usability of these SIFS Josephson junctions is not restricted by poor noise properties.

The second aim of this thesis was an extensive investigation of the phase boundary in 0 - π junctions and the associated fractional vortices. Regarding the static properties of 0 - π junctions, a strong signature of the 0 - π boundary in a short junction was demonstrated by measuring the $I_c^{0-\pi}(B_x, B_y)$ pattern: the central minimum around zero field ($B_y = 0$). The second magnetic field orientation guaranteed, that no trapped parasitic flux falsified the results. Additionally, SIFS 0 - π junctions show

a clear indication of the finite magnetization of the ferromagnetic layer. The $I_c(B)$ dependencies are shifted from zero magnetic field and revealed an asymmetric height of the maxima and bumped side minima. The precise shape of the $I_c(B)$ pattern of a $0-\pi$ junction crucially depends on several aspects, *e.g.*, its length and the different critical current densities in both halves of the junction. Taking the asymmetry into account, the comparison between experimental data and numerical simulations showed a good quantitative agreement for all $0-\pi$ junctions presented in this thesis. Discrepancies between numerics and experimental data were assigned to the fact, that we could not take ferromagnetic properties, as the finite magnetization, into account for numerical simulations. Investigating $I_c(B)$ dependencies of long $0-\pi$ junctions, we verified complicated metastable fluxon/semifluxon configurations in experiment, which had been theoretically predicted. Furthermore, we studied the dynamic properties of $0-\pi$ junctions in the short and long length limit. *Half-integer* zero field steps were found on the current-voltage characteristics of short $0-\pi$ Josephson junctions. The step current dependencies of several Fiske and zero field steps on applied magnetic field were measured experimentally and the results were analyzed analytically, revealing an excellent agreement. To our knowledge, this is the first time that a half-integer zero field step is reported for SIFS $0-\pi$ Josephson junctions. Comparable measurements of long $0-\pi$ junctions revealed complicated substructures (satellite steps) on the zero field steps in experiment and in numerics. The dynamics on (half-inter) zero field steps were identified by simulating the trajectories of the semifluxon(s). At the satellite steps the system changes between a Fiske-step-like motion and a bunched mode of semifluxons/antisemifluxons. This behavior had been predicted in theory, it is now verified in experiment.

The respective barrier height of short $0-\pi$ junctions was examined as a function of magnetic field and as a function of temperature. The data analysis of switching current measurements showed, that there is no indication of spin noise or other extra noise related to the ferromagnetic layer in comparison to standard SIS samples. As in the case of the reference junctions, numerical simulations revealed that the activation energy vs. magnetic field could be described in the framework of short junction theory. Within the limits of experimental resolution, the experimental data showed a good agreement with numerical simulations. Around zero magnetic field, in numerics we found a kink-like structure in the activation energy dependence, which is due to the $0-\pi$ boundary. This structure could not be resolved in experiment due to resolution restrictions. The

phase escape measurements at different temperatures were performed in the I_c maxima. Analogously to the reference junctions, these measurements revealed that the escape temperatures coincided well with the temperatures of the environment. As expected from theory, there was no additional noise contribution due to the fractional vortex; the effective barrier height was precisely remodeled by the pointlike junction theory. Using microwave spectroscopy, we determined the eigenfrequencies of a short and intermediate length $0-\pi$ junction. Again, we observed harmonic, subharmonic and superharmonic pumping. The experimental data showed a perfect agreement with the pointlike junction theory. Surprisingly, neither the length effects nor the phase discontinuity point had any observable influence on the effective barrier height. Numerical simulations revealed, that in the parameter range, which was accessible with our experimental setup, both, pointlike junction theory and the more detailed numerical simulations coincide.

Overall, we developed a deep understanding for SIFS Josephson junctions, with a phase coupling of 0 , π and $0-\pi$. We figured out their peculiar properties, *e.g.*, the finite magnetization of the F-layer, which are different from standard SIS Josephson junctions. Being aware of this, in the majority of cases short SIFS junctions are well described by the pointlike junction theory. We found no indication for additional spin noise due to the ferromagnetic layer. Furthermore, in the framework of this thesis, we experimentally verified some characteristics of short and long $0-\pi$ junctions, *e.g.*, half-integer zero field steps, metastable fluxon/semifluxon configurations and satellite steps.

Concerning the original aims of this thesis, there are some open questions left: Up to now, the influence of a semifluxon on the effective barrier height and on the phase escape mechanisms was not observed. For achieving this goal, long, very symmetric $0-\pi$ Josephson junctions with a substantial amount of trapped fractional flux should be used. Biasing these junctions around the central minimum during switching current measurements, should reveal an influence of the semifluxon on the phase escape mechanisms. Such measurements should be performed as soon as adequate samples are available. Furthermore, the observation of the crossover from thermal to quantum regime in $0-\pi$ junctions, is still an open problem of fundamental interest. Likewise, the respective samples of appropriate properties are not yet available. Fabrication of SIFS junctions with a high critical current, so that the crossover temperature is unambiguously detectable in the dilution refrigerator (*i.e.*, $T^* > 50$ mK), is a demanding task. On the one hand, the physical junction size should

be as small as possible to avoid inhomogeneities and other size effects. On the other hand, the critical current density of SIFS junctions is orders of magnitude lower than for SIS samples. Thus it is hard to fulfil both requirements of a small junction size and a high critical current. The fabrication of SIFS junctions with drastically enhanced critical current densities is a topic of current research. Increasing the critical current density of SIFS junctions, has a further advantage: A high critical current density is equivalent to a small Josephson penetration depth, thus making the fabrication of several $0-\pi$ transitions with fully developed semifluxons within *one* junction possible. $0-\pi$ discontinuity points are of fundamental interest as these systems provide semifluxons with a degenerate ground state for applications in quantum computing. Thus, $0-\pi$ junctions could be the basic element for the development of tailored quantum matter. One might think of many interesting and easily realizable $(0-\pi)_n$ -designs which are based on the simple $0-\pi$ elements examined in this thesis.

Zusammenfassung

Im Rahmen der vorliegenden Arbeit werden ausführliche Studien präsentiert, die sich mit ferromagnetischen (SIFS) $0-\pi$ Josephsonkontakten und ihren jeweiligen 0 und π gekoppelten Referenzkontakten beschäftigen. Ein $0-\pi$ Kontakt und seine zugehörigen 0 und π Referenzkontakte werden zusammen ein *Triplet* genannt. Zur Charakterisierung der Proben wurden zunächst ihre *statischen* und *dynamischen* Eigenschaften bestimmt. Die Abhängigkeit des kritischen Stromes vom angelegten Magnetfeld, $I_c(B)$, und die Abhängigkeit der Spannung vom angelegten Strom, beides Standard-Messmethoden, wurden jeweils in einem ^4He - und ^3He -Kryostaten gemessen. Im Gegensatz zu bisher veröffentlichten Studien, die sich mit SFS/SIFS Kontakten beschäftigten, werden in der vorliegenden Arbeit sowohl Kontakte verschiedener Geometrien (linear und annular) als auch Kontakte verschiedener Längen (kurze und lange) untersucht. Insgesamt werden die Ergebnisse von fünf Kontakt-Triplets vorgestellt. Desweiteren soll darauf hingewiesen werden, dass die hier verwendeten SIFS Proben für den derzeitigen Stand der Technik vergleichsweise hohe kritische Stromdichten aufweisen (im π Zustand werden bis zu $j_c = 40 \text{ A/cm}^2$ erreicht). Im zweiten experimentellen Kapitel dieser Arbeit werden Experimente vorgestellt, die sich mit Escape-Prozessen der Josephsonphase aus einem metastabilen Potentialtopf beschäftigen. Zu diesem Zweck wurden Schaltstatistiken des kritischen Stromes in einem Mischkryostaten gemessen. In dem Mischkryostaten konnte sowohl kontrolliert ein externes Magnetfeld angelegt und Mikrowellen eingestrahlt werden, ebenso konnte die Temperatur zwischen $25 < T < 500 \text{ mK}$ variiert werden. Eine wesentliche Eigenschaft der hier verwendeten SIFS Josephsonkontakte besteht darin, dass sie bei Erniedrigung der Temperatur unter $T < 4.2 \text{ K}$ vom über- ins unterdämpfte Regime überführt werden konnten.

In der vorliegenden Arbeit sollten im Wesentlichen zwei Fragestellungen

gen untersucht werden: Einerseits sollte herausgefunden werden, ob die zusätzliche ferromagnetische Zwischenschicht einen merklichen Einfluss auf die Josephsonphysik ausübt, will heißen, ob die statischen und dynamischen Eigenschaften von SIFS Kontakten sich von den entsprechenden Eigenschaften in SIS Kontakten unterscheiden. Zur Beantwortung dieser Frage habe ich mich intensiv mit den 0 und π gekoppelten Referenzkontakten beschäftigt. Ein Ergebnis der Untersuchungen besteht darin, dass die $I_c(B)$ Kurven von SIFS Kontakten bezüglich des angelegten Feldes nicht symmetrisch sind, sie weisen auch ohne extern angelegtes Magnetfeld eine Verschiebung vom Nullfeld auf. Dieses Verhalten ist von SIS Standardkontakten nicht bekannt. Eine mögliche Erklärung besteht darin, dass die ferromagnetische Zwischenschicht in SIFS Kontakten eine definierte Restmagnetisierung aufweist, die sich mit jedem Durchgang durch die Curietemperatur der jeweiligen Probe ändert. Bezeichnenderweise ist die Verschiebung des $I_c(B)$ Graphen im Magnetfeld und seine genaue Gestalt für (fast) jeden Einkühlvorgang der Probe unterschiedlich (und das, obwohl keine eingefangenen Abrikosovflusswirbel die Messung stören!). Bei der Untersuchung der dynamischen Eigenschaften der SIFS Referenzkontakte konnten keine Unterschiede zur normalen Josephsonphysik nachgewiesen werden. Je nachdem, wie die experimentellen Gegebenheiten ausgerichtet waren, konnten Fiskestufen, Nullfeldstufen und Shapirostufen beobachtet werden, und zwar genauso, wie sie theoretisch vorhergesagt werden. Es konnte keinerlei Hinweis auf die Notwendigkeit höherer Harmonischer zur Strom-Phasen-Beziehung gefunden werden. Bei der Untersuchung der Josephsonphase-Escapeprozesse wurden keine Anzeichen dafür gefunden, dass die zusätzliche ferromagnetische Zwischenschicht die bekannten Standardprozesse der Kramer-Theorie modifiziert: Zunächst wurden Schaltstatistiken bei konstanter Temperatur, $T = 200$ oder 300 mK, in Abhängigkeit vom angelegten Magnetfeld durchgeführt. Mittels numerischer Simulationen konnte für kurze SIFS Referenzkontakte gezeigt werden, dass die Abhängigkeit der effektiven Barrierehöhe vom Magnetfeld, und damit auch die Abhängigkeit der Aktivierungsenergie vom Magnetfeld, mittels der Theorie für kurze Josephsonkontakte beschrieben werden kann. Ein ähnliches Resultat ergaben Schaltstatistikmessungen bei unterschiedlichen Temperaturen $25 < T < 500$ mK. Unter Berücksichtigung von Dämpfungseffekten konnten die Histogramme der Schaltstatistikmessungen perfekt durch Simulationen reproduziert werden, die auf Grundlage der Theorie für kurze Josephsonkontakte (lumped junction model) erzeugt wurden. Wie es im Falle gemäßigter Dämpfung erwartet wird, stimmten die Escape-

temperaturen genau mit den angelegten Badtemperaturen überein. Alle hier vorgestellten Schaltstatistikmessungen wurden im thermischen Regime aufgenommen. Wie für die vorliegenden Probenparameter erwartet, konnte kein Übergang ins Quantenregime beobachtet werden. Die Eigenfrequenzen der Referenzkontakte wurden mittels Mikrowellenspektroskopie ermittelt. Sowohl harmonische, als auch subharmonische und superharmonische Übergänge wurden beobachtet. Die experimentellen Daten wurden mit der Theorie punktförmiger Kontakte analysiert und zeigten eine hervorragende Übereinstimmung. Insgesamt konnte kein Hinweis auf ein zusätzliches Spinrauschen gefunden werden, dessen Ursache in der ferromagnetischen Zwischenschicht begründet liegt. Die vorliegenden SIFS Josephsonkontakte können mit der Standard-Josephsontheorie beschrieben werden. Wichtig ist dies vor allem im Zusammenhang mit Anwendungen für Quantensysteme, z. B. Quantencomputer. Die Ergebnisse dieser Arbeit deuten darauf hin, dass die Anwendbarkeit von SIFS Kontakten nicht durch ungünstige Rauscheigenschaften eingeschränkt wird.

Die zweite große Fragestellung in dieser Arbeit war die Untersuchung von $0-\pi$ Grenzflächen und die Charakterisierung der daran ausgebildeten fraktionalen Flusswirbel. Ein eindeutiger Nachweis einer $0-\pi$ Grenzfläche besteht in dem zentralen Minimum im $I_c(B)$ Graphen eines $0-\pi$ Kontaktes. Für einen kurzen $0-\pi$ Josephsonkontakt wurde eben dieses zentrale Minimum in einer $I_c^{0-\pi}(B_x, B_y)$ Messung nachgewiesen. Gleichzeitig konnte durch Verwendung einer zweiten Magnetfeldorientierung ausgeschlossen werden, dass eingefangener parasitischer Fluss die Messung verfälschte. Auch die $0-\pi$ SIFS Proben geben deutliche Hinweise auf die Anwesenheit der ferromagnetischen Zwischenschicht. Auch ihre $I_c(B)$ Abhängigkeiten sind im Feld verschoben, die beiden Maxima haben nicht die gleiche Höhe und die Seitenminima weisen deutliche Asymmetrien auf. Die genaue Gestalt der $I_c(B)$ Graphen von $0-\pi$ Kontakten hängt von mehreren Faktoren ab, entscheidend sind jedoch die Kontaktlänge und die Asymmetrie der kritischen Stromdichten in beiden Kontakthälften. Berücksichtigt man diese, so stimmen die numerischen Simulationen für alle in dieser Arbeit gezeigten $0-\pi$ Josephsonkontakte quantitativ mit den experimentellen Daten überein. Kleine Abweichungen zwischen Simulation und Experiment sind vor allem darauf zurückzuführen, dass in den Simulationen die ferromagnetischen Eigenschaften der Zwischenschicht, wie etwa die Restmagnetisierung, nicht berücksichtigt werden können. Bei der Untersuchung von langen $0-\pi$ Kontakten konnten in $I_c(B)$ Messungen komplizierte Fluxon/Semifluxon Zustände nachgewiesen werden,

die bereits theoretisch vorausgesagt worden waren, bisher experimentell aber noch nicht bestätigt worden waren. Desweiteren wurden die dynamischen Eigenschaften von kurzen und langen $0-\pi$ Kontakten untersucht. Auf der Strom-Spannung-Kennlinie eines kurzen $0-\pi$ Kontaktes konnte eine halbzahlige Nullfeldstufe nachgewiesen werden. Die Abhängigkeit des maximalen Stufenstroms mehrerer Fiske- und Nullfeldstufen vom angelegten Magnetfeld wurde experimentell ermittelt und analytisch analysiert. Die Übereinstimmung zwischen Theorie und Experiment war exzellent. Soweit mir bekannt ist, stellen diese Messungen den ersten experimentellen Nachweis von halbzahligen Nullfeldstufen in SIFS Josephsonkontakten dar. Ähnliche Messungen an langen $0-\pi$ Kontakten zeigten Substrukturen (sogenannte Satellitenstufen) auf den Nullfeldstufen, und zwar sowohl experimentell als auch in numerischen Simulationen. Um die Dynamik auf diesen Nullfeldstufen zu untersuchen, wurden die Trajektorien der Semifluxonen auf den Nullfeldstufen simuliert. Es konnte gezeigt werden, dass sich die Dynamik des Systems an den Satellitenstufen ändert. Zunächst handelt es sich um stehende Wellen, die an den Satellitenstufen in eine Form gebündelter Semifluxonen/Antisemifluxonen übergehen. Dieses Verhalten war theoretisch vorausgesagt worden und ist jetzt experimentell bestätigt worden.

Die effektiven Barrierenhöhe in kurzen $0-\pi$ Kontakten wurde als Funktion von Magnetfeld und Temperatur untersucht. Die Datenanalyse der Schaltstatistikmessungen ergab, dass die ferromagnetische Zwischenschicht im Vergleich zu SIS Kontakten zu keinerlei zusätzlichem Spinrauschen führt. Wie schon bei der Behandlung der Referenzkontakte diskutiert, konnte auch für $0-\pi$ Kontakte die Aktivierungsenergie im Model eines kurzen Josephsonkontaktes beschrieben werden. Innerhalb der vorgegebenen Auflösungsgrenzen zeigten die experimentellen Daten eine gute Übereinstimmung mit der Theorie. Als eine Besonderheit der $0-\pi$ Kontakte zeigten die numerischen Simulationen eine Knick-artige Struktur in der Aktivierungsenergie für niedrige Magnetfeldwerte. Diese Struktur konnte im Experiment nicht nachgewiesen werden, da sie unter der experimentellen Auflösungsgrenze lag. Im Gegensatz zu den Schaltstatistikmessungen der Referenzkontakte vs. Temperatur, die ohne angelegtes Magnetfeld durchgeführt worden waren, wurden die Schaltstatistikmessungen eines kurzen $0-\pi$ Kontaktes in beiden Maxima des $I_c(B)$ Graphen durchgeführt. Auch in diesen Messungen stimmten die ermittelten Escapetemperaturen gut mit den Badtemperaturen überein. Wie theoretisch erwartet, war kein zusätzliches Rauschen zu beobachten, das auf der Anwesenheit eines fraktionalen Flusswirbels beruhte. Die effek-

tive Barrierhöhe des Systems wurde präzise durch die Theorie eines punktförmigen Josephsonkontaktes wiedergegeben. Zusätzlich wurden die Eigenfrequenzen eines kurzen und mittellangen $0-\pi$ Kontaktes ermittelt. Auch hier wurde Mikrowellenspektroskopie verwendet. Wie im Fall der Referenzkontakte konnten harmonische, subharmonische und superharmonische Übergänge nachgewiesen werden. Überraschenderweise konnte kein Längeneffekt und kein Einfluss des Phasensprunges auf die effektive Barrierhöhe ermittelt werden. Den Grund dafür ergaben numerische Simulationen. Es stellte sich heraus, dass in den von dem vorliegenden Messaufbau festgelegten Parameterbereich die Theorie eines punktförmigen Josephsonkontaktes mit den detaillierten numerischen Simulationen übereinstimmt.

Zusammenfassend kann also festgestellt werden, dass im Rahmen dieser Arbeit ein tiefes Verständnis für die Physik von SIFS Josephsonkontakten entwickelt wurde, sowohl für 0 und π , als auch für $0-\pi$ gekoppelte Kontakte. Die wesentlichen Unterschiede im Vergleich zu SIS Kontakten wurden herausgearbeitet, so z. B. die Restmagnetisierung der ferromagnetischen Zwischenschicht und die damit verbundenen Probleme. Zieht man dies allerdings in Betracht, so können kurze SIFS Kontakte in den allermeisten Fällen mit der Theorie eines punktförmigen Josephsonkontaktes beschrieben werden. Desweiteren wurden keine Hinweise auf zusätzliches Spinrauschen gefunden, das auf die ferromagnetische Zwischenschicht zurückzuführen ist. Im Rahmen dieser Arbeit konnten verschiedene Besonderheiten von kurzen und langen $0-\pi$ Kontakten experimentell nachgewiesen werden, so z. B. halbzahlige Nullfeldstufen, metastabile Fluxon/Semifluxon Konfigurationen und die sogenannten Satellitenstufen.

Was die ursprünglichen Zielsetzungen dieser Arbeit angeht, bleiben einige Fragen leider ungeklärt: Bisher konnte kein Einfluss fraktionaler Flusswirbel auf die effektive Barrierhöhe und auf die Escape-Prozesse der Josephsonphase beobachtet werden. Um dies zweifelsfrei nachweisen zu können, sind lange, möglichst symmetrische $0-\pi$ Kontakte nötig, die eine möglichst große Menge an fraktionalem Fluss aufweisen. Führt man Schaltstatistikmessungen in der Nähe des zentralen Minimums der $I_c(B)$ Abhängigkeit durch, sollte ein Einfluss des Semifluxons auf die effektive Barrierhöhe gezeigt werden können. Derartige Messungen scheitern leider derzeit an dem Fehlen geeigneter Proben. Desweiteren steht ein Nachweis für den Übergang von $0-\pi$ Kontakten ins Quantenregime aus. Auch hier fehlen bisher geeignete Kontakte. Die Herstellung von SIFS Josephsonkontakten, die eine hohe kritische Stromdichte aufwei-

sen, gestaltet sich schwierig. Ein hoher kritischer Strom ist allerdings nötig, um zweifelsfrei im Mischkryostaten (*i.e.*, $T^* > 50$ mK) einen Übergang ins Quantenregime zu beobachten. Einerseits sollen die Proben möglichst kleine Kontaktflächen aufweisen, um Inhomogenitäten und andere Längeneffekte zu vermeiden. Andererseits ist die kritische Stromdichte von SIFS Kontakten um Größenordnungen kleiner als die von SIS Kontakten. Deswegen ist es schwierig, beiden Anforderungen, nämlich eine kleine Kontaktfläche bei hohem kritischen Strom, gerecht zu werden. Die Herstellung von SIFS Kontakten mit wesentlich höheren kritischen Stromdichten ist Gegenstand gegenwärtiger Forschung. Hohe kritische Stromdichten hätten noch einen weiteren Vorteil, da eine hohe kritische Stromdichte gleichbedeutend mit einer kleinen Josephsoneindringlänge ist. Auf diese Weise wäre es möglich, Strukturen mit mehreren $0-\pi$ Übergängen, die jeweils voll ausgebildete Semifluxonen tragen, in *einem* Kontakt zu realisieren. $0-\pi$ Übergänge sind von grundsätzlichem Interesse, da sie Semifluxonen mit entarteten Grundzuständen für die Anwendung in Quantensystemen zur Verfügung stellen. Deshalb könnten $0-\pi$ Kontakte das Grundelement für die Entwicklung von maßgeschneiderter Quantenmaterie darstellen. Es gibt viele interessante und leicht realisierbare $(0 - \pi)_n$ -Strukturen, die auf den im Rahmen dieser Arbeit untersuchten $0-\pi$ Übergängen beruhen.

Anhang A

Samples

In the table on the next side, Tab. A.1, we give an overview on the sample parameters which were used throughout this thesis. The names of the chips are taken over from Dr. M. Weides. Some chips contain *-sm* or *-lg* in their denotation. This is due to the fact, that the respective chip exists in two versions: On one chip small designs are realized, on the second chip large designs are implemented. The other parameters are equal for both chips (*e.g.*, they have the same thickness gradient of the ferromagnetic barrier), thus they are named almost equally. The abbreviations *-sm* stand for *small*, *-lg* for *large*. In Tab. A.1, *id* is the respective name of each junction which was used in this thesis; the *position* indicates the position of the junction on chip. Again, the nomenclature is used according to Dr. M. Weides: Each chip is separated in 2 – 3 blocks, which are described by roman numbers. After that, the first arabic number accounts for the row, the second arabic number is the column. Different *geometries* were chosen to realize our samples. First, the majority of the samples is designed in linear *overlap geometry*. Two different designs of the electrodes are used to bias the linear junctions, compare Fig. 5.1. *linear,narrow* accounts for the fact, that the linear junctions are biased with very narrow electrodes which are centered at the middle of the junction length. *linear,wide* describes linear junctions whose electrodes are as wide as the whole junction length. The *annular* junctions are designed in *Lynby*-geometry [DDKP85].

id	position	j_c (A/cm ²)	l	L (μm)	W (μm)	W_i (μm)	geometry
SFS64I/0	II-4-2	2.1	0.72	330	30	50	linear,narrow
SFS64I/ π	II-4-3	1.5	0.62	330	30	50	linear,narrow
SFS64I/0- π	I-3-3	1.8	0.67	330	30	50	linear,narrow
JJF16/0	II-1-3	13.4	3.1	500	12.5	10	linear,wide
JJF16/ π	II-1-1	4.5	1.8	500	12.5	10	linear,wide
JJF16/0- π	II-1-2	9.0	2.5	500	12.5	10	linear,wide
SINFS-F11-lg/0	II-1-5	16.6	4.0	500	10	5	linear,wide
SINFS-F11-lg/ π	II-1-3	23	4.7	500	10	5	linear,wide
SINFS-F11-lg/0- π	II-1-4	19.8	4.3	500	10	5	linear,wide
AJJ19-H-sm/0*	I-2-2	1.1	1.1	628	4	2	annular
AJJ19-H-sm/ π	I-1-1	3.2	2.2	628	4	2	annular
AJJ19-H-sm/0- π	I-1-2	2.2	1.6	628	4	2	annular
SINFS-13H-sm/0	II-1-8	50.4	0.69	50	10	5	linear,wide
SINFS-13H-sm/ π	II-1-1	40.0	0.61	50	10	5	linear,wide
SINFS-13H-sm/0- π	II-1-7	48.3	0.68	50	10	5	linear,wide

Table A.1: Parameters of the investigated samples. The critical current densities of chip JJF16 are measured at $T = 0.34$ K, the critical current densities of triplet SINFS-13H-sm are measured at $T = 0.2$ K, the other values at $T = 4.2$ K. L is the length of the junction; for annular samples on chip AJJ19-H-sm L is the circumference. l is the respective normalized length. W is the width of the junction, W_i is the width of the idle region. The parameters of junction AJJ19-H-sm/0* are estimated from other samples on the wafer, as this sample is broken. Idle region corrections are considered according to Ref. [MCM95].

Literaturverzeichnis

- [AB63a] V. Ambegaokar and A. Baratoff, *Tunneling between superconductors*, Phys. Rev. Lett. **10** (1963), 486.
- [AB63b] V. Ambegaokar and A. Baratoff, *Tunneling between superconductors*, Phys. Rev. Lett. **11** (1963), 104, erratum.
- [act09] activLLJJa.exe, by Dr. T. Gaber (2009).
- [And64] A. F. Andreev, *The thermal conductivity of the intermediate state in superconductors*, Zh. Eksp. Teor. Fiz. **46** (1964), 1823.
- [Arr89] S. Arrhenius, *Über die Reaktionsgeschwindigkeit der Umwandlung von Rohrzucker durch Säuren*, Z. Phys. Chem. (Leipzig) **49** (1889), 226.
- [BBA⁺04] A. Bauer, J. Bentner, M. Aprili, M. L. Della-Rocca, M. Reinwald, W. Wegscheider, and C. Strunk, *Spontaneous Supercurrent Induced by Ferromagnetic π Junctions*, Phys. Rev. Lett. **92** (2004), 217001.
- [BCS57] J. Bardeen, L. N. Cooper, and J. R. Schrieffer, *Theory of Superconductivity*, Phys. Rev. **108** (1957), 1175.
- [BGI01] G. Blatter, V. B. Geshkenbein, and L. B. Ioffe, *Design aspects of superconducting-phase quantum bits*, Phys. Rev. B **63** (2001), 174511.
- [BGS⁺07] K. Buckenmaier, T. Gaber, M. Siegel, D. Koelle, R. Kleiner, and E. Goldobin, *Spectroscopy of the Fractional Vortex Eigenfrequency in a Long Josephson $0-\kappa$ Junction*, Phys. Rev. Lett. **98** (2007), 117006.

- [BHL83] M. Büttiker, E. P. Harris, and R. Laundauer, *Thermal activation in extremely underdamped Josephson-junction circuits*, Phys. Rev. B **28** (1983), 1268.
- [BK04] W. Buckel and R. Kleiner, *Supraleitung: Grundlagen und Anwendungen*, 6 ed., Wiley-VCH, 2004.
- [BKS77] L. N. Bulaevskii, V. V. Kuzii, and A. A. Sobyenin, *Superconducting system with weak coupling to the current in the ground state*, JETP Lett. **25** (1977), 290, [Pis'ma Zh. Eksp. Teor. Fiz. 25, 314 (1977)].
- [BKS78] L. N. Bulaevskii, V. V. Kuzii, and A. A. Sobyenin, *On Possibility of the Spontaneous Magnetic Flux in a Josephson junction containing magnetic impurities*, Solid State Commun. **25** (1978), 1053.
- [BLT⁺05] T. Bauch, F. Lombardi, F. Tafuri, A. Barone, G. Rotoli, P. Delsing, and T. Claeson, *Macroscopic Quantum Tunneling in d-Wave $YBa_2Cu_3O_{7-\delta}$ Josephson Junctions*, Phys. Rev. Lett. **94** (2005), 087003.
- [BMU96] P. Barbara, R. Monaco, and A. V. Ustinov, *Model for the fine structure of zero field steps in long Josephson tunnel junctions and its comparison with experiment*, J. Appl. Phys. **79** (1996), 327.
- [BMWK99] J. J. A. Baselmans, A. F. Morpurgo, B. J. V. Wees, and T. M. Klapwijk, *Reversing the direction of the supercurrent in a controllable Josephson junction*, Nature **397** (1999), 43.
- [BP82a] A. Barone and G. Paterno, *Physics and Applications of the Josephson effect*, ch. 12.3, In [BP82b], 1982.
- [BP82b] A. Barone and G. Paterno, *Physics and Applications of the Josephson effect*, John Wiley & Sons, 1982.
- [BPS⁺09] A. A. Bannykh, J. Pfeiffer, V. S. Stolyarov, I. E. Batov, V. V. Ryazanov, and M. Weides, *Josephson tunnel junctions with a strong ferromagnetic interlayer*, Phys. Rev. B **79** (2009), 054501.

- [BSH⁺06] F. Born, M. Siegel, E. K. Hollmann, H. Braak, A. A. Golubov, D. Y. Gusakova, and M. Y. Kupriyanov, *Multiple $0-\pi$ transitions in superconductor/insulator/ferromagnet/superconductor Josephson tunnel junctions*, Phys. Rev. B **74** (2006), 140501.
- [BTKP02] Y. Blum, A. Tsukernik, M. Karpovski, and A. Palevski, *Oscillations of the Superconducting Critical Current in Nb-Cu-Ni-Cu-Nb Junctions*, Phys. Rev. Lett. **89** (2002), 187004.
- [Buz05] A. I. Buzdin, *Proximity effects in superconductor-ferromagnet heterostructures*, Rev. Mod. Phys. **77** (2005), 935.
- [CFL88] Y. C. Chen, M. P. A. Fisher, and A. J. Leggett, *The return of a hysteretic Josephson junction to the zero-voltage state: I-V characteristic and quantum retrapping*, J. Appl. Phys. **64** (1988), 3119.
- [CFP62] M. H. Cohen, L. M. Falicov, and J. C. Phillips, *Superconductive tunneling*, Phys. Rev. Lett. **8** (1962), 316.
- [CL83] A. O. Caldeira and A. J. Leggett, *Quantum Tunnelling in a Dissipative System*, Ann. Phys. (N.Y.) **149** (1983), 374.
- [CTC⁺96] M. G. Castellano, G. Torrioli, C. Cosmelli, A. Costantini, F. Chiarello, P. Carelli, G. Rotoli, M. Cirillo, and R. L. Kautz, *Thermally activated escape from the zero-voltage state in long Josephson junctions*, Phys. Rev. B **54** (1996), 15417.
- [CTC⁺97] M. G. Castellano, G. Torrioli, C. Cosmelli, F. Chiarello, M. Cirillo, P. Carelli, and G. Rotoli, *Magnetic Field Dependence of Thermal Excitations in Josephson Junctions*, IEEE Trans. Appl. Supercond. **7** (1997), 1051.
- [CWB⁺06] J.-P. Cleuziou, W. Wernsdorfer, V. Bouchiat, T. Ondarcuhu, and M. Monthieux, *Carbon nanotube superconducting quantum interference device*, Nature Nanotech. **1** (2006), 53.

- [DDKP85] A. Davidson, B. Dueholm, B. Kryger, and N. F. Pedersen, *Experimental Investigation of Trapped Sine-Gordon Solitons*, Phys. Rev. Lett. **55** (1985), 2059.
- [DMC85] M. H. Devoret, J. M. Martinis, and J. Clarke, *Measurements of Macroscopic Quantum Tunneling out of the Zero-Voltage State of a Current-Biased Josephson Junction*, Phys. Rev. Lett. **55** (1985), 1908.
- [DMEC84] M. Devoret, J. M. Martinis, D. Esteve, and J. Clarke, *Resonant Activation from the Zero-Voltage State of a Current-Biased Josephson Junction*, Phys. Rev. Lett. **53** (1984), 1260.
- [DRAK⁺05] M. L. Della Rocca, M. Aprili, T. Kontos, A. Gomez, and P. Spathis, *Ferromagnetic $0-\pi$ Junctions as Classical Spins*, Phys. Rev. Lett. **94** (2005), 197003.
- [Eil68] G. Eilenberger, *Transformation of Gorkov's equation for type II superconductors into transport-like equations*, Z. Phys. **214** (1968), 195.
- [FD74] T. A. Fulton and L. N. Dunkleberger, *Lifetime of the zero-voltage state in Josephson tunnel junctions*, Phys. Rev. B **9** (1974), 4760.
- [FF64] P. Fulde and R. A. Ferrell, *Superconductivity in a Strong Spin-Exchange Field*, Phys. Rev. **135** (1964), A550–A563.
- [FHO⁺04] S. M. Frolov, D. J. V. Harlingen, V. A. Oboznov, V. V. Bolginov, and V. V. Ryazanov, *Measurement of the current-phase relation of superconductor/ferromagnet/superconductor π Josephson junctions*, Phys. Rev. B **70** (2004), 144505.
- [FVHB⁺06] S. M. Frolov, D. J. Van Harlingen, V. V. Bolginov, V. A. Oboznov, and V. V. Ryazanov, *Josephson interferometry and Shapiro step measurements of superconductor-ferromagnet-superconductor $0-\pi$ junctions*, Phys. Rev. B **74** (2006), 020503(R).
- [FWK⁺03] M. V. Fistul, A. Wallraff, Y. Koval, A. Lukashenko, B. A. Malomed, and A. V. Ustinov, *Quantum Dissociation of*

- a Vortex-Antivortex Pair in a Long Josephson Junction*, Phys. Rev. Lett. **91** (2003), 257004.
- [GAB⁺03] W. Guichard, M. Aprili, O. Bourgeois, T. Kontos, J. Lesueur, and P. Gandit, *Phase Sensitive Experiments in Ferromagnetic-Based Josephson Junctions*, Phys. Rev. Lett. **90** (2003), 167001.
- [Gab07] T. Gaber, *Dynamik fraktionaler Flusswirbel in langen Josephsonkontakten*, Tübingen, PhD thesis (2007).
- [Gab09] T. Gaber, **et al.**, unpublished (2009).
- [Gar95] A. Garg, *Escape-field distribution for escape from a metastable potential well subject to a steadily increasing bias field*, Phys. Rev. B **51** (1995), 15592.
- [GBA09] E. Goldobin, T. L. Boyadjiev, and J. A. Angelova, *Critical relations in $0 - \pi$ junctions*, to be submitted to Phys. Rev. B (2009).
- [GGS⁺05] T. Gaber, E. Goldobin, A. Sterck, R. Kleiner, D. Koelle, M. Siegel, and M. Neuhaus, *Nonideal artificial phase discontinuity in long Josephson $0 - \kappa$ junctions*, Phys. Rev. B **72** (2005), 054522.
- [Gia60] I. Giaever, *Electron tunneling between two superconductors*, Phys. Rev. Lett. **5** (1960), 464.
- [GIS07] A. Gumann, C. Iniotakis, and N. Schopohl, *Geometric π Josephson junction in d -wave superconducting thin films*, Appl. Phys. Lett. **91** (2007), 192502.
- [GJC04] N. Grønbeck-Jensen and M. Cirillo, *Ac-induced thermal vortex escape in magnetic-field-embedded long annular Josephson junctions*, Phys. Rev. B **70** (2004), 214507.
- [GJCC⁺04] N. Grønbeck-Jensen, M. G. Castellano, F. Chiarello, M. Cirillo, C. Cosmelli, L. V. Filippenko, R. Russo, and G. Torriolo, *Microwave-Induced Thermal Escape in Josephson Junctions*, Phys. Rev. Lett. **93** (2004), 107002.
- [GK06] D. Gulevich and F. Kusmartsev, *Switching Phenomena in an Annular Josephson Junction*, Physica C **435** (2006), 87–91.

- [GKI04] A. A. Golubov, M. Y. Kupriyanov, and E. Il'ichev, *The current-phase relation in Josephson junctions*, Rev. Mod. Phys. **76** (2004), 411.
- [GKK02] E. Goldobin, D. Koelle, and R. Kleiner, *Semifluxons in long Josephson $0-\pi$ -junctions*, Phys. Rev. B **66** (2002), 100508(R).
- [GKK03] E. Goldobin, D. Koelle, and R. Kleiner, *Ground state and bias current induced rearrangement of semifluxons in $0-\pi$ -Josephson junctions*, Phys. Rev. B **67** (2003), 224515.
- [GKK04] E. Goldobin, D. Koelle, and R. Kleiner, *Ground states of one and two fractional vortices in long Josephson $0-\kappa$ junctions*, Phys. Rev. B **70** (2004), 174519.
- [GL50] V. L. Ginzburg and L. D. Landau, Zh. Eksperim. i Teor. Fiz. **20** (1950), 1064.
- [Gol] E. Goldobin, *GoldExI*, <http://www.geocities.com/SiliconValley/Heights/7318/>.
- [Gor59] L. P. Gor'kov, *Microscopic derivation of the Ginzburg Landau equations in the theory of Superconductivity*, Soviet Phys. JETP **9** (1959), 1364.
- [GSG+04] E. Goldobin, A. Sterck, T. Gaber, D. Koelle, and R. Kleiner, *Dynamics of semifluxons in Nb long Josephson $0-\pi$ junctions*, Phys. Rev. Lett. **92** (2004), 057005.
- [GSKK04] E. Goldobin, N. Stefanakis, D. Koelle, and R. Kleiner, *Fluxon-semifluxon interaction in an annular long Josephson $0-\pi$ junction*, Phys. Rev. B **70** (2004), 094520.
- [GVC+05] E. Goldobin, K. Vogel, O. Crasser, R. Walser, W. P. Schleich, D. Koelle, and R. Kleiner, *Quantum tunneling of semifluxons in a $0-\pi-0$ long Josephson junction*, Phys. Rev. B **72** (2005), 054527.
- [GVS+09] E. Goldobin, K. Vogel, W. P. Schleich, D. Koelle, and R. Kleiner, *Quantum tunneling of a single semifluxon in a $0-\pi$ Josephson junction*, submitted to Phys. Rev. B (2009).
- [GW84] H. Grabert and U. Weiss, *Crossover from Thermal Hopping to Quantum Tunneling*, Phys. Rev. Lett. **53** (1984), 1787.

- [Hal01] K. Haltermann, *Proximity effects at ferromagnet-superconductor interfaces*, Phys. Rev. B **65** (2001), 014509.
- [HAS⁺03] H. Hilgenkamp, Ariando, H.-J. H. Smilde, D. H. A. Blank, G. Rijnders, H. Rogalla, J. R. Kirtley, and C. C. Tsuei, *Ordering and manipulation of the magnetic moments in large-scale superconducting π -loop arrays*, Nature (London) **422** (2003), 50.
- [HE84] K. Hida and U. Eckern, *Quantum dynamics of the sine-Gordon model in the presence of dissipation*, Phys. Rev. B **30** (1984), 4096.
- [HFS⁺07] A. Herr, A. Fedorov, A. Shnirman, E. Ilichev, and G. Schoen, *Design of a ballistic fluxon qubit readout*, Supercond. Sci. Technol. **20** (2007), S450.
- [HPH⁺02] J. Huang, F. Pierre, T. T. Heikkilä, F. K. Wilhelm, and N. O. Birge, *Observation of a controllable π junction in a 3-terminal Josephson device*, Phys. Rev. B **66** (2002), 020507.
- [HSBJ94] Z. Hermon, A. Stern, and E. Ben-Jacob, *Quantum dynamics of a fluxon in a long circular Josephson Junction*, Phys. Rev. B **49** (1994), 9757.
- [HTB90] P. Hänggi, P. Talkner, and M. Borkovec, *Reaction rate theory: fifty years after Kramers*, Rev. Mod. Phys. **49** (1990), 251–341.
- [IGF⁺99] L. B. Ioffe, V. B. Geshkenbein, M. V. Feigel'man, A. L. Faucheère, and G. Blatter, *Environmentally decoupled sds-wave Josephson junctions for quantum computing*, Nature (London) **398** (1999), 679.
- [JGH⁺81] L. D. Jackel, J. P. Gordon, E. L. Hu, R. E. Howard, L. A. Fetter, D. M. Tennant, R. W. Epworth, and J. Kurkijarvi, *Decay of the Zero-Voltage State in Small-Area, High-Current-Density Josephson Junctions*, Phys. Rev. Lett. **47** (1981), 697.

- [JNGR⁺07] H. Jorgensen, T. Novotny, K. Grove-Rasmussen, K. Flensburg, and P. Lindelof, *Critical Current $0-\pi$ Transition in Designed Josephson Quantum Dot Junctions*, Nano Lett. **7** (2007), 2441.
- [KAL⁺02] T. Kontos, M. Aprili, J. Lesueur, F. Genêt, B. Stephanidis, and R. Boursier, *Josephson Junction through a Thin Ferromagnetic Layer: Negative Coupling*, Phys. Rev. Lett. **89** (2002), 137007.
- [KCK00] V. G. Kogan, J. R. Clem, and J. R. Kirtley, *Josephson vortices at tricrystal boundaries*, Phys. Rev. B **61** (2000), 9122.
- [Kem06] A. Kemp, *Quantum and Thermal Phase Escape in Extended Josephson Systems*, Erlangen, PhD thesis (2006).
- [KGB⁺09a] U. Kienzle, T. Gaber, K. Buckenmaier, K. Ilin, M. Siegel, D. Koelle, R. Kleiner, and E. Goldobin, unpublished (2009).
- [KGB⁺09b] U. Kienzle, T. Gaber, K. Buckenmaier, K. Ilin, M. Siegel, D. Koelle, R. Kleiner, and E. Goldobin, *Thermal escape of fractional vortices in long Josephson junctions*, Phys. Rev. B **80** (2009), 014504.
- [KI96] T. Kato and M. Imada, *Macroscopic Quantum Tunneling of a Fluxon in a Long Josephson Junction*, J. Phys. Soc. Jpn. **65** (1996), 2963.
- [KI97] T. Kato and M. Imada, *Vortices and Quantum Tunneling in Current-Biased $0-\pi-0$ Josephson Junctions of d -Wave Superconductors*, J. Phys. Soc. Jpn. **66** (1997), 1445.
- [KM89] Y. S. Kivshar and B. A. Malomed, *Dynamics of solitons in nearly integrable systems*, Rev. Mod. Phys. **61** (1989).
- [KMS97] J. R. Kirtley, K. A. Moler, and D. J. Scalapino, *Spontaneous flux and magnetic-interference patterns in $0-\pi$ Josephson junctions*, Phys. Rev. B **56** (1997), 886.
- [KO11] H. Kammerlingh-Onnes, Leiden Comm. **120b**, **122b**, **124c** (1911).

- [Kra40] H. A. Kramers, *Brownian motion in a field of force and the diffusion model of chemical reactions*, *Physica* **7** (1940), 284.
- [KTA⁺05] J. R. Kirtley, C. C. Tsuei, Ariando, H. J. H. Smilde, and H. Hilgenkamp, *Antiferromagnetic ordering in arrays of superconducting π -rings*, *Phys. Rev. B* **72** (2005), 214521.
- [KTM99] J. R. Kirtley, C. C. Tsuei, and K. A. Moler, *Temperature Dependence of The Half-Integer Magnetic Flux quantum*, *Science* **285** (1999), 1373.
- [KTR⁺96] J. R. Kirtley, C. C. Tsuei, M. Rupp, J. Z. Sun, L. S. Yu-Jahnes, A. Gupta, M. B. Ketchen, K. A. Moler, and M. Bhushan, *Direct imaging of integer and half-integer Josephson vortices in high- T_c grain boundaries*, *Phys. Rev. Lett.* **76** (1996), 1336.
- [Kul65] I. O. Kulik, *Pis'ma Zh. Eksp. Teor. Fiz.* **2** (1965), 134.
- [KWW⁺09] M. Kemmler, M. Weides, M. Weiler, M. Opel, S. T. B. Goennenwein, A. S. Vasenko, A. A. Golubov, H. Kohlstedt, D. Koelle, R. Kleiner, and E. Goldobin, *Magnetic interference patterns in $0-\pi$ SIFS Josephson junctions: effects of asymmetry between 0 and π regions*, to be submitted to *Phys. Rev. B*, arXiv:0910.5907 (2009).
- [Laz04] N. Lazarides, *Critical current and fluxon dynamics in overdamped $0-\pi$ Josephson junctions*, *Phys. Rev. B* **69** (2004), 212501.
- [LB92] G. S. Lee and A. T. Barfknecht, *Geometric and Material Dispersion in Josephson Transmission Lines*, *IEEE Trans. Appl. Supercond.* **2** (1992), 67.
- [Leg80] A. J. Leggett, *Macroscopic Quantum Systems and the Quantum Theory of Measurement*, *Prog. Theor. Phys. Suppl.* **69** (1980), 80.
- [Leg84] A. J. Leggett, *Percolation, localization, and superconductivity*, ch. Macroscopic quantum tunnelling and related effects in Josephson systems, New York, Plenum Press, 1984.

- [Lik86] K. K. Likharev, *Dynamics of Josephson Junctions and Circuits*, Gordon and Breach, Philadelphia, 1986.
- [Lis08] J. Lisenfeld, *Experiments on superconducting Josephson Phase Quantum Bits*, Erlangen, PhD thesis (2008).
- [LO65] A. Larkin and Y. N. Ovchinnikov, Sov. Phys. JETP **20** (1965), 762.
- [LTR⁺02] F. Lombardi, F. Tafuri, F. Ricci, F. Miletto Granozio, A. Barone, G. Testa, E. Sarnelli, J. R. Kirtley, and C. C. Tsuei, *Intrinsic d-Wave Effects in $YBa_2Cu_3O_{7-\delta}$ Grain Boundary Josephson Junctions*, Phys. Rev. Lett. **89** (2002), 207001.
- [LU08] A. Lukashenko and A. Ustinov, *Improved powder filters for qubit measurements*, Rev. Sci. Instr. **79** (2008), 014701.
- [MBW⁺06] K. Madek, S. Beutner, G. Wild, C. Probst, M. Weides, H. Kohlstedt, A. Marx, and R. Gross, *Observation of Macroscopic Quantum Behavior in π Josephson Junctions with Ferromagnetic Interlayer*, unpublished (2006).
- [McC68] D. E. McCumber, *Tunneling and Weak-Link Superconductor Phenomena Having Potential Device Applications*, J. Appl. Phys. **39** (1968), 2503.
- [MCM95] R. Monaco, G. Costabile, and N. Martucciello, *Influence of the idle region on the dynamic properties of window Josephson tunnel junctions*, J. Appl. Phys. **77** (1995), 2073.
- [MDC85] J. M. Martinis, M. H. Devoret, and J. Clarke, *Energy-Level Quantization in the Zero-Voltage State of a Current-Biased Josephson Junction*, Phys. Rev. Lett. **55** (1985), 1543.
- [MDC87] J. M. Martinis, M. H. Devoret, and J. Clarke, *Experimental tests for the quantum behavior of a macroscopic degree of freedom: The phase difference across a Josephson junction*, Phys. Rev. B **35** (1987), 4682.
- [MO33] W. Meißner and R. Ochsenfeld, *Ein neuer Effekt bei Eintritt der Supraleitfähigkeit*, Naturwissenschaften **21** (1933), 787.

- [MOL⁺99] J. E. Mooij, T. P. Orlando, L. Levitov, L. Tian, C. H. van der Wal, and S. Lloyd, *Josephson Persistent-Current Qubit*, *Science* **285** (1999), 1036.
- [MS78] D. W. McLaughlin and A. C. Scott, *Phys. Rev. A* **18** (1978), 1652.
- [MSS01] Y. Makhlin, G. Schön, and A. Shnirman, *Quantum-state engineering with Josephson-junction devices*, *Rev. Mod. Phys.* **73** (2001), 357.
- [NH86] S. Nakaya and K. Hida, *Quantum Tunneling of Nonlinear Klein-Gordon System with Dissipation in High External Field*, *J. Phys. Soc. Jpn.* **55** (1986), 3768.
- [NSAN06] C. Nappi, E. Sarnelli, M. Adamo, and M. A. Navacerrada, *Fiske modes in $0-\pi$ Josephson junctions*, *Phys. Rev. B* **74** (2006), 144504.
- [NSS60] J. Nicol, S. Shapiro, and P. Smith, *Direct measurement of the superconducting energy gap*, *Phys. Rev. Lett.* **5** (1960), 461.
- [OAM⁺06] T. Orllepp, Ariando, O. Mielke, C. J. M. Verwijs, K. F. K. Foo, H. Rogalla, F. H. Uhlmann, and H. Hilgenkamp, *Flip-Flopping Fractional Flux Quanta*, *Science* **312** (2006), 1495.
- [OBF⁺06] V. A. Oboznov, V. V. Bol'ginov, A. K. Feofanov, V. V. Ryazanov, and A. I. Buzdin, *Thickness Dependence of the Josephson Ground States of Superconductor-Ferromagnet-Superconductor Junctions*, *Phys. Rev. Lett.* **96** (2006), 197003.
- [PA09] I. Petkovic and M. Aprili, *Phase Dynamics of Ferromagnetic Josephson Junctions*, *Phys. Rev. Lett.* **102** (2009), 157003.
- [PLC⁺81] R. J. Prance, A. P. Long, T. D. Clark, A. Widom, J. E. Mutton, J. Sacco, M. W. Potts, G. Megaloudis, and F. Goodall, *Macroscopic quantum electrodynamic effects in a superconducting ring containing a Josephson weak link*, *Nature (London)* **289** (1981), 543.

- [RGP⁺98] B. Ruggiero, C. Granata, V. G. Palmieri, A. Esposito, M. Russo, and P. Silvestri, *Supercurrent decay in extremely underdamped Josephson junctions*, Phys. Rev. B **57** (1998), 134.
- [ROR⁺01] V. V. Ryazanov, V. A. Oboznov, A. Y. Rusanov, A. V. Veretennikov, A. A. Golubov, and J. Aarts, *Coupling of Two Superconductors through a Ferromagnet: Evidence for a π Junction*, Phys. Rev. Lett. **86** (2001), 2427.
- [ROVR01] V. V. Ryazanov, V. A. Oboznov, A. V. Veretennikov, and A. Y. Rusanov, *Intrinsically frustrated superconducting array of superconductor-ferromagnet-superconductor π junctions*, Phys. Rev. B **65** (2001), 020501.
- [RPB⁺06] J. W. A. Robinson, S. Piano, G. Burnell, C. Bell, and M. G. Blamire, *Critical Current Oscillations in Strong Ferromagnetic π Junctions*, Phys. Rev. Lett. **97** (2006), 177003.
- [RSC⁺08] G. Rotoli, D. Stornaiuolo, K. Cedergren, A. Leo, D. Born, T. Bauch, A. Barone, F. Lombardi, and F. Tafuri, *Resonant phase dynamics in faceted high- T_c Josephson junctions*, unpublished (2008).
- [SAB⁺02] H.-J. H. Smilde, Ariando, D. H. A. Blank, G. J. Gerritsma, H. Hilgenkamp, and H. Rogalla, *d-Wave-Induced Josephson Current Counterflow in $YBa_2Cu_3O_7/Nb$ Zigzag Junctions*, Phys. Rev. Lett. **88** (2002), 057004.
- [SBLC03] H. Sellier, C. Baraduc, F. Lefloch, and R. Calemczuk, *Temperature-induced crossover between 0 and π states in S/F/S junctions*, Phys. Rev. B **68** (2003), 054531.
- [SBLC04] H. Sellier, C. Baraduc, F. Lefloch, and R. Calemczuk, *Half-Integer Shapiro Steps at the 0- π Crossover of a Ferromagnetic Josephson Junction*, Phys. Rev. Lett. **92** (2004), 257005.
- [Sca69] D. J. Scalapino, *Tunnelling phenomena in Solids*, p. 477, E. Burstein and S. Lundqvist, Plenum, New York, 1969.
- [Sch97] V. V. Schmidt, *The Physics of Superconductors*, Springer, Berlin, 1997.

- [SG90] H. Simanjuntak and L. Gunther, *Macroscopic quantum tunneling in long Josephson junctions*, Phys. Rev. B **42** (1990), 930.
- [Skj09] Skjj32.exe, by Dr. Edward Goldobin (2009).
- [SOR⁺08] I. S.Veshchunov, V. A. Oboznov, A. N. Rossolenko, L. V. A. S. Prokofiev, A. Y. Rusanov, and D. V. Matveev, *Observation of the magnetic domain structures in Cu_{0.47}Ni_{0.53} thin films*, Pis'ma v ZhETF **88** (2008), N11.
- [SPRR97] P. Silvestri, V. G. Palmieri, B. Ruggiero, and M. Russo, *Observation of Energy Levels Quantization in Underdamped Josephson Junctions above the Classical-Quantum Regime Crossover Temperature*, Phys. Rev. Lett. **79** (1997), 3046.
- [Ste68] W. C. Stewart, *Current-Voltage Characteristics of Josephson Junctions*, Appl. Phys. Lett. **12** (1968), 277.
- [Ste02] N. Stefanakis, *Resonant flux motion and I-V characteristics in frustrated Josephson junctions*, Phys. Rev. B **66** (2002), 214524.
- [SvGV⁺03] H. Susanto, S. A. van Gils, T. P. P. Visser, Ariando, H.-J. H. Smilde, and H. Hilgenkamp, *Static semifluxons in a long Josephson junction with π -discontinuity points*, Phys. Rev. B **68** (2003), 104501.
- [TB98] E. Terzioglu and M. R. Beasley, *Complementary Josephson Junction Devices and Circuits: A Possible New Approach to Superconducting Electronics*, IEEE Trans. Appl. Supercond. **8** (1998), 48.
- [TGB97] E. Terzioglu, D. Gupta, and M. R. Beasley, *Complementary Josephson Junction circuits*, IEEE Trans. Appl. Supercond. **7** (1997), 3642.
- [TK00] C. C. Tsuei and J. R. Kirtley, *Pairing symmetry in cuprate superconductors*, Rev. Mod. Phys. **72** (2000), 969.
- [UK03] A. V. Ustinov and V. K. Kaplunenko, *Rapid single-flux quantum logic using π -shifters*, J. Appl. Phys. **94** (2003), 5405.

- [Usa70] L. Usadel, *Generalized diffusion equation for superconducting alloys*, Phys. Rev. Lett. **25** (1970), 507.
- [Ust09] A. V. Ustinov, *Solitons in Josephson Junctions: Physics of Magnetic Fluxons in Superconducting Junctions and Ar-rays*, 1 ed., Wiley-VCH, 2009.
- [vDNB⁺06] J. A. van Dam, Y. V. Nazarov, E. P. A. M. Bakkers, S. De Franceschi, and L. P. Kouwenhoven, *Supercurrent reversal in quantum dots*, Nature (London) **442** (2006), 667.
- [VGG⁺06] O. Vavra, S. Gazi, D. S. Golubovic, I. Vavra, J. Derer, J. Verbeeck, G. Van Tendeloo, and V. V. Moshchalkov, *0 and π phase Josephson coupling through an insulating barrier with magnetic impurities*, Phys. Rev. B **74** (2006), 020502.
- [VGJ⁺96] D. Vion, M. Götz, P. Joyez, D. Esteve, and M. Devoret, *Thermal Activation above a Dissipation Barrier: Switching of a Small Josephson Junction*, Phys. Rev. Lett. **77** (1996), 3435.
- [VGKW08] A. S. Vasenko, A. A. Golubov, M. Y. Kupriyanov, and M. Weides, *Properties of tunnel Josephson junctions with ferromagnetic interlayer*, Phys. Rev. B **77** (2008), 134507.
- [VH95] D. J. Van Harlingen, *Phase sensitive tests of the symmetry of the pairing state in the high-temperature superconductors — Evidence for $d_{x^2-y^2}$ symmetry*, Rev. Mod. Phys. **67** (1995), 515.
- [VSK⁺09] K. Vogel, W. P. Schleich, T. Kato, D. Koelle, R. Kleiner, and E. Goldobin, *Theory of fractional vortex escape in a long Josephson junction*, Phys. Rev. B **80** (2009), 134515.
- [Wal01] A. Wallraff, *Fluxon Dynamics in Annular Josephson Junction: From Relativistic Strings to Quantum Particles*, Erlangen, PhD thesis (2001).
- [WDLU03] A. Wallraff, T. Duty, A. Lukashenko, and A. V. Ustinov, *Multiphoton Transitions between Energy Levels in a Current-Biased Josephson Tunnel Junction*, Phys. Rev. Lett. **90** (2003), 037003.

- [Wei69] M. Weihnacht, Phys. Status Solidi **32** (1969), K 169.
- [Wei06] M. Weides, *Josephson tunnel junctions with ferromagnetic interlayer*, Köln, PhD thesis (2006).
- [WKG⁺06] M. Weides, M. Kemmler, E. Goldobin, D. Koelle, R. Kleiner, H. Kohlstedt, and A. Buzdin, *High quality ferromagnetic 0 and π Josephson tunnel junctions*, Appl. Phys. Lett. **89** (2006), 122511.
- [WKK⁺06] M. Weides, M. Kemmler, H. Kohlstedt, R. Waser, D. Koelle, R. Kleiner, and E. Goldobin, *0 - π Josephson Tunnel Junctions with Ferromagnetic Barrier*, Phys. Rev. Lett. **97** (2006), 247001.
- [WLC⁺03] A. Wallraff, A. Lukashenko, C. Coqui, A. Kemp, T. Duty, and A. Ustinov, *Switching current measurements of large area Josephson tunnel junctions*, Rev. Sci. Instr. **74** (2003), 3740.
- [WLL⁺03] A. Wallraff, A. Lukashenko, J. Lisenfeld, A. Kemp, M. V. Fistul, Y. Koval, and A. V. Ustinov, *Quantum dynamics of a single vortex*, Nature **425** (2003), 155.
- [WSK07] M. Weides, C. Schindler, and H. Kohlstedt, *Low- T_c Josephson junctions with tailored barrier*, J. Appl. Phys. **101** (2007), 063902.
- [WTK06] M. Weides, K. Tillmann, and H. Kohlstedt, *Fabrication of high quality ferromagnetic Josephson junctions*, Physica C **437–438** (2006), 349.
- [WVHL⁺93] D. A. Wollman, D. J. Van Harlingen, W. C. Lee, D. M. Ginsberg, and A. J. Leggett, *Experimental determination of the superconducting pairing state in YBCO from the phase coherence of YBCO-Pb dc SQUIDs*, Phys. Rev. Lett. **71** (1993), 2134.
- [XMT95] J. H. Xu, J. H. Miller, and C. S. Ting, *π -vortex state in a long 0 - π -Josephson junction*, Phys. Rev. B **51** (1995), 11958.
- [YTM06] T. Yamashita, S. Takahashi, and S. Maekawa, *Superconducting π qubit with three Josephson junctions*, Appl. Phys. Lett. **88** (2006), 132501.

- [YTTM05] T. Yamashita, K. Tanikawa, S. Takahashi, and S. Maekawa, *Superconducting π Qubit with a Ferromagnetic Josephson Junction*, Phys. Rev. Lett. **95** (2005), 097001.
- [ZG04] A. Zenchuk and E. Goldobin, *Analytical analysis of ground states of 0 - π long Josephson junctions*, Phys. Rev. B **69** (2004), 024515.

Acknowledgements

Zuallererst möchte ich **Prof. Dr. Reinhold Kleiner** und **Prof. Dr. Dieter Koelle** dafür danken, dass sie mir die Möglichkeit boten, über das so interessante und aktuelle Thema der SIFS-Kontakte zu promovieren. Sie haben mich während aller Phasen meiner Arbeit unterstützt, mir die Teilnahme an mehreren nationalen / internationalen Konferenzen ermöglicht, und — mir aber auch viel Freiraum gelassen. Dieter Koelle danke ich zudem dafür, dass er für alle nicht-physikalischen Belange seiner Mitarbeiter stets ein offenes Ohr hat. Ich danke **Dr. Edward Goldobin** für die Hilfe und Unterstützung während der letzten drei Jahre. Danke Edward, für die vielen netten Gespräche, insbesondere über Russisch, die russische Seele und das Land im Allgemeinen!

Besonderer Dank geht an **Dr. Martin Weides** (Forschungszentrum Jülich), von dem ich meine Proben bezogen habe. Unsere Zusammenarbeit war immer exzellent, die Diskussionen gewinnbringend und motivierend - und es hat auch noch Spass gemacht! Unsere zahlreichen gemeinsamen Besuche auf Konferenzen werden mir in guter Erinnerung bleiben, besonders Moskau. Dir, Martin, alles Gute auf deinem Weg! Und ein großes Danke für alles!

Wholeheartedly, I want to thank **Prof. Dr. Alexey Ustinov** (meanwhile University of Karlsruhe) for our fruitful collaboration. Results of my thesis were produced using his measurement setups and equipment. Alexey, I thank you for your support, your wisdom and friendship. I thank Alexey's group, my former colleagues (namely Jürgen Lisenfeld, Sasha Lukashenko, Tobias Wirth and Lyosha Feofanov) that their welcomed me warmly whenever I did measurements in their group. Jürgen and Lyosha, thanks for your great help in the lab!

I thank **Prof. Dr. Valery Ryazanov** (Institute of Solid State Physics, Chernogolova, Russia) that he invited me to work in this group for two months during my thesis. I appreciate that he gave me the oppor-

tunity to make very different and exciting experiences in a fascinating country like Russia. I thank his group (especially **Alexander Rusanov**) for taking care about me so enthusiastically.

Ich danke all meinen Kollegen im sechsten Stock für die angenehme Atmosphäre. Besonders hervorzuheben sind: **Dr. Matthias Kemmler**, der mich so lange Zeit als Schreibtischnachbarin ausgehalten hat. Ich möchte ihm dafür danken, dass er seinen Aufbau mit mir geteilt, mich in das Thema eingeführt und so viele Fragen physikalischer Art diskutiert hat. Nicht zuletzt danke ich dir Matze, dass du die Kaffeemaschine am Leben gehalten hast! Ich danke **Dr. Tobias Gaber**, Exilerlanger wie ich, für seine Unterstützung in so zahlreichen Belangen (Was habe ich dich eigentlich nicht gefragt?). Für die fachliche Hilfestellung, die zur-Verfügung-Stellung diverser Software, die Mithilfe und Ko-autorschaft, und letztendlich für das Korrekturlesen meiner Arbeit. **Christian Gürlich** danke ich für seine Unterstützung als Administrator, seine freundschaftliche Art und immer gute Laune — und dass er mir einen Platz freihalten wird. Ich danke euch, Matze, Tobi und Christian, nicht zuletzt sondern vor allem für eure Freundschaft. **Kai Buckenmayer** und **Uta Kienzle** danke ich für ihre Hilfe mit dem Mischkryostaten.

Ich danke unseren beiden Sekretärinnen **Marie-Luise Fenske** und **Marie-Annick Pacquier**, die mich organisatorisch immer auf dem Laufenden gehalten haben. Und dafür, dass sie die guten Seelen der Abteilung sind. Marie-Luises herzliche Art werde ich vermissen. Ich danke **Elmar Baur** und **Manuel Brandt**, dass sie sich zu den unmöglichsten Zeiten (bei Schneesturm und Regen) für mich mit ihren Heliumkannen den Berg hinuntergestürzt haben. Ebenso danke ich den Werkstätten für ihre zuverlässige Unterstützung. An dieser Stelle möchte ich auch noch **Hans Wener** danken, dessen tatkräftige Unterstützung ich leider nur kurz genießen durfte.

An dieser Stelle möchte ich abschließend allen Kollegen und Freunden am Lehrstuhl für die Zukunft alles erdenklich Gute wünschen.

Bei der **Studienstiftung des Deutschen Volkes** möchte ich mich für das in mich gesetzte Vertrauen und die Finanzierung meiner Dissertation bedanken. Ebenso für die Finanzierung meines Aufenthalts in Russland und die Teilnahme an verschiedenen Konferenzen. Stellvertretend für die so reibungslose und unkomplizierte Organisation bedanke ich mich bei Imke Thamm, für die vor-Ort-Betreuung danke ich meiner Vertrauensdozentin **Prof. Dr. Schamma Shahadat**.

Zuletzt oder zuerst möchte ich mich noch bei meiner Familie und meinen Freunden bedanken. Ohne ihren Rückhalt wäre so manche Durst-

strecke schwieriger und so manche Wolke dunkler gewesen. Danke aber auch für die schöne, erlebnisreiche, das-Herz-nährende Zeit! Vor allen möchte ich meiner **Mama** danken, die mich in jeder erdenklichen Weise auf den vielen Stationen meines Lebens unterstützt hat. Danke! Mein letzter (Ge)dank(e) gilt meinem Freund **Marcus**. Ich danke dir, dass du jeden unserer Tage zu einem Geschenk machst.

Publikationsliste

1. **J. Pfeiffer**, M. Schuster, A. A. Abdumalikov, and A. V. Ustinov, *Observation of Soliton Fusion in a Josephson Array*, Phys. Ref. Lett. **96**, 034103 (2006).
2. M. Weides, H. Kohlsted, R. Waser, M. Kemmler, **J. Pfeiffer**, D. Koelle, R. Kleiner, and E. Goldobin, *Ferromagnetic $0-\pi$ Josephson junctions*, Appl. Phys. A **89**, 613-617 (2007).
3. **J. Pfeiffer**, A. A. Abdumalikov, M. Schuster, and A. V. Ustinov, *Resonances between fluxons and plasma waves in underdamped Josephson transmission lines of stripline geometry*, Phys. Ref. B **77**, 024511 (2008).
4. **J. Pfeiffer**, M. Kemmler, D. Koelle, R. Kleiner, E. Goldobin, M. Weides, A. K. Feofanov, J. Lisenfeld, and A. V. Ustinov, *Static and dynamic properties of 0 , π , and $0-\pi$ ferromagnetic Josephson tunnel junctions*, Phys. Ref. B **77**, 214506 (2008).
5. **Online-publication**: European Superconductivity News forum, 3rd Issue, 7. February 2008, New Paper and Result Highlights, H20.
6. A. A. Bannykh, **J. Pfeiffer**, V. S. Stolyarov, I. E. Batov, V. V. Ryazanov, and M. Weides, *Josephson tunnel junctions with a strong ferromagnetic interlayer*, Phys. Rev. B **79**, 054501 (2009).
7. **J. Pfeiffer**, A. S. Malishesvkii, A. K. Feofanov, and A. V. Ustinov, *Vortices in Comb-arrays of submicron Josephson Junctions*, to be submitted to Phys. Ref. B.

Lebenslauf

Persönliches:

Judith Pfeiffer
geboren am 16.01.1979 in Schweinfurt
ledig; deutsch

Schulbildung:

1985 – 1989	Vitus-Grundschule Veitshöchheim
1989 – 1990	Ludwig-von-Erthal Gymnasium Lohr
1990 – 1993	Gymnasium Bad Königshofen
1993 – 1998	Celtis-Gymnasium Schweinfurt

Abschluß: Allgemeine Hochschulreife (Abitur)
Notendurchschnitt: 1,0

Hochschulbildung:

11/1998 – 05/2006	Friedrich-Alexander Universität (FAU) Erlangen Doppelstudium Diplom-Physik / Diplom-Biologie Schwerpunkte in Physik: Experimentalphysik, Tieftemperaturphysik, Supraleitung. Diplomarbeit über “Kinks and Resonances in Discrete Josephson Transmission Lines” (Arbeitsgruppe Prof. Dr. A. Ustinov) Abschluß: Diplom (Gesamtnote: 1,0 / mit Auszeichnung) Ohm-Preis für die beste Diplomarbeit der Fakultät Physik (FAU Erlangen) im Jahr 2005
	Schwerpunkte in Biologie: Humangenetik, Immunologie. Diplomarbeit über “Funktion und Expression des NKX-kodierten

Rezeptors LLT1" (extern betreute Diplomarbeit
 an der Eberhard Karls Universität Tübingen,
 Arbeitsgruppe PD. Dr. A. Steinle)
 Abschluß: Diplom (Gesamtnote: 1,0)
 09/2006 – 11/2009 Eberhard Karls Universität Tübingen
 Promotion in Physik über
 "Fractional vortices in Josephson tunnel junctions
 with a ferromagnetic interlayer"
 (Arbeitsgruppe Prof. Dr. R. Kleiner,
 Physikalisches Institut)

Auslandsaufenthalte:

10/2000 – 07/2001 University of Cambridge,
 Fitzwilliam College, Großbritannien
 Studium: Special subject Physics / Biochemistry
 05/2008 – 06/2008 Russian Academy of Sciences,
 Institute of Solid State Physics, Chernogolovka, Russland

Stipendien, Auszeichnungen:

10/1998 – 09/2004 Bayerisches Hochbegabtenstipendium, Vollstipendium
 10/2001 – 01/2005 Studienstiftung des Deutschen Volkes, Studienstipendium
 07/2005 Ohm-Preis, beste Diplomarbeit der Fakultät Physik
 (FAU Erlangen) im Jahr 2005
 06/2007 – 12/2009 Studienstiftung des Deutschen Volkes, Promotionsstipendium

Praktische Tätigkeiten:

2002 Studentische Hilfskraft bei
 UroNova GmbH Medizinische Implantate, Erlangen
 10/2002 – 11/2002 Studentische Hilfskraft bei
 Biotronik GmbH Co., Erlangen
 2004 – 2005 Studentische Hilfskraft am Phys. Inst. III, FAU Erlangen
 (Lehrtätigkeit, Praktikumsbetreuung, Übungsbetreuung)
 06/2006 – 08/2006 Wissenschaftliche Hilfskraft am Institut für Immunologie,
 Eberhard Karls Universität Tübingen (Labortätigkeit)

Akademische Lehrer: (in Physik)

G. Anton, W. P. Barth, R. van Eldik, W. Eyrich, T. Fauster, B. Hensel, A.
 Hüller, A. Knauf, R. Kleiner, D. Koelle, W. Kretschmer, F. Lenz, H. Leschke,
 P. Müller, O. Pankratov, G. Pensl, M. Schulz, D. Sellmann, M. Thies, C.
 Toepffer, A. V. Ustinov, H. G. Weidner, H. Wilsch, J. Zowe.